University of South Carolina
Scholar Commons

Theses and Dissertations

2015

InN NEMS and Heterojunction Devices For Sensing Applications

Alina Wilson
University of South Carolina

Follow this and additional works at: http://scholarcommons.sc.edu/etd

Part of the Electrical and Computer Engineering Commons

Recommended Citation
Wilson, A.(2015). *InN NEMS and Heterojunction Devices For Sensing Applications.* (Doctoral dissertation). Retrieved from http://scholarcommons.sc.edu/etd/3640

This Open Access Dissertation is brought to you for free and open access by Scholar Commons. It has been accepted for inclusion in Theses and Dissertations by an authorized administrator of Scholar Commons. For more information, please contact SCHOLARC@mailbox.sc.edu.

InN NEMS and Heterojunction Devices for Sensing Applications

by

Alina Wilson

Bachelor of Science
University of South Carolina, 2010

Master of Engineering
University of South Carolina, 2015

Submitted in Partial Fulfillment of the Requirements

For the Degree of Doctor of Philosophy in

Electrical Engineering

College of Engineering and Computing

University of South Carolina

2015

Accepted by:

Goutam Koley, Major Professor

MVS Chandrashekhar, Committee Member

Mohammod Ali, Committee Member

Richard Webb, Committee Member

Lacy Ford, Senior Vice Provost and Dean of Graduate Studies

© Copyright by Alina Wilson, 2015
All Rights Reserved.

Dedication

I dedicate this dissertation to

my parents Angela and Stefan, and my fiancé Levi

for their constant support and unconditional love.

I love you all dearly.

ACKNOWLEDGEMENTS

It has been a long journey fulfilled with frustration, happiness, accomplishments, hard work, long hours of discussion and planning, but I would not have it any other way. This achievement in my life would not be possible without my advisor and mentor, Professor Goutam Koley, who believed in me from the beginning, after just finishing my bachelor degree in a different field than the one I wanted to pursue PhD for. I would like to thank him for the endless support and guidance throughout my graduate studies and research for the past five years. I will forever be thankful for accepting me to be part of his research team and for guiding me through the rough road towards the finish line. I am grateful for the many insightful discussions and suggestions, and for the scientific advice throughout the years, which made possible finishing this thesis. Without his limitless help I would not be where I am today.

I owe my gratitude to all of the committee members, Professor Richard Webb, Dr. MVS Chandrashekhar and Professor Mohammod Ali for their help, advice and suggestions. I would like to express my gratitude to Professor Webb, who generously allowed me to use his facility in the Nanocenter and for allowing me permission to use ZEISS SEM located in the Electron Microscopy Center. I would like to thank Prof. Webb for his research advice and for his patience, understanding and help when reporting about malfunction of instruments. I would also like to thank Dr. Chandrashekhar for allowing me to use the clean room facility, Nomarski microscope, FTIR, instruments without

which I would not be able to fabricate and characterize my devices and finish my dissertation.

I would like to acknowledge the financial support from NSF grant that funded part of the research for this dissertation. I would like to acknowledge South Carolina Space Grant Consortium and NASA EPSCoR for awarding me for two consecutive years with the Graduate Research Assistantship, which was a tremendous help in completing part of my dissertation. My last year of graduate school would not be possible without financial help from Southern Regional Education Board, which awarded me with the Dissertation Fellowship and gave me the ease of mind to finish my research and write my thesis.

I am thankful to all the present and past members of Nanoscale and Sensors Lab for their constant help and support. I will cherish all the moments forever. Special thanks to Ifat Jahangir, for helping me with fabrication techniques and various measurements. His constant support and friendship helped me maintain my self-esteem and confidence in difficult times. A big thanks also goes to staff at the department of Electrical Engineering, especially Nat, for pushing me in applying for the Southern Regional Education Board fellowship, Dave, for helping me with my computer problems, and Ashley, for making sure that all my graduation paperwork was completed and turned in on time.

Last but not least, I would like to express my gratitude to my friends for their patience and moral support throughout the years. To my fiancé, Levi, who loves me and supports me during difficult times. To my mother Angela and father Stefan, for providing unconditional love and guidance throughout my life.

ABSTRACT

Recent research trends in chemical and biological sensing have been geared toward developing molecular sensor devices that are fast, inexpensive, miniaturized, have low power consumption and are portable. The performance of these devices can be dramatically improved by utilizing multimodal detection techniques, new materials and nanofabrication technologies. To develop such sensor devices, we utilized Indium Nitride (InN) nanowires (NWs) to fabricate nanoelectromechanical system (NEMS) based sensors and Graphene/InN NW heterojunctions, and InN thin films to fabricate Graphene/InN thin film heterojunction based sensors. InN NWs, which exhibit interesting properties including high carrier density, superior electron mobility, strong surface charge accumulation, and chemical inertness, were synthesized using Chemical Vapor Deposition (CVD) technique by Vapor-Liquid-Solid (VLS) mechanism. A novel method for synthesis of high quality InN nanowires, at temperatures well above their decomposition temperature, has been demonstrated by utilizing controlled oxygen flow into the growth chamber. Detailed structural and chemical analyses indicate that the nanowires consist of pure InN, with no evidence of In_2O_3 detected by any of the characterization methods. It is proposed that the oxygen, pre-adsorbed on the Au catalyst surface, assists in accelerating the decomposition of NH_3 at the growth temperature by providing high concentration of atomic nitrogen to assist in the growth, and prevent decomposition of the InN nanowires, without getting incorporated in them. The proposed role of oxygen is supported by improved material quality at higher oxygen flow rates.

In a related research effort, Indium Nitride based heterojunction sensor devices were investigated. We designed and fabricated graphene/InN heterojunction devices that are suitable for gas sensing because of a tunable barrier height controlling the conductivity across the heterojunction in presence of different analyte gas and vapor molecules. Electrical characterization of the device demonstrated good rectifying behavior across the graphene/InN heterojunction. Preliminary sensing experiments carried out with trace amount of water and acetone vapors, as well as, NH_3 and NO_2 gases showed highly promising results. It is observed that this sensor offers better sensitivity than simple graphene or InN based conductometric sensors, primarily because of the presence of a tunable Schottky barrier formed between graphene and InN that can be modulated by different analyte gas molecules, which affects the junction current exponentially.

To explore promising alternative device approaches addressing the challenges posed by continuous shrinking of Si based device dimensions in integrated circuits, we investigated for the first time an InN NW/graphene heterojunction based vertical three-terminal active device, a variable barrier transistor or barristor, where the interfacial current between two terminals were controlled by an insulated gate. A very promising on/off ratio exceeding 100 was achieved by adjusting the gate voltage to control the graphene/InN NW heterojunction Schottky barrier, which underlines the promise of these devices in low power device and sensing applications.

TABLE OF CONTENTS

DEDICATION iii

ACKNOWLEDGEMENTS iv

ABSTRACT vi

LIST OF FIGURES x

CHAPTER 1 INTRODUCTION 1

1.1 Overview 1

1.2 Chemical sensor arrays 3

1.3 Classification of sensors 4

1.4 Applications of chemical sensors 8

1.5 Motivation 12

1.6 Outline of dissertation 13

CHAPTER 2 INDIUM NITRIDE NANOWIRES SYNTHESIS AND STRUCTURAL CHARACTERIZATION 16

2.1 Introduction 16

2.2 Why InN nanowires 17

2.3 InN nanowire synthesis 25

2.4 InN nanowire characterization 32

2.5 Growth optimization and the role of oxygen flow rate 39

2.6 Growth direction modulation 49

CHAPTER 3 INDIUM NITRIDE NW BASED SENSORS 52

3.1 Introduction 52

3.2 Field effect transistor fabrication 53

3.3 Electrical characterization 61

3.4 Sensing results 66

CHAPTER 4 INN NEMS BASED SENSORS **70**

4.1 Introduction 70

4.2 Suspended NWs fabrication 72

CHAPTER 5 GRAPHENE/INN THIN FILM BASED SENSORS **84**

5.1 Introduction 84

5.2 Fabrication of devices 86

5.3 Electrical characterization 88

5.4 Sensing results 89

CHAPTER 6 GRAPHENE/INN NW BASED SENSORS **94**

6.1 Introduction 94

6.2 Non-lithographic patterning of graphene on InN NW sample 96

6.3 Lithographic pattering of graphene on InN NW sample 98

6.4 Effect of partial oxidation of InN NWs: bias stressing 110

CHAPTER 7 CONCLUSION AND PROPOSED FUTURE WORK **113**

7.1 Summary 113

7.2 Proposed future work 115

REFERENCES **122**

APPENDIX A DEVICE FABRICATION **135**

LIST OF FIGURES

Figure 1.1 Various applications of chemical sensors.. 9

Figure 1.2 Environmental pollutants.. 12

Figure 1.3 CWA, indoor air and traffic pollution detection systems............................. 13

Figure 2.1 Atomic arrangements in In-face and N-face InN crystals. The red arrow pointing from N to In atom shows the direction of the spontaneous polarization (Ref. [35])... 20

Figure 2.2 (a) The conduction and valence band edges (E_C and E_V, solid lines) and the branch-point energy (E_B, dotted line) with respect to the Fermi level (E_F, dashed line) in the near-surface region of InN(0001). (b) The donor-type surface states (Dss) are also shown, where the unoccupied states above the Fermi level are shown to be positively charged.. 24

Figure 2.3 CVD system setup, pressure and mass flow controllers (MFCs), MFCs, temperature controllers and heated furnace.. 26

Figure 2.4 (a) SEM image of network of InN nanowires grown on Si/SiO_2 substrate. Scale bar is 3 μm. (b) SEM image of single InN nanowire grown on Si/SiO_2 substrate. Scale bar is 1 μm.. 28

Figure 2.5 (a) and (b) show optical micrographs of dense and non-uniform 3D networks of InN nanowires grown on Si/SiO_2 substrate... 29

Figure 2.6 Schematic band diagrams of (a) an as-grown InN nanowire, (b) an oxidized InN nanowire and (c) an overgrown InN nanowire with an In_2O_3 shell layer................. 32

Figure 2.7 (a) A typical SEM image showing InN nanowires as-synthesized on a SiO_2 /Si substrate. The inset shows image of a single NW. Scale bar is 100 nm. (b) High resolution TEM image of a single NW growing along the [110] direction. The inset shows the hexagonal FFT spectrum. (c) Lattice resolved TEM image shows the lattice spacing. (d) TEM image of a suspended NW showing good crystalline quality and lack of any significant oxide shell layer. 33

Figure 2.8 Energy Dispersive X-Ray Spectroscopy (EDS) mapping on a nanowire K-junction. (a) STEM Image of the K-junction. (b) In elemental mapping, (c) N elemental mapping and (d) O elemental mapping over the K-junction. The scale bar is 300 nm for (a) and 400 nm for (b) – (d). 35

Figure 2.9 Adjusted EDS spectrum of a thin InN NW with contribution from SiO_2 membrane subtracted. Top left inset shows EDS spectra on InN NW and SiO_2 membrane. Top right inset shows TEM image with positions 1 and 2 where EDS spectra were taken. 36

Figure 2.10 (a) Raman spectrum of the InN NW junction showing peaks at 443, 491 and 594 cm^{-1}, which correspond to the A_1(TO), E_2 (high) and A_1(LO) phonon peaks, respectively. (b) Raman spectrum of the bare SiO_2 membrane without NWs. Inset shows Raman spectra taken on commercial In_2O_3 sample. 38

Figure 2.11 Position of Boron Nitride during growth at 0 mm, 28 mm, 51 mm, 76 mm, 102 mm and 117 mm away from the center of furnace. 41

Figure 2.12 Temperature profile for 5 different segments: 700 °C, 704 °C, 708 °C, 712 °C and 716 °C. 41

Figure 2.13 Temperature-time curve for InN NW synthesis using a CVD furnace. 42

Figure 2.14 SEM images showing NW morphologies at different dilute oxygen flow rates: (a) 0 sccm, (b) 2.0 sccm, (c) 4.0 sccm, (d) 8.0 sccm, (e) 10.0 sccm and (f) 14.0 sccm. 45

Figure 2.15 HTREM images of single NWs (on 40 nm SiO_2 membranes) grown at different oxygen (3% in balance N_2) flow rates: (a) 2 sccm; (b) 4.0 sccm; (c) 10.0 sccm; (d) 14.0 sccm. Careful observation shows lattice planes in the images. Insets in the images show the respective hexagonal FFT spectra. Bottom left inset of (c) shows a typical SiO_2 membrane window with NWs growing from catalyst spots on the Si support to the SiO_2 membrane. 47

Figure 2.16 Energy Dispersive Spectroscopy (EDS) mapping on section of a partially decomposed nanowire grown with 4 sccm of oxygen flow. (a) STEM Image, (b) In elemental mapping, (c) N elemental mapping and (d) O elemental mapping along the nanowire. The scale bar is 300 nm for all sub parts... 48

Figure 2.17 Energy Dispersive Spectroscopy (EDS) mapping around a NW K-junction. The growth was performed with an oxygen flow rate of 10 sccm. (a) STEM Image, (b) In elemental mapping, (c) N elemental mapping and (d) O elemental mapping around the K-junction. The scale bar is 300 nm for all sub parts. 49

Figure 2.18 SEM images showing (a) spontaneous bending of InN NW, as well as bending caused by (b) two InN NW guides (c) lithographically deposited 100 nm SiO2 barriers and (d) Lattice resolved TEM images of a NW showing atomic arrangement as the growth direction is changed from [110] to another [$1\bar{1}0$], inset shows schematic diagram of atomic configurations for 60° (similar to 120°) bend................................... 51

Figure 3.1 Schematic of the basis procedures of optical lithography process for catalyst patterns. The size of the lines is 3 µm x 30 µm, and the circle diameter is 3 µm............ 56

Figure 3.2 Optical images of 2 nm Au pattern. (a) Size of lines is 3 µm x 30 µm and the diameter of the circles is 3 µm. (b) The size of the patter is 50 µm x 50 µm.................. 57

Figure 3.3 SEM image for a network of NW. Scale bar is 10 µm................................ 58

Figure 3.4 SEM image of InN NW FET with source and drain contact deposited on each side of the nanowire.. 60

Figure 3.5 (a) I_dV_d curves for InN NW FET at gate bias voltages varying from 0 to -15 V with intervals of -2.5 V and (b) I_dV_g curve measured at Vd = 1 V.............................. 62

Figure 3.6 SEM image of NW overhang from the edge of the sample.......................... 64

Figure 3.7 Schematic of experimental set up for the field emission studies from the InN NWs. 64

Figure 3.8 I-V curve showing field emission of InN NWs starting at different voltages. The inset shows the field emission for a single InN NW. 66

Figure 3.9 Schematic diagram of (a) single InN NW FET and (b) multiple InN NW FET. 67

Figure 3.10 Picture of sensing setup showing the device under test (DUT) and the gas flow line. 68

Figure 3.11 Sensing results using InN NW FET with (a) acetone vapor and (b) water vapor. 69

Figure 4.1 SEM image of a suspended Pt NW with 1.3 µm length and diameter of 43 nm (Ref. [68]). 70

Figure 4.2 (a) A part of a NW, and (b) a complete NW hanging over a trench etched post NW growth. Note that the NWs are hanging shallowly as the SiO2 is also etched along the NW. 74

Figure 4.3 Optical image showing trench patterns after exposure and the rest of the sample being covered with PMMA. 75

Figure 4.4 Trench etched on the SiO_2 layer, with (a) multiple InN NWs going across and (b)-(d) single NW going across trench........ 76

Figure 4.5 Schematic diagram of a RIE system (Ref. [80])........ 77

Figure 4.6 SEM images of NWs etched by RIE. (a) sample A from top, no tilt, (b) - (c) sample A tilted 40°, (d) sample B tilted 40°, (e) sample C tilted 40°........ 79

Figure 4.7 SEM image of InN NW etched (a) by RIE, tilted 40°, (b) by RIE and BOE vapor etch without tilt and (c) by RIE and BOE vapor etch, tilted 40°. 80

Figure 4.8 SEM image of InN NW etched (a) by RIE, tilted 40°, (b) by RIE and BOE vapor etch without tilt and (c) by RIE and BOE vapor etch, tilted 40°. 81

Figure 4.9 (a) SEM image of trenches made using e-beam lithography, with multiple Au catalyst spots patterned around them. (b) A magnified image of a trench pattern with Au catalyst spots around it. (c) NWs growing randomly from catalyst spots deposited near a pre-patterned trench. (d) A single suspended NW going over the trench........ 83

Figure 5.1 Schematic diagram of the graphene/InN sensor. Inset shows a photograph of the device before putting contacts, graphene is coated with PMMA. 88

Figure 5.2 Graphene/InN junction I-V characteristics which exhibits Schottky behavior........ 89

Figure 5.3 Water vapor sensing by graphene/InN thin film sensor under a bias voltage of 0.5V........ 90

Figure 5.4 Water vapor sensing by InN thin film sensor under a bias voltage of 0.5V. "1" and "2" denotes the beginning and stopping of the water vapor flow. 91

Figure 5.5 Diluted acetone vapor (100 ppm) sensing by graphene/InN sensor under -5V bias. "1" and "2" denotes the beginning and stopping of the acetone vapor flow........ 91

Figure 5.6 Sensing responses for (a) NO_2 and (b) NH_3 gas for graphene/InN thin film device under a voltage bias of 1V. 93

Figure 6.1 Optical image of graphene/InN NW heterojunctions. 97

Figure 6.2 Graphene/InN NW heterojunction I-V characteristics which exhibits Schottky behavior. 98

Figure 6.3 InN NWs grown out of 2 nm Au catalyst (catalyst pattern dimensions: 5 µm x 100 µm and 5 µm x 200 µm). 100

Figure 6.4 Optical microscope images of (a) optical lithography pattern of metal contacts and (b) 20nm/80nm Cr/Au metal contacts deposited by e-beam evaporator (metal contact dimensions, B25: 50µm x 160 µm, A35: 50 µm x 260 µm). 101

Figure 6.5 Optical image of patterned photoresist on graphene. 102

Figure 6.6 Optical images of (a) 2 devices and (b) multiple devices, after graphene transfer, graphene etch and resist removal. 103

Figure 6.7 I-V characteristics for (a) InN NW/graphene heterostructure with inset showing the schematic diagram of the device and (b) graphene field effect transistor with inset showing the schematic diagram of the measurement. 105

Figure 6.8 (a) I_d-V_d curves for graphene/InN NW heterostructure at gate bias voltages varying from -20 V to 20 V(the inset shows the schematic diagram of the measurement setup), (b) shows the magnitude of current in log scale for the data shown in (a). 108

Figure 6.9 (a) I_d-V_g curve measured at drain voltages varying from -2 V to 2V, (b) shows the magnitude of current in log scale for the data shown in (a). 109

Figure 6.10 I-V characteristics of partially oxidized InN NW/graphene heterojunction, having the voltage swept from positive to negative and negative to positive direction. 110

Figure 6.11 Effect of bias stressing and oxide charge trapping on the transient behavior of the partially oxidized InN NW/graphene heterojunction. 112

Figure 7.1 Schematic representation of NEMS resonator with contacts traced using FIB. 116

Figure 7.2 Proposed FIB method on NW grown on already etched trench. 116

Figure 7.3 Optimization of InN NW release. (a) Shows a schematic diagram of trench etch using RIE and (b) shows a schematic diagram of NW release after etching the SiO_2 with HF vapor. 117

Figure 7.4 Graphene/ InN NW barristor configuration.. 118

Figure 7.5 Reactive ion etch system used for NW oxidation....................................... 119

Figure 7.6 Graphene/InN NW heterojunction sensing setup (a) showing how the probes are placed on the sample and (b) showing a close-up of the device. 121

LIST OF TABLES

Table 2.1 Summary of properties for III-V Nitride semiconductors.............................. 18

Table 2.2 Lattice parameters of wurtzite III-V nitrides at 300 K................................... 21

Table 2.3 Effects of lattice non-ideality on the strength of spontaneous polarization in the III-V nitrides. 22

CHAPTER 1

INTRODUCTION

1.1 Overview

Detection of small quantities of molecules is of significant interest for numerous numbers of applications, ranging from gas sensing and environmental monitoring to biological and medical diagnostics. These require the sensors to be inexpensive, power efficient, easily deployable and miniaturized, yet sensitive enough to detect molecules down to the single-molecule level. With the advancement of miniaturization technologies molecular sensors are getting smaller and smaller in dimensions. Conventional molecular sensors suffer from extensive packaging, complex electronic interfacing and regular maintenance, the use of novel Microelectromechanical system (MEMS) devices that integrate electronics and micro-mechanical structures on chip could address all those drawbacks.

Microcantilevers are the most simplified MEMS based devices. Diverse applications of microcantilevers in the field of sensors have been explored by many researchers. These sensors have several advantages over the conventional techniques in terms of high sensitivity, low cost, simple procedure, non-hazardous procedures and quick response. Moreover, the technology has been developed in the last few years for the fabrication and use of *Nanocantilevers* for sensing applications, thereby giving rise to *Nanoelectromechanical systems (NEMS)*. This development has increased the sensitivity

limit up to the extent that researchers have now started visualizing the counting of molecules.

A molecular sensor is usually evaluated with respect to three major aspects: 1) sensitivity, 2) selectivity, and 3) size. An ideal sensor should have high sensitivity towards targeting chemicals, excellent selectivity to a specific signal of interest, and a very small dimension.

Particles that are smaller than the characteristic lengths associated with the specific phenomena often display new chemistry and new physics that lead to new properties that depend on size. The sensing elements, for example nanowires, have the surface area the same as the gas molecules that are exposed to and they exhibit new chemistry and physics compared to bulk InN, developing new sensing mechanisms. Because of their size, the surface to volume ratio is increased. This enhances the sensitivity even more since the molecular interaction or sensing occurs at the surface.

The careful selection of superior material quality confirms the fast response. *InN nanowires*, which have been investigated only in the last few years, exhibit such superior material properties in terms of sensing including high carrier density, high electron mobility, surface charge accumulation and chemical inertness. In this work we are proposing using InN for NEMS based sensors and also for heterojunction based sensors. NEMS resonators have the potential to have significant impact in various applications such as ultra-high resolution mass detection, force detection, electromechanical signal generation and processing and biosensing. On the other hand, Graphene/InN heterostructure based sensors offer the possibility of surface barrier modulation and high detection sensitivity, making these devices suitable for sensing applications.

1.2 Chemical sensor arrays

A chemical sensor is a device that transforms chemical information, ranging from the concentration of a specific sample component to total composition analysis, into an analytically useful signal. The chemical information, mentioned above, may originate from a chemical reaction of the analyte or from a physical property of the system investigated.

A physical sensor is a device that provides information about a physical property of the system. A chemical sensor is an essential component of an *analyzer.* In addition to the sensor, the analyzer may contain devices that perform the following functions: sampling, sample transport, signal processing, data processing. An analyzer may be an essential part of an automated system. The analyzer working according to a sampling plan as a function of time acts as a monitor.

Chemical sensors contain two basic functional units: a receptor part and a transducer part. Some sensors may include a separator which is, for example, a membrane. In the *receptor* part of a sensor the chemical information is transformed into a form of energy which may be measured by the transducer [1].

The *transducer* part is a device capable of transforming the energy carrying the chemical information about the sample into a useful analytical signal. The transducer as such does not show selectivity.

The receptor part of chemical sensors may be based upon various principles:

- Physical, where no chemical reaction takes place. Typical examples are those based upon measurement of absorbance, refractive index, conductivity, temperature or mass change.

- Chemical, in which a chemical reaction with participation of the analyte gives rise to the analytical signal.
- Biochemical, in which a biochemical process is the source of the analytical signal. Typical examples are microbial potentiometric sensors or immune-sensors. They may be regarded as a subgroup of the chemical ones. Such sensors are called *biosensors.*

In some cases it is not possible to decide unequivocally whether a sensor operates on a chemical or on a physical principle. This is, for example, the case when the signal is due to an adsorption process.

Sensors are normally designed to operate under well-defined conditions for specified analytes in certain sample types. Therefore, it is not always necessary that a sensor responds specifically to a certain analyte. Under carefully controlled operating conditions, the analyte signal may be independent of other sample components, thus allowing the determination of the analyte without any major preliminary treatment of the sample. Otherwise unspecific but satisfactory reproducible sensors can be used in series for multicomponent analysis using multivariate calibration software and signal processing. Such systems for multicomponent analysis are called sensor arrays.

1.3 Classification of sensors

The development of instrumentation, microelectronics and computers makes it possible to design sensors utilizing most of the known chemical, physical and biological principles that have been used in chemistry.

Chemical sensors may be classified according to the operating principle of the transducer [1]:

1. *Optical devices* transform changes of optical phenomena, which are the result of an interaction of the analyte with the receptor part. This group may be further subdivided according to the type of optical properties which have been applied in chemical sensors:

a) Absorbance, measured in a transparent medium, caused by the absorptivity of the analyte itself or by a reaction with some suitable indicator.

b) Reflectance is measured in non-transparent media, usually using an immobilized indicator.

c) Luminescence, based on the measurement of the intensity of light emitted by a chemical reaction in the receptor system.

d) Fluorescence, measured as the positive emission effect caused by irradiation. Also, selective quenching of fluorescence may be the basis of such devices.

e) Refractive index, measured as the result of a change in solution composition. This may include also a surface plasmon resonance effect.

f) Optothermal effect, based on a measurement of the thermal effect caused by light absorption.

g) Light scattering, based on effects caused by particles of definite size present in the sample.

2. *Electrochemical devices* transform the effect of the electrochemical interaction analyte – electrode into a useful signal. Such effects may be stimulated electrically or may result in a spontaneous interaction at the zero-current condition. The following subgroups may be distinguished:

a) Voltammetric sensors, including amperometric devices, in which current is measured in the DC or AC mode. This subgroup may include sensors based on

chemically inert electrodes, chemically active electrodes and modified electrodes. Sensors with and without (galvanic sensors) external current source are also part of this group.

b) Potentiometric sensors, in which the potential of the indicator electrode (ion-selective electrode, redox electrode, metal/meta1 oxide electrode) is measured against a reference electrode.

c) Chemically sensitized field effect transistor (CHEMFET) in which the effect of the interaction between the analyte and the active coating is transformed into a change of the source-drain current. The interactions between the analyte and the coating are, from the chemical point of view, similar to those found in potentiometric ion-selective sensors.

d) Potentiometric solid electrolyte gas sensors, differing from class 2(b) because they work in high temperature solid electrolytes and are usually applied for gas sensing measurements.

3. *Electrical devices* based on measurements, where no electrochemical processes take place, but the signal arises from the change of electrical properties caused by the interaction of the analyte.

a) Metal oxide semiconductor sensors used principally as gas phase detectors, based on reversible redox processes of analyte gas components.

b) Organic semiconductor sensors, based on the formation of charge transfer complexes, which modify the charge carrier density.

c) Electrolytic conductivity sensors.

d) Electric permittivity sensors.

4. *Mass sensitive devices* transform the mass change at a specially modified surface into a change of a property of the support material. The mass change is caused by accumulation of the analyte.

a) Piezoelectric devices used mainly in gaseous phase, but also in solutions, are based on the measurement the frequency change of the quartz oscillator plate caused by adsorption of a mass of the analyte at the oscillator.

b) Surface acoustic wave devices depend on the modification of the propagation velocity of a generated acoustical wave affected by the deposition of a definite mass of the analyte.

5. *Magnetic devices* based on the change of paramagnetic properties of a gas being analyzed. These are represented by certain types of oxygen monitors.

6. *Thermometric devices* based on the measurement of the heat effects of a specific chemical reaction or adsorption which involve the analyte. In this group the heat effects may be measured in various ways, for example in the so called catalytic sensors the heat of a combustion reaction or an enzymatic reaction is measured by use of a thermistor. The devices based on measuring optothermal effects can alternatively be included in this group.

This classification represents one of the possible alternatives. Sensors have, for example, been classified not according to the primary effect but to the method used for measuring the effect. As an example can be given the so-called catalytic devices in which the heat effect evolved in the primary process is measured by the change in the conductivity of a thermistor. Also, the electrical devices are often put into one category together with the electrochemical devices.

Sensors have also been classified according to the application to detect or determine a given analyte. Examples are sensors for pH, for metal ions or for determining oxygen or other gases. Another basis for the classification of chemical sensors may be according to the mode of application, for example sensors intended for use in vivo, or sensors for process monitoring and so on. It is, of course, possible to use various classifications as long as they are based on clearly defined and logically arranged principles.

The biosensors are not presented as a special class because the process on which they are based is, in general, common to chemical sensors. They may be also differentiated according to the biological elements used in the receptor. Those may be: organisms, tissues, cells, organelles, membranes, enzymes, antibodies, etc. The biosensors may have several enzymatic systems coupled which serve for amplification of the signal.

1.4 Applications of chemical sensors

Figure 1.1 shows various applications of chemical sensors including monitoring automobile emission gasses, medical diagnosis, industrial control, national security, indoor air quality control, and environmental evaluation.

The regulation on *automobile emission* usually involves toxic gases such as nitrogen oxide (NOx), carbon monoxide (CO), or volatile hydrocarbons.

A *general medical* examination requires measuring these substances in human body such as glucose, blood oxygen, and cholesterol, which lead to determine possible disease or disorder of a patient.

In a research lab or industrial factory, it is extremely important to prevent accidents from leakage of *flammable gases such as H_2*, thus the concentration of H_2 on working sites needs to be monitored in real-time.

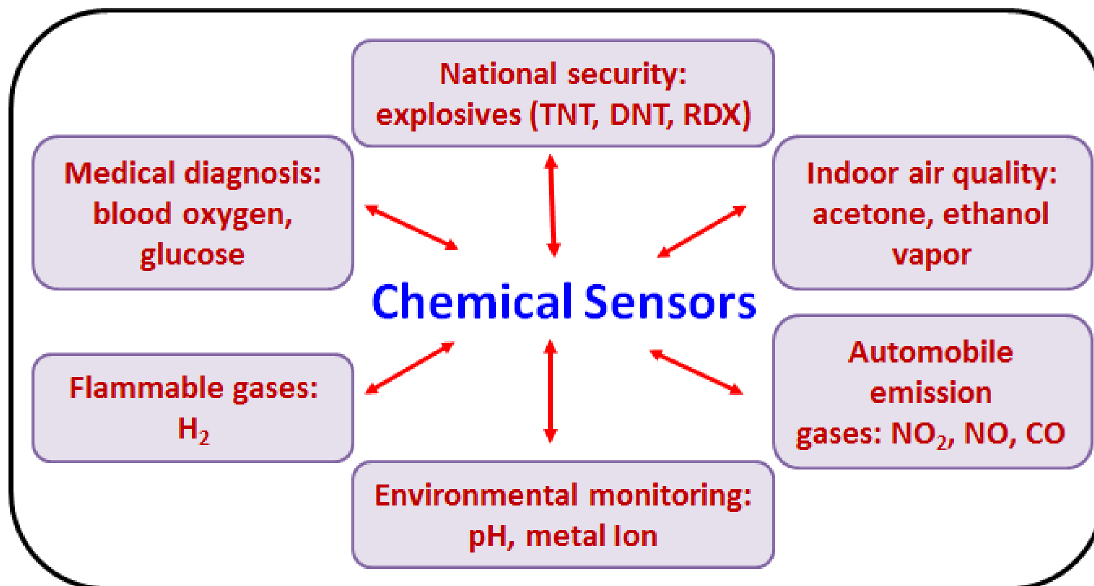

Figure 1.1 Various applications of chemical sensors.

There are *indoor air pollutants* such as *volatile organic compounds* (VOCs) including acetone, ethanol and isopropanol. These organic compounds are widely used as ingredients in household products and extensive exposure to these VOCs can lead to disorder, sickness or even death [2].

Particularly, there have been significant increasing technical demands on identifying *explosive chemicals*_due to challenges of anti-terrorism worldwide. Sensors are required to be deployed at public transport station, plaza, schools, and commercial buildings to detect trace amount of explosive molecule such as TNT, DNT, and RDX [3]. Apart from explosive chemicals, recently in last few decades there have been several

incidents of the use of *CWAs* (mustard gas, sarin, etc.) around the world that killed thousands of lives and threatened the whole civilization [4]. These incidents worldwide highlight the importance of having a continuous detection and monitoring of these kinds of chemical agents and explosives for both defense and homeland security.

Chemical sensors are expected to play a critical role in environmental monitoring (both indoor and outdoor) and environmental control (air, water), facilitating a better quality of life. The projected increase in global energy usage and unwanted release of pollutants has led to a serious focus on advanced monitoring technologies for environmental protection, remediation, and restoration. In a recent study, the World Health Organization (WHO) reported that over 3 million people die each year from the effects of air pollution. Furthermore, reports from World Energy Congress (WEC) suggest that if the world continues to use fuels reserves at the current rate, the environmental pollution in 2025 will create irreversible environmental damage. Long-term exposure to air pollution provokes inflammation, accelerates atherosclerosis, and alters cardiac function. Within the general population, medical studies suggest that inhaling particulate matter (PM) is associated with increased mortality rates which are further magnified for people suffering from diabetes, chronic pulmonary diseases, and inflammatory diseases. Pollution, in general is contamination that renders part of the environment unfit for intended or desired use. Natural processes release toxic chemicals into the environment as a result of ongoing industrialization and urbanization. Major contributors to large-scale pollution crisis are deforestation, polluted rivers, and contaminated soils. Other sources of pollution include emissions from iron and steel mills; zinc, lead, and copper smelters; municipal incinerators; oil refineries; cement

plants; and nitric and sulphuric acid producing industries. Of the group of pollutants that contaminate urban air, nitrous oxide (NO_x), fine suspended PM, Sulphur dioxide (SO_2), and ozone pose the most widespread and acute risks. Recent studies on the effects of chronic exposure to air pollution have singled out PM suspended in smog (NO_x) and volatile organic compounds (VOCs) as the pollutant most responsible for life-shortening respiratory and associated health disorders. Since the Clean Air Act was adopted in 1970, great strides have been made in the U.S. in reducing many harmful pollutants from air, such as SO_2. Levels of NO_x, however, have increased by 20% over the last 30 years. Sources of NO_x include passenger vehicles, industrial facilities, construction equipment and railroads, but of the 25 million tons of NO_x discharged annually in the U.S., 21% of that amount is generated by power plants alone, resulting in rising threats to the health of the general population. Furthermore, the SCanning Imaging Absorption spectroMeter for Atmospheric CHartographY (SCIAMACHY), shows rapid increase in NO_x columns worldwide, especially since 2003.

Rapid detection of contaminants in the environment by emerging technologies is of paramount significance. Environmental pollution in developing countries has reached an alarming level thus necessitating deployment of real-time pollution monitoring sensors, sensor networks, and real-time monitoring devices and stations to gain a thorough understanding of cause and effect. A tool providing interactive qualitative and quantitative information about pollution is essential for policy makers to protect massive populations, especially in developing countries.

1.5 Motivation

There are a lot of different pollutants that affect us on a daily basis. The smoke and fumes from cars and power plants emit nitrogen dioxide (NO_2) and sulphur dioxide (SO_2), which increase the risk of asthma, lung damage and premature death. These gases are also responsible for acid rain, which is hazardous to humans, plants and animals (**Figure 1.2**).

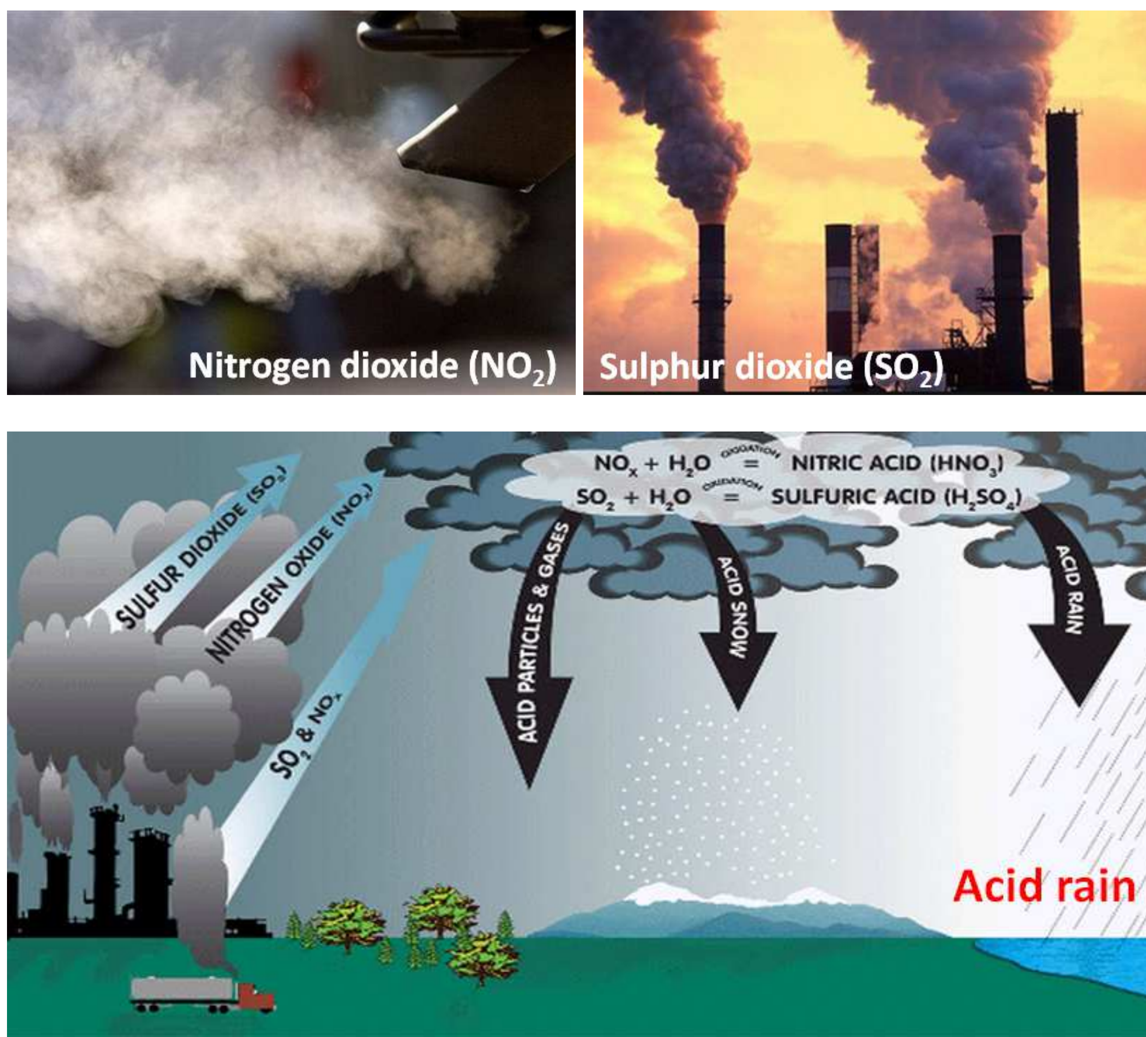

Figure 1.2 Environmental pollutants.

Few sensing techniques have been developed throughout the years, not only for pollutants but also for chemical welfare agents (CWA). Some of these techniques are

indoor air pollution monitoring and testing, CWA detection sensors and remote traffic pollution detection system, ion mobility spectrometer mainly used in airports to detect unwanted chemicals (**Figure 1.3**).

Figure 1.3 CWA, indoor air and traffic pollution detection systems.

The problem with these sensors is that they are bulky, expensive, have slow response and have high power consumption. Few promising methods for gas sensing have been developed throughout the years, such as nanowires, nanotubes or semiconductor resistor based sensors. The nanoscale sensors are one of the solutions to the above mentioned problems because they are light, miniaturized, inexpensive, highly sensitive, they have ultra-low power consumption and most importable they are portable.

1.6 Outline of dissertation

This dissertation is aimed to develop nanoscale size devices used for gas detection using InN nanowires, InN thin films and graphene. The dissertation is organized in such way that even a non-expert can get familiar with the basics and be able to explore into the deep of the topic. For this, attempts have been made to include relevant review topics and separate each matter in individual chapters. Thus, the dissertation is divided in two major parts: InN NEMS based sensors (Chapter 4), graphene/InN heterojunction based sensors (Chapters 5 and 6).

After the introduction chapter, the dissertation starts in chapter 2 with introduction to semiconductor nanowires, indium nitride and InN NWs. Growth system and nanowire synthesis will be explained in detail in this chapter, followed by structural characterization and chemical composition. The role of oxygen during the growth and the growth direction modulation, two of the most important aspects of this work based on InN NWs, are explained thoroughly.

Chapter 3 exclusively focuses on the fabrication of InN NW field effect transistors (FETs), and the methods used to fabricate single and multiple NW FETs. Also, the results of our field emission study which shows interesting tunneling effect in our InN NW FET devices will also be deliberated and explained. Electrical characterization and sensing results of InN NW FET will also be presented in this chapter.

Chapter 4 is dedicated to InN NEMS based sensors. This chapter presents a brief introduction to the current status and challenges of nanocantilever fabrication found from literature. Three different approaches were investigated in order to fabricate InN NEMS based sensors, which will be explained in this section.

The second major topic of this dissertation will start with Chapter 5 discussing about electrical characterization and sensing results for InN thin film/graphene based sensors and continue with Chapter 6, which will cover electrical characterization, such as current-voltage results, effect of NW oxidation and sensing results for InN NW/graphene based sensors. The fabrication steps and graphene transfer procedures for each type of heterostructure will also be covered in these chapters. For the first time an InN NW/graphene heterojunction based on vertical three-terminal active device is investigated and the full details are covered also in Chapter 6.

Chapter 7 summarizes all the major contributions of this work to the research community. In this chapter we also propose future extension of this work and further development.

CHAPTER 2

INDIUM NITRIDE NANOWIRES SYNTHESIS AND STRUCTURAL CHARACTERIZATION

2.1 Introduction

Nanoscale sensors, in various forms, have been under intense research focus in the past several years due to their high sensitivity toward changes in many physical parameters such as, mass [5], force [6], energy [7], stress [8], temperature [9], charge [10], and spin [11]. Additionally, these systems promise high integration density and low power consumption, two of the most desirable aspects of an integrated system [12]. A combination of all these properties can lead to potential applications of these sensors in a large variety of civilian and military applications. There are currently two approaches for nanoscale sensor fabrication: top-down and bottom-up. In the top-down approach, one uses expensive and complicated fabrication processes to realize the nanostructures, which limits their applications to only very specific and niche areas. In the bottom-up approach, the nanostructures are realized through inexpensive NW synthesis processes that can open up opportunities for widespread applications. In addition, the uniformity and quality of the nanostructures (which seriously impact the device characteristics) that are naturally obtained during the synthesis process cannot be achieved by current state-of-the-art nanofabrication tools. However, controlled positioning of the NWs over a large area has

been quite difficult to achieve so far, restricting their applications to individual devices, or to low levels of integration.

2.2 Why InN nanowires

One dimensional nanostructures, such as nanowires and nanotubes, possess unique physical properties that are fundamentally different from their bulk or thin film counterparts, enabling them to serve as basic building blocks for novel nanoscale devices [13]. Among various nanostructures, semiconducting nanowires (NWs) have attracted increasing interest due to their predictable material properties, controllable carrier density, and potential for applications in electronic and photonic devices. Group III-V Nitride (Al, Ga, In)N semiconducting NWs are highly promising for optoelectronic and high power electronic devices as well as chemical sensors due to their unique material properties including wide range of direct bandgap, spontaneous and piezoelectric polarization, high electron mobility, chemical inertness and high mechanical strength [1]-[17] (important material properties for III-V nitride semiconductors are summarized in **Table 2.1**). Due to its narrow bandgap [18]-[19], high predicted [20]-[21] and measured electron mobility [22], high saturation velocity, surface band bending and surface electron accumulation [23]-[25], InN NWs are highly promising for applications in high speed electronic devices and nano-electromechanical systems (NEMS).

Over the last several years significant research efforts have been focused on obtaining high quality single crystalline InN NWs. Several methods have been developed for the synthesis of InN nanostructures; including InN nanowires and nanotubes from vapor–solid mechanism [26], template assisted nanowire arrays [27], and vapor-liquid-solid (VLS) mechanisms [28]. Dingman *et al.* first reported synthesis of InN NWs from a

precursor based on the vapor–liquid–solid (VLS) mechanism at low temperature [29]. More recently, Cai *et al.* reported the growth of InN NWs by chemical vapor deposition

Table 2.1 Summary of properties for III-V Nitride semiconductors.

Properties[a]	***InN***	***GaN***	***AlN***
Bandgap (eV)	0.7	3.42	6.2
Lattice Constant (Å)	$a_0 = 3.533$ $c_0 = 5.693$	$a_0 = 3.189$ $c_0 = 5.178$	$a_0 = 3.111$ $c_0 = 4.979$
Electron Mobility (cm^2/Vs)	3200	900	300
Saturation Velocity ($\times 10^7$ cm/s)	2.5	1.4	1.6
Spontaneous Polarization (C/m^2)	– 0.032	– 0.029	– 0.081
Piezoelectric Polarization (C/m^2)	$e_{33} = + 0.97$ $e_{31} = – 0.57$	$e_{33} = + 0.73$ $e_{31} = – 0.49$	$e_{33} = + 1.46$ $e_{31} = – 0.60$

[a]Refs. [34], [58]-[61].

technique at around 550 ºC by the direct reaction between metallic Indium and ammonia with Au catalyst [30]. Unfortunately, the synthesis of high quality InN is fundamentally challenging since its thermal decomposition temperature (500 – 600 °C) [31] is lower than that of NH_3, which provides the atomic nitrogen (N) precursor. Thus, synthesis of InN is generally carried out at temperatures below 550 °C, and typically yields inhomogeneous nanowires with uncontrolled growth direction, low growth rates (a few microns/hour), nonuniform cross-sections, and large variations in NW material properties. To obtain high quality NWs, different approaches have been adopted for generating a steady supply of atomic nitrogen by increasing the NH_3 cracking efficiency. Most significant among them involve the usage of RF plasma to enhance NH_3

dissociation *in situ*, or utilization of two zone furnace, where NH_3 is cracked efficiently in the high temperature zone before being transported to the growth zone maintained at a lower temperature [32]-[33]. Although useful, these techniques are cumbersome and add significantly to the cost of material synthesis. Cai *et al.* first reported the planar growth (on the plane of the substrate) of high quality InN NWs by chemical vapor deposition (CVD) technique through direct reaction between metallic In and NH_3 with Au catalyst [30] using a single zone furnace without RF plasma attachment. However, an extremely narrow set of parameters governed the synthesis of these high quality NWs, which made it challenging to perform synthesis over an extended period of time maintaining the material quality. Before explaining the synthesis of InN nanowires, the physics of InN will be clarified in the next few sub-chapters.

2.2.1 InN wurtzite structure

Group III-nitride has two phase structures: α-phase and β-phase. The hexagonal wurtzite structure, α-phase, is the thermodynamically stable phase and the zincblende structure, β-phase, corresponds to the metastable phase, such as AlN, GaN and InN [34]. The wurtzite structure consists of tetrahedrally coordinated indium and nitrogen atoms that are stacked in an ABABAB pattern (Zincblende is stacked in an ABCABC pattern). In this structure, each atom is tetrahedrally bonded to four atoms of the other type, and the primitive unit cell is simple hexagonal with a basis of four atoms, two of each kind. The inversion symmetry in this lattice along [001] direction does not exist, which results in having all atoms on the same plane at each side of a bond being the same. Due to this, InN crystal has two distinct faces, the In-face and the N-face. The arrangement of atoms

for In-face and N-face InN are shown in **Figure 2.1**. Note that for In-face the N-atom is stacked directly over the In-atom and vice-versa for the N-face.

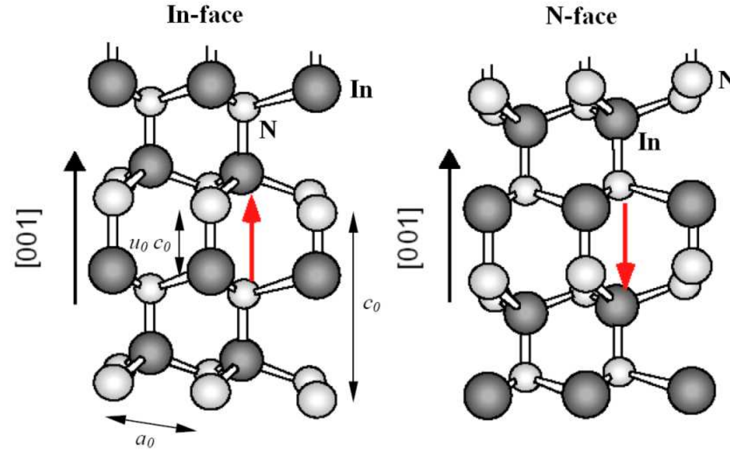

Figure 2.1 Atomic arrangements in In-face and N-face InN crystals. The red arrow pointing from N to In atom shows the direction of the spontaneous polarization (Ref. [35]).

The wurtzite lattice is characterized by three parameters: the edge length of the basal hexagon (a_0), the height of the hexagonal lattice cell (c_0), and the cation-anion bond length ratio (u_0) along the [001] axis in units of c_0. The subscript "0" indicates these values are those of the equilibrium lattice. These dimensions are marked in **Figure 2.1**. In an ideal wurtzite crystal structure, the c_0/a_0 ratio is 1.6330 and u_0 is 0.375. Because of the different metal cations, the bond lengths and the resultant c_0/a_0 ratio of AlN, GaN and InN are different (as listed in **Table 2.2**). It is obvious from **Table 2.2** that among the group-III nitrides, InN is second closest to the ideal structure. This fact is very important because the degree of non-ideality is an important factor in determining the strength of polarization in group-III nitrides.

Table 2.2 Lattice parameters of wurtzite III-V nitrides at 300 K

Material	***Ideal***	***AlN***	***GaN***	***InN***
a_0 (Å)[b]	-	3.112	3.189	3.54
c_0 (Å)[b]	-	4.982	5.185	5.705
c_0/a_0 (exp.)[b]	-	1.6010	1.6259	1.6116
c_0/a_0 (cal.)[a]	1.6330	1.6190	1.6336	1.6270
u_0[a]	0.375	0.380	0.376	0.377

[a]Ref. [34]

[b]Ref. [36]

2.2.2 Spontaneous and piezoelectric polarizations

In the group-V elements, nitrogen is the smallest and the most electronegative atom, which has a great influence on the properties of the III-nitrides. Because of the $1s^2 2s^2 2p^3$ electronic configuration of the nitrogen atom, the electrons involved in the metal-nitrogen covalent bond will be strongly attracted by the coulomb potential of the nitrogen atomic nucleus. This means that the metal-nitrogen covalent bond will have stronger ionicity compared to other III-V covalent bonds. This ionicity will result in macroscopic polarization if there is a lack of inversion symmetry in the crystal.

As mentioned before, there is no inversion symmetry in the wurtzitic III-nitrides along the c-axis. Absence of this inversion symmetry, in addition to the strong ionicity of the metal-nitrogen bond, results in a strong macroscopic polarization along the [001] direction in the III-nitrides, [34],[35]. This same effect also exists in the [111] direction of zincblende GaAs and InP, though to a much lesser extent because of the relatively smaller ionicity of the III-V covalent bond. Since this polarization effect occurs in the

equilibrium lattice of the III-nitrides at zero strain, it is called spontaneous polarization [34],[36].

Apart from the ionicity of the III-V covalent bond, the degree of non-ideality of the crystal lattice also affects the strength of spontaneous polarization. In III- nitrides, although the covalent bond parallel to the c-axis is strongly ionic and is primarily responsible for the spontaneous polarization, the other three covalent bonds in the tetrahedral structure are also equally ionic. The resultant polarization from these other three bonds is actually aligned in the opposite direction and serves to counteract the polarization of the other bond (see **Figure 2.1**). As the c_0/a_0 ratio decreases (c_0 decreases and a_0 increases), these three covalent bonds will be at a wider angle from the c-axis, and their resultant compensation polarization will decrease, giving rise to a stronger macroscopic spontaneous polarization. **Table 2.3** shows the c_0/a_0 ratio and the spontaneous polarization for GaN, InN and AlN. We can see that as the lattice non-ideality increases (c_0/a_0 ratio decreases away from 1.6330 of the ideal lattice), the value of spontaneous polarization (P_{SP}) increases from GaN to InN to AlN.

Table 2.3 Effects of lattice non-ideality on the strength of spontaneous polarization in the III-V nitrides.

Material	***AlN***	***GaN***	***InN***
c_0/a_0[a]	1.6010	1.6259	1.6116
P_{SP} (C/m^2)[a]	-0.081	-0.029	-0.032

[a]Ref. [34],[35].

Following the previous discussion on lattice non-ideality influencing the strength of spontaneous polarization, one can imagine that if the ideality of the III-nitride lattices is changed externally, then due to the strong ionicity of the metal-nitrogen covalent bond

there will be dramatic changes in the polarization of the crystal. One way to change the ideality of the crystal lattice is through strain. If stress is applied to the III-V nitride lattice, the ideal lattice parameters c_0 and a_0 of the crystal structure will change to accommodate the stress. Thus the polarization strength will be changed. This additional polarization in strained III-nitride crystals, in addition to the spontaneous polarization already present, is called piezoelectric polarization [34], [36]. For example, if the nitride crystal is under biaxial compressive stress, the in-plane lattice constant a_0 will decrease and the vertical lattice constant c_0 will increase, making the c_0/a_0 ratio increase towards the ideal lattice value of 1.6330. This will decrease the polarization strength of the crystal, since the piezoelectric polarization and the spontaneous polarization will act in opposite directions. On the other hand, if the nitride crystal is under tensile stress, the in-plane lattice constant will increase and the vertical lattice constant will decrease, lowering the c_0/a_0 ratio further away from 1.6330. This will increase the overall polarization, since the piezoelectric and the spontaneous polarizations now act in the same direction.

2.2.3 Surface band bending and charge accumulation

Normally, depletion layers occur at III–V semiconductor surfaces, with the surface Fermi level located in the band gap at the G-point. This depletion of conduction electrons allows the ionized acceptor-type surface states to be neutralized, giving overall charge neutrality. Narrow band gap Group III-nitride semiconductors, such as InN, InAs and InSb, usually show an accumulation layer due to pinning of the Fermi level above the conduction band edge at the NW surface, while semiconducting GaN NWs show an depletion region due to pinning of the Fermi level below the conduction band edge at the

NW surface [37]. For the wurtzitic InN nanowires, polarization (polar direction [001]) is always directed perpendicularly to the NW growth direction [110], and is also perpendicular to the NW surface. Therefore, the Fermi level is pinned above the conduction band edge at the nanowire surface for InN nanowires due to the sheet charge caused by the polarizations, much like InN film. Therefore, the free electrons move to the surface and form a charge accumulation layer, combining with the accumulation charge caused by the spontaneous and piezoelectric polarizations in InN nanowires [34] [see schematic bandgap diagram of **Figure 2.2** (a)]. In addition, the pinning of the surface Fermi level at the same energy for a-plane (i.e. [110]) and both polarities of c-plane (i.e. [001] and [00$\bar{1}$]) InN means that the band bending close to the surface is very similar, resulting in similar near-surface charge profiles [38].

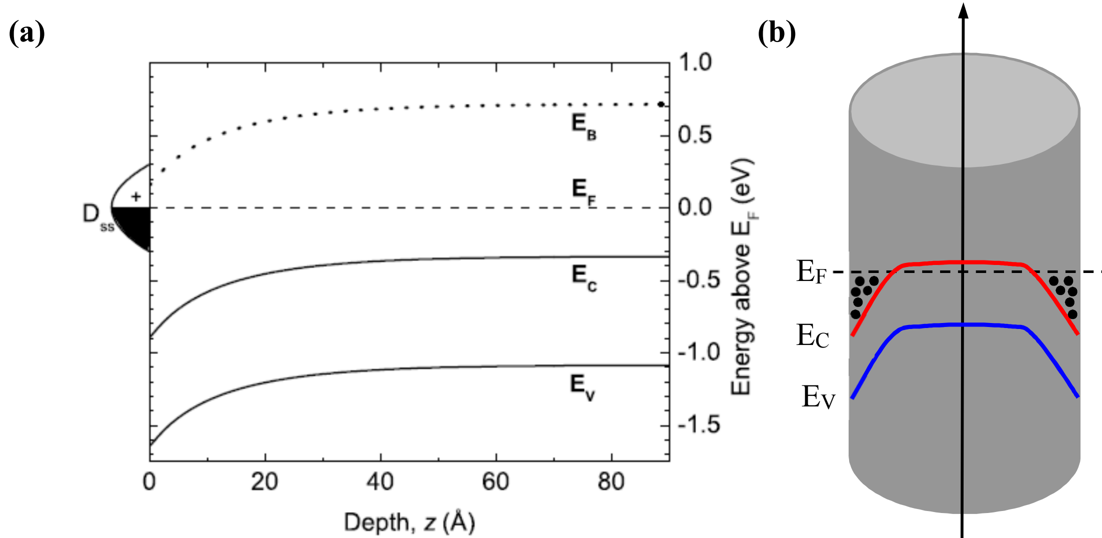

Figure 2.2 (a) The conduction and valence band edges (E_C and E_V, solid lines) and the branch-point energy (E_B, dotted line) with respect to the Fermi level (E_F, dashed line) in the near-surface region of InN(0001). (b) The donor-type surface states (Dss) are also shown, where the unoccupied states above the Fermi level are shown to be positively charged.

The observed electron accumulation at the surface of *n*-type InN is due to the presence of positively charged donor-type surface states. The existence of such surface states requires that the following conditions are satisfied. First, in order to have predominantly donor-type character, the surface states must lie below the branch-point energy E_B. This is the crossover point from states higher in the gap that are mainly of conduction band character (acceptor-type) to states lower in energy that are mainly of valence band character (donor-type) [38], [39]. This branch-point energy falls close to the center of the band gap (in one dimension) in the complex band structure [39]. Second, the surface states must be at least partly above the Fermi level, since valence band (donor-type) states are positively charged when unoccupied and neutral when occupied. The surface Fermi level can be pinned above the Γ--point conduction band minimum (CBM) by unoccupied, positively charged donor-type surface states. These donors acquire a positive surface charge by emitting electrons into the conduction band. This results in downward band bending and electron accumulation. This combined requirement that the surface states are ionized donors and lie above the Fermi level can be achieved only in *n*-type semiconductors when the Γ-point CBM lies significantly below E_B.

2.3 InN nanowire synthesis

Synthesis of InN NWs was carried out through chemical vapor deposition (CVD) using VLS mechanism in a high temperature horizontal quartz-tube furnace at a controlled temperature range through direct reaction between metallic In and NH_3 using Au as the catalyst (**Figure 2.3**). Lithographically patterned Au catalyst spots of 2 nm thickness were deposited by E-beam evaporation on SiO_2 (100 nm)/Si [n^+ (100)] substrate. The thickness and size of the patterned Au catalyst was optimized as they

strongly influence the quality of the NWs [40]. A boron nitride boat holding both the catalyst patterned substrate and In wire (99.999% purity, Aldrich) was placed inside the quartz tube. The substrate was placed ~4 mm downstream from the In wire along the gas flow direction. The growth was performed at a nominal temperature of 700 ˚C keeping the system pressure constant at 150 Torr for ~30 min. A mixture of 17 sccm N_2 (99.999% purity, National Welders) and 0-20 sccm dilute O_2 (3% in National Welders UHP balanced N_2) was flown over molten In, while the NH_3 (99.9995% purity, Matheson Tri-gas) flow rate was maintained at 100 sccm for optimal growth. A pre-growth flow of dilute oxygen at 7 sccm, while the temperature of the furnace was ramped up to the growth temperature, was also utilized to facilitate its adsorption on Au catalyst surface.

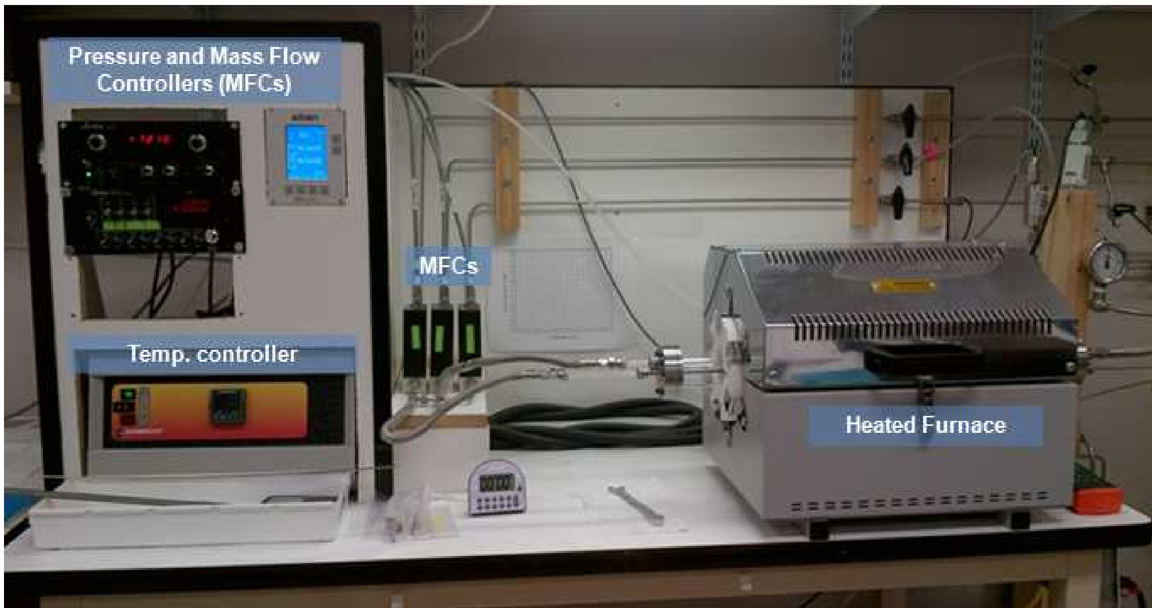

Figure 2.3 CVD system setup, pressure and mass flow controllers (MFCs), MFCs, temperature controllers and heated furnace.

2.3.1 Planar nanowire growth

During our experimental growth we observed that we can obtain two types of growth depending on the parameters applied: two-dimensional growth (**Figure 2.4**), where nanowires are uniform, high quality, crystalline and on the surface, and three-dimensional growth (**Figure 2.5**), where nanowires are non-uniform, thick diameters and growing out of the surface. More details about the 2D growth (optimization and characterization) will be explained in more details in the upcoming subchapters. The pre-growth flow of dilute oxygen, while the temperature ramps up, plays an important role in the type of growth needed. If no pre-growth flow is turned on, then we observe that the nanowires grow three-dimensional, with diameters more than 100 nm, being non-uniform and non-crystalline. These problems can be significantly reduced by introducing a pre-growth flow of dilute oxygen. Depending on the flow rate, nanowires can still grow three-dimensional, but the quality can be improved, where nanowires are more uniform and are of higher quality. This type of growth, where nanowires grow three-dimensional or outward and overhang from the sample edge can be useful in different applications, such as field emission (method explained later on).

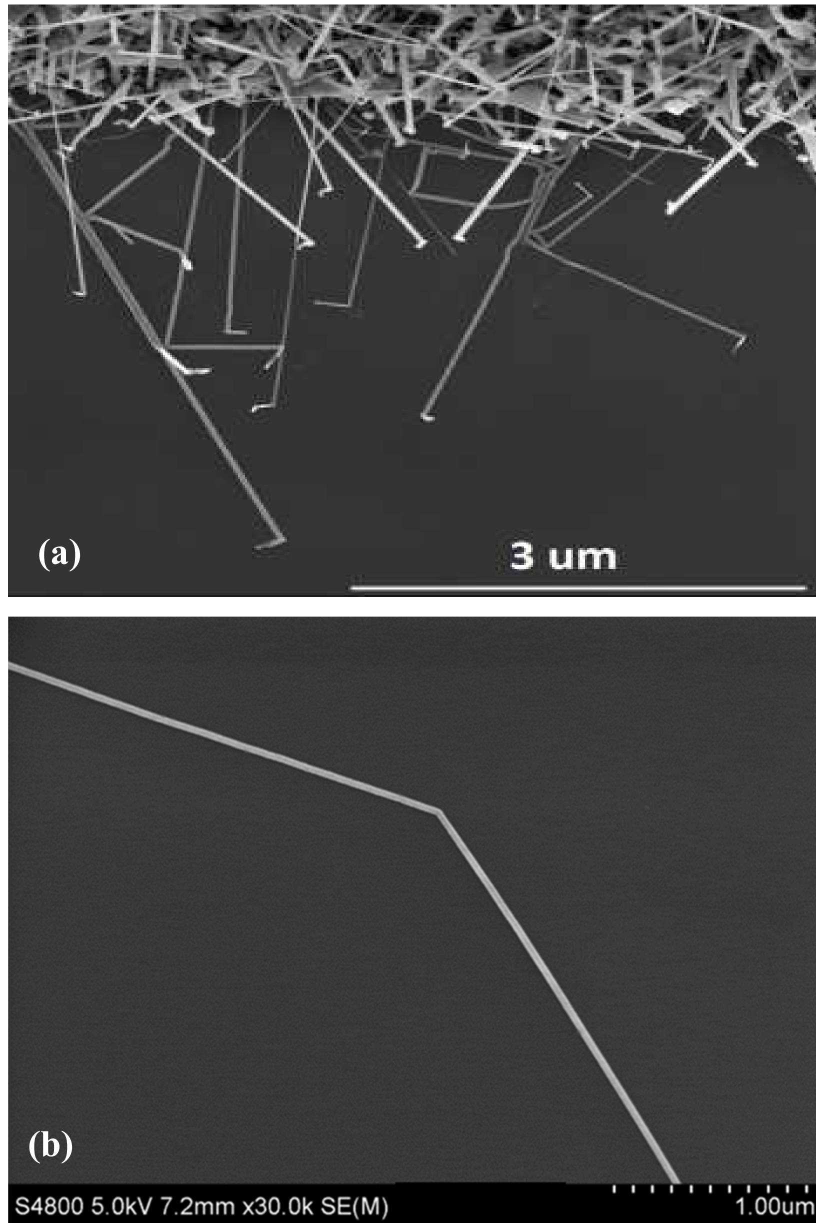

Figure 2.4 (a) SEM image of network of InN nanowires grown on Si/SiO_2 substrate. Scale bar is 3 μm. (b) SEM image of single InN nanowire grown on Si/SiO_2 substrate. Scale bar is 1 μm.

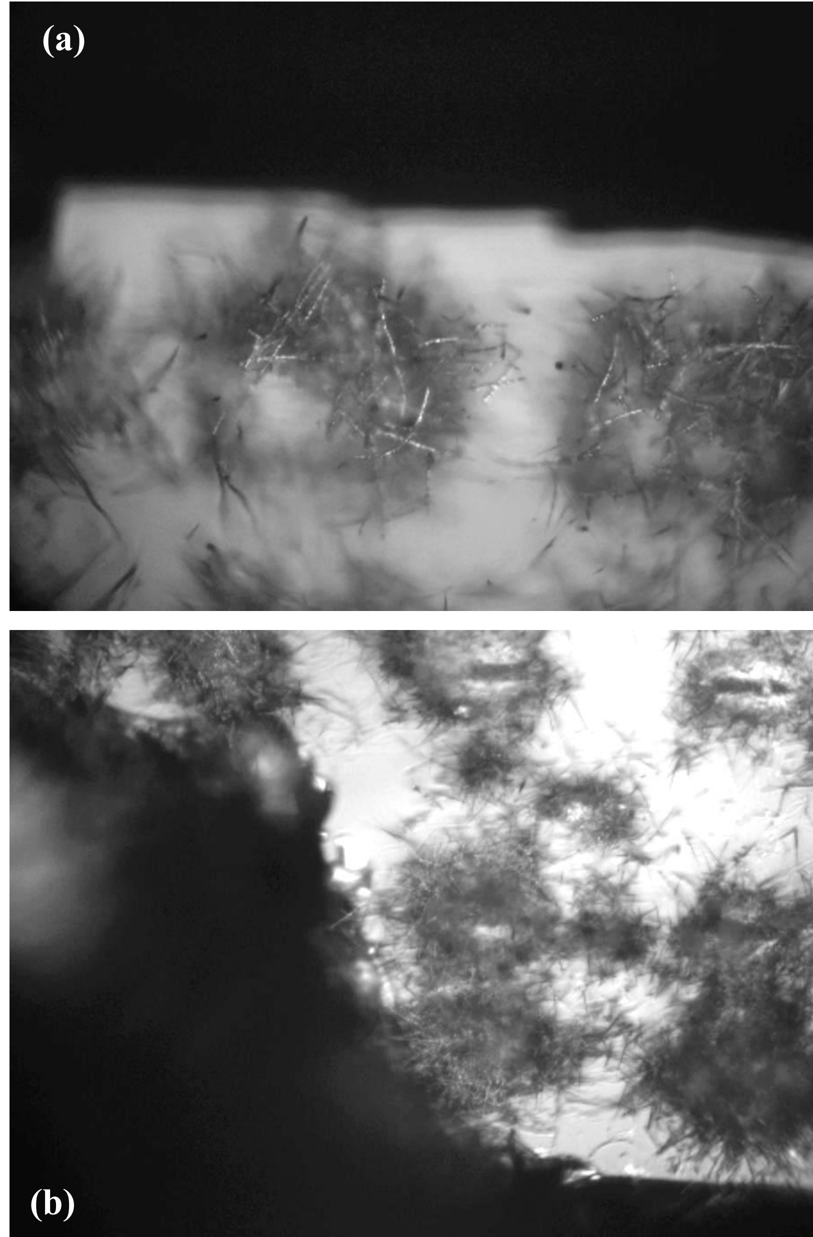

Figure 2.5 (a) and (b) show optical micrographs of dense and non-uniform 3D networks of InN nanowires grown on Si/SiO_2 substrate.

2.3.2 InN nanowire oxidation and charge accumulation at InN/In_2O_3 interface

Narrow band gap Group III-nitride semiconductors, such as InN, InAs and InSb, usually show an accumulation layer due to pinning of the Fermi level above the conduction band edge at the NW surface, while semiconducting GaN NWs show an

depletion region due to pinning of the Fermi level below the conduction band edge at the NW surface [41]. For the wurtzitic InN nanowires, polarization (polar direction [001]) is always directed perpendicularly to the NW growth direction [110], and is also perpendicular to the NW surface. Therefore, the Fermi level is pinned above the conduction band edge at the nanowire surface for InN nanowires due to the sheet charge caused by the polarizations, much like InN film. Therefore, the free electrons move to the surface and form a charge accumulation layer, combining with the accumulation charge caused by the spontaneous and piezoelectric polarizations in InN nanowires [41] [see schematic bandgap diagram of Figure 2.6 (a)]. In addition, the pinning of the surface Fermi level at the same energy for a-plane (i.e. [110]) and both polarities of c-plane (i.e. [001] and $[00\bar{1}]$) InN means that the band bending close to the surface is very similar, resulting in similar near-surface charge profiles [42]. Therefore, the accumulation is shown to be a universal feature of InN surfaces, such as wurtzite c- and a-plane InN surfaces, due to the low Γ-point conduction band minimum lying significantly below the charge neutrality level [42]. These effects result in a very high conductance of the InN nanowires, and the current is much larger than in the other Group III-Nitride device.

Surface charge accumulation model of InN nanowires would be proposed, based on theory and experimental results of surface charge accumulation of InN thin films in last subsection. Similar to InN thin films, there are also three typical forms of the InN nanowires during the growth, which can be classified as as-grown, oxidized and overgrown InN nanowires according to the changes of the chemical surface composition (i.e. oxygen). The charge accumulation layer at the surface of the as-grown InN nanowires is caused by the polarizations and pinning of the Fermi level above the

conduction band edge, resulting in the downward band bending, as shown in **Figure 2.6** (a). In general, the oxygen plays a significant role during the InN NW growth, resulting in an oxidized surface or ever overgrowing to form an In_2O_3 shell layer. The initial stage of the surface oxidation, prior to the overgrowth of a thin shell oxide layer, reduces the downward band bending [see **Figure 2.6** (b)]. The total electron density is significantly reduced and the electron distribution peak is simultaneously enforced to shift towards the InN core, resulting in increase of the carrier mobility. The improvements in the electron transport of oxidized InN nanowires relate to the saturation of the surface dangling bonds (donors), while the formation of a single crystalline In_2O_3 shell results in an extra downward band bending in InN core close to the heterointerface causing an increase of accumulation carrier concentration and the corresponding reduction of electron mobility due to the enhanced interface roughness scattering. Therefore, the maximum of the mobility of InN nanowires will be achieved at the oxidized saturation of the surface dangling bonds. For an overgrown InN/In_2O_3 heterostructure, the conduction band bending at the InN/oxide heterointerface is the same as for the oxidized InN surface caused by a variation of the polarization bound charge at the interface. Additionally, the conduction band offset at the interface results in the increase of the electron density peak as well as sheet density in comparison to the as grown InN sample, while the electron distribution peak is enforced shifted toward the InN core. The carrier density changes caused either by the oxidation or by the overgrowth can be theoretically reproduced assuming a reasonable variation of the surface band bending at the InN/In_2O_3 heterointerface, indicating that the carrier mobility of InN nanowires can be

experimentally improved by optimizing the oxidization of the surface of the InN nanowires.

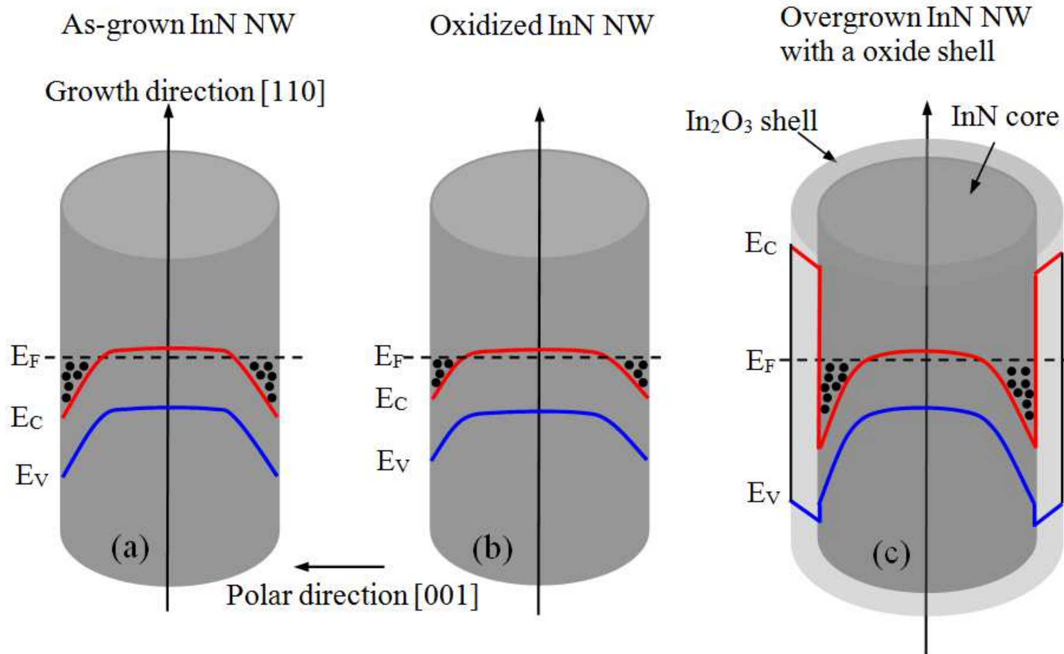

Figure 2.6 Schematic band diagrams of (a) an as-grown InN nanowire, (b) an oxidized InN nanowire and (c) an overgrown InN nanowire with an In_2O_3 shell layer.

2.4 InN nanowire characterization

2.4.1 Structural characterization: TEM

High quality single crystalline InN NWs were observed to grow along the plane of the substrate in the [110] direction with diameter and length varying in the ranges of 10-100 nm and 5-50 μm, respectively. A systematic study was performed to optimize the growth conditions and produce high quality NWs. Structural characterization of the as-grown NWs was performed with Scanning (Zeiss Ultraplus FESEM and Hitachi S-4800) and Transmission Electron Microcopy (Hitachi HF-3300 FEG-TEM/STEM with EDS) techniques. For TEM characterization, 20 and 40 nm SiO_2 membrane TEM grids (SPI

Supplies, 9 windows) were used to grow the NWs directly using 2 nm thick patterned Au catalyst spots, which allowed the NWs to be characterized readily without the need for further processing. **Figure 2.7** (a) shows an SEM image of typical NWs and their deflections from other NWs to form “K-junctions”; the inset shows magnified image of a single NW with diameter ~50 nm. It can be seen that the deflecting NW on the left side exhibited both spontaneous and barrier-induced deflections, at angles

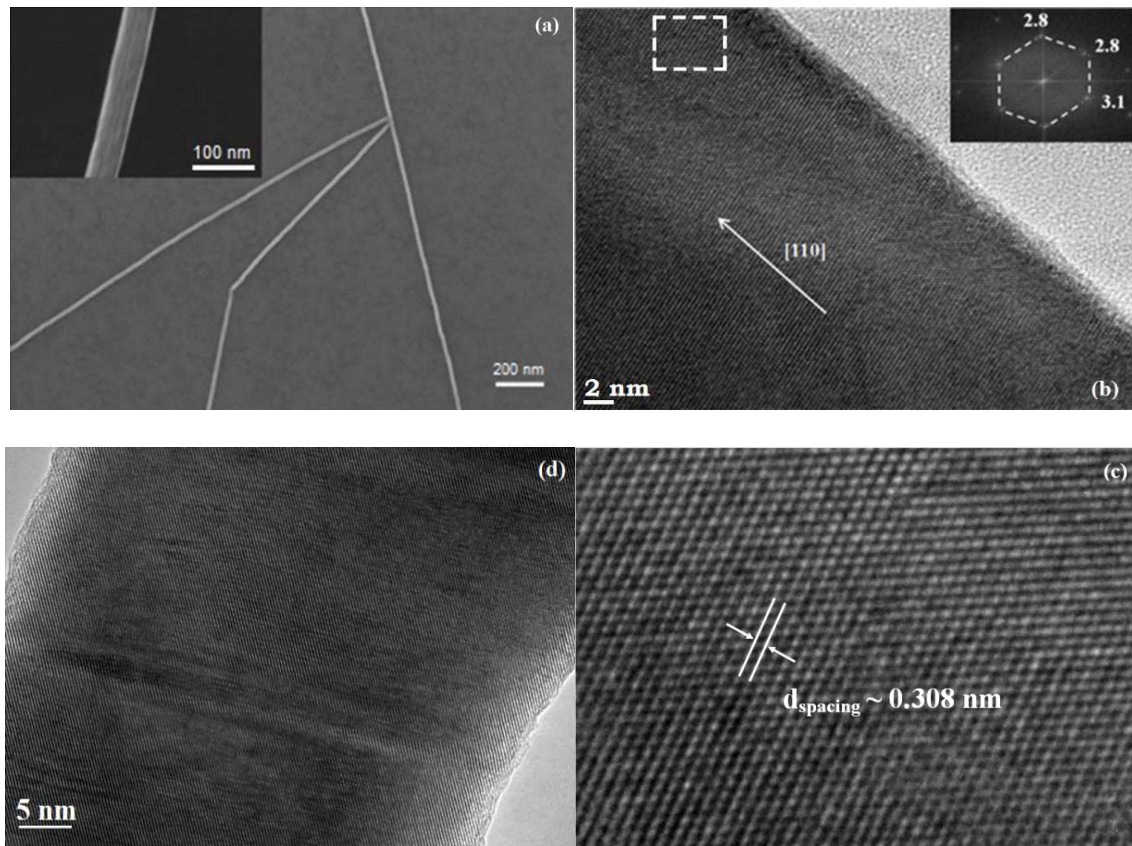

Figure 2.7 (a) A typical SEM image showing InN nanowires as-synthesized on a SiO_2 /Si substrate. The inset shows image of a single NW. Scale bar is 100 nm. (b) High resolution TEM image of a single NW growing along the [110] direction. The inset shows the hexagonal FFT spectrum. (c) Lattice resolved TEM image shows the lattice spacing. (d) TEM image of a suspended NW showing good crystalline quality and lack of any significant oxide shell layer.

that are multiples of 30°, consistent with previously reported results [22],[30]. **Figure 2.7** (b) shows a lattice resolved TEM image of a section of a NW (taken along [001] zone axis), with the inset showing hexagonal FFT spectrum, from which the wurtzite crystalline structure, the lattice spacing, and [110] growth direction of the NW can be identified. From the HRTEM image of the NW in **Figure 2.7** (b) no inclusions or outer sheath can be observed, which indicates that in spite of the presence of oxygen during growth, no shell or inclusion of In_2O_3 is formed. From the lattice resolved image shown in **Figure 2.7** (c), the lattice spacing of the (100) atomic planes is found to be ~0.308 nm, which is in agreement with earlier reports [45],[46], and very close to that of bulk InN of 0.307 nm [47]. The TEM image of a suspended NW over a SiO_2 membrane [**Figure 2.7** (d)] in a Si TEM grid clearly exhibits very good crystalline quality over the entire width of the NW and lack of any significant oxide shell layer.

2.4.2 Chemical composition: EDS

To verify the chemical composition of the NWs we performed Energy Dispersive Spectroscopy (EDS) mapping on a K-junction. Elemental mapping to confirm NW chemical composition was performed using energy dispersive X-Ray spectroscopy mode available with the Hitachi TEM system. **Figure 2.8** (a) shows the low resolution scanning TEM (STEM) image with (b), (c), and (d) demonstrating In, N and O elemental mapping, respectively. The mapping was done at In-L: 87% FWHM (3.285 keV), N-K: 30% FWHM (0.392 keV), O-K: 50% FWHM (0.525 keV) energy levels. The images are background subtracted and deconvoluted to account for close overlap between In-M peak (0.366 keV) and N-K peak (0.392 keV). However for N- and O- map the background noise was visible due to their lighter elemental weight and could not be completely

removed. Since the NWs were synthesized on thin SiO_2 membrane, a reverse contrast is observed for O-peaks i.e. along the NW the O-signal is significantly lower, while it can be detected elsewhere.

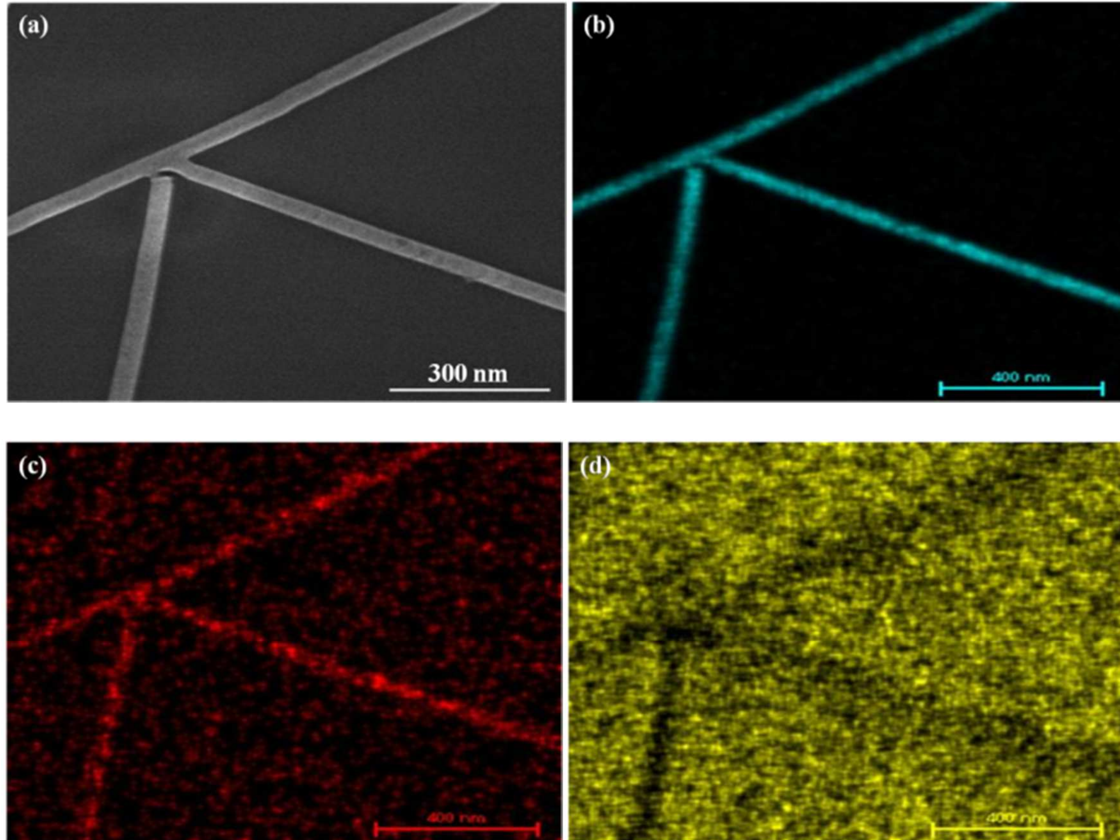

Figure 2.8 Energy Dispersive X-Ray Spectroscopy (EDS) mapping on a nanowire K-junction. (a) STEM Image of the K-junction. (b) In elemental mapping, (c) N elemental mapping and (d) O elemental mapping over the K-junction. The scale bar is 300 nm for (a) and 400 nm for (b) – (d).

To further investigate the chemical composition of these NWs, we performed EDS analysis on a fixed spot on a thin InN NW and subtracted the contribution of the SiO_2 membrane. The adjusted EDS spectra is shown in **Figure 2.9**, while the individual spectra obtained on the InN NW and the SiO_2 are shown in the top left inset of **Figure 2.9**. A TEM image of the NW and the measurement spots are shown in the top right inset

of **Figure 2.9**. To obtain the adjusted spectrum, we subtracted the EDS spectrum on the SiO_2 membrane from that obtained on the NW, after multiplying the SiO_2 spectrum with the ratio of the Si peak related photon counts, i.e. the areas under the Si peaks at 1.75 keV. We find that the adjusted spectrum shows no noticeable Si or O peak, which further supports the compositional purity of these NWs.

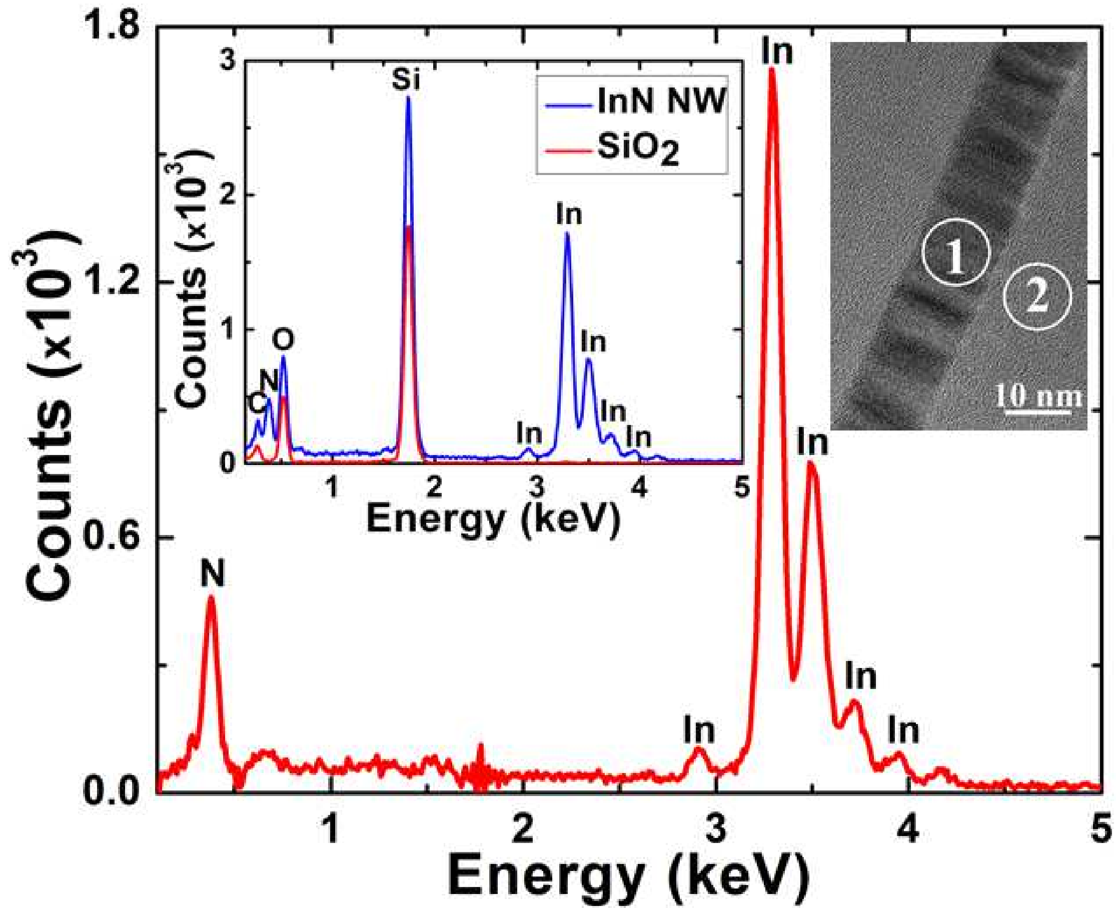

Figure 2.9 Adjusted EDS spectrum of a thin InN NW with contribution from SiO_2 membrane subtracted. Top left inset shows EDS spectra on InN NW and SiO_2 membrane. Top right inset shows TEM image with positions 1 and 2 where EDS spectra were taken.

2.4.3 Chemical composition: Raman spectroscopy

Raman spectroscopy (Horiba, LabRam 1B) was performed on InN NWs grown on 40 nm SiO_2 membrane TEM grids. Regular samples with NWs grown on SiO_2/Si substrate could not be used as Si produced a very high background signal that obscured the faint InN NW peaks. The Raman data was taken at room temperature with a micro-Raman setup, equipped with HeNe laser operating at a wavelength of 632 nm and power of 20 mW, with its focal spot tunable through an optical microscope (80×, numerical aperture 0.95) to a minimum diameter of 2 μm. A liquid nitrogen cooled charge coupled device was used to collect the scattered signal dispersed on 1800 grooves/mm grating. The backscattering Raman spectra were recorded perpendicular to the incident beam.

Raman spectroscopy was also performed to further verify the compositional purity of these NWs. As discussed above, the measurements were made on the NWs grown on the 40 nm SiO_2 membrane TEM grid to avoid interference from Si substrate. Inset of **Figure 2.15** (c) shows a section of the suspended SiO_2 membrane window, with NWs grown on it, where the Raman studies were performed. The incident laser spot for the Raman spectroscopy was focused on thicker NW (>60 nm) K-junctions to maximize the InN exposure area and hence the Raman signal intensity. From **Figure 2.10**, we can clearly see the peaks at 443, 491 and 594 cm^{-1}, which correspond to the A_1(TO), E_2 (high) and A_1(LO) phonon peaks, respectively confirming the presence of InN NWs, based on earlier reports [45],[46], [47]-[51]. The Raman spectrum indicates a broad background peak approximately between 500 and 600 cm^{-1}. This is most likely due to the activation of the B_1(high) peak, which is normally forbidden, but can be activated in presence of high electron density (>5×10^{18} cm^{-3}, which is commonly observed in our NWs[10]) [51], as

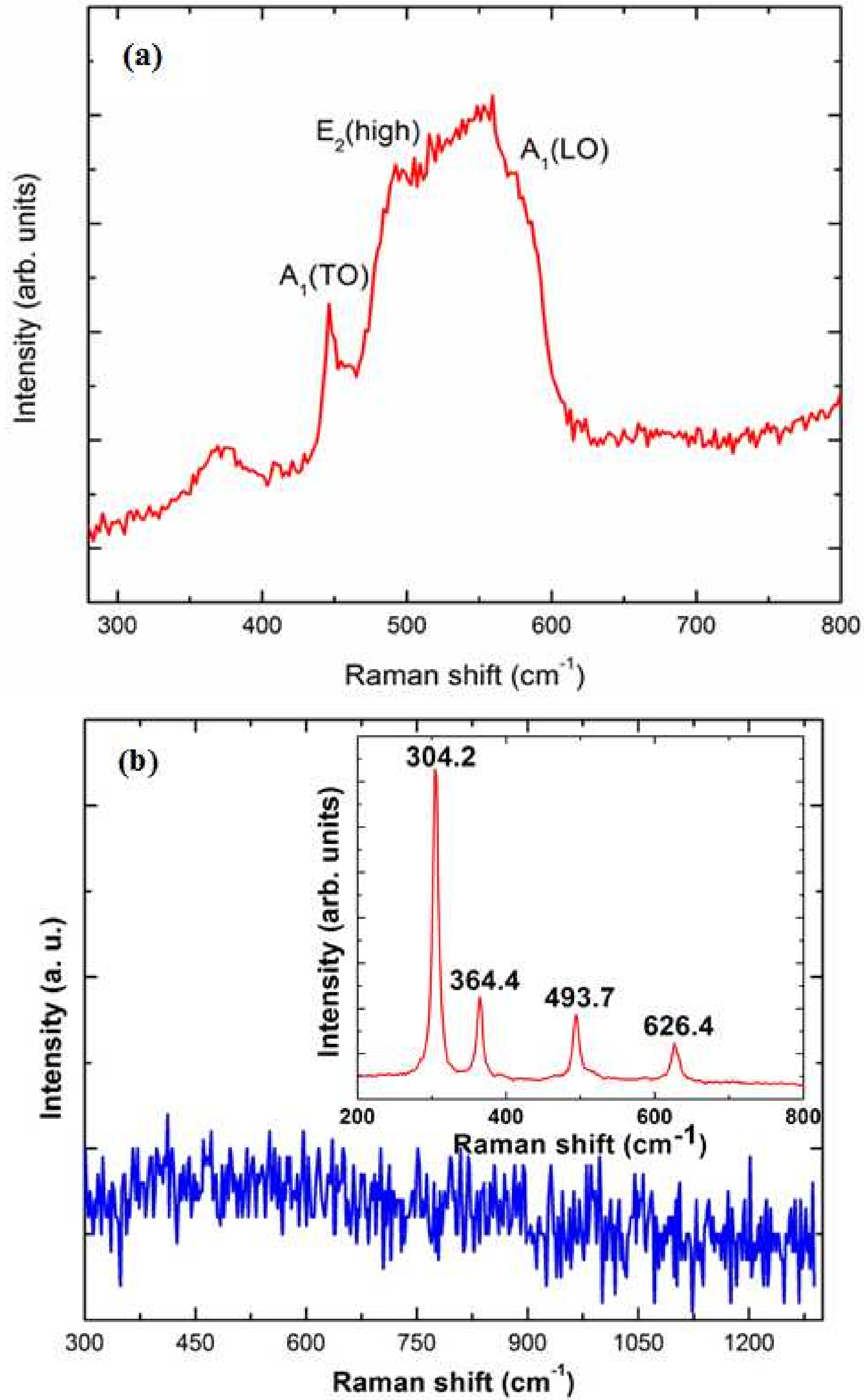

Figure 2.10 (a) Raman spectrum of the InN NW junction showing peaks at 443, 491 and 594 cm^{-1}, which correspond to the A_1(TO), E_2 (high) and A_1(LO) phonon peaks, respectively. (b) Raman spectrum of the bare SiO_2 membrane without NWs. Inset shows Raman spectra taken on commercial In_2O_3 sample.

well as activation of surface phonon modes in the 530 – 560 cm^{-1} range [50]. The A_1(TO) mode, although forbidden, has been widely observed for thin films and NWs [45], [46], [50]-[51], including nanostructures with high structural quality [45], [46], and thus can be attributed to misalignment of the crystal symmetry axis with probing axis, or internal reflection at the interfaces [51]. A broad peak with low intensity is observed between 350 – 400 cm^{-1}, was also observed in Raman spectra on highly pure InN thin films grown by molecular beam epitaxy [51], as well as high quality InN nanobelts grown by CVD [45], however, its origin has not yet been identified. For comparison, Raman spectra were taken on bare SiO_2 membrane [see **Figure 2.10** (b)], which showed no significant peaks indicating that the peaks observed in **Figure 2.10** (a) are contributed by the NWs only. The Raman spectra taken on a commercial In_2O_3 sample is shown in the inset of **Figure 2.10** (b) for comparison. The most prominent peak is observed at 304 cm^{-1}, which is not observed in the Raman spectra of our InN NWs, confirming the absence of In_2O_3 in them.

2.5 Growth optimization and the role of oxygen flow rate

Series of experiments were performed to obtain the best growth conditions including flow rates of different gases, process temperature and pressure. Among all different conditions and parameters, gas flow of diluted O_2 and temperature are the most important factors that affect the growth and quality of NWs significantly.

2.5.1 Growth temperature

One of the most critical parameter for InN growth is the temperature. In order to get high quality InN NWs we need to optimize the temperature and avoid the temperature at which ammonia cracks and the temperature at which the nanowires will decompose.

To optimize the growth temperature we performed a series of experiments by comparing the temperature between different positions of Boron Nitride sample holder, and also we performed a series of temperature profiles.

The position at which the samples are located is very important, because the temperature it is not the same throughout the quartz tube. From **Figure 2.11** we can notice that the position of the sample holder plays an important role and the temperature decreases if the sample holder is placed further away from the center of the furnace. We can also notice that the middle of the furnace reaches the maximum temperature, so choosing the location of the sample holder is critical. For our experiments the optimized location is placing the samples 28 mm away from the center of the furnace, where the temperature reaches 690 °C, the optimized value to achieve high quality InN NWs.

A temperature profile for five different segments (700 °C, 704 °C, 708 °C, 712 °C and 716 °C) was recorded and from **Figure 2.12** can be observed that the furnace temperature and the one measured are not the same, and actually the measured one is much higher than the temperature set with the temperature controller. From the figure we can also notice not only that the actual temperature is much higher than the one set, but it also overshoots, the temperature going much above the desired value, a critical step for InN NW growth. If the temperature goes above the desired value, the NWs could result in poor quality or they could also disintegrate, so knowing the actual temperature inside the furnace is very important.

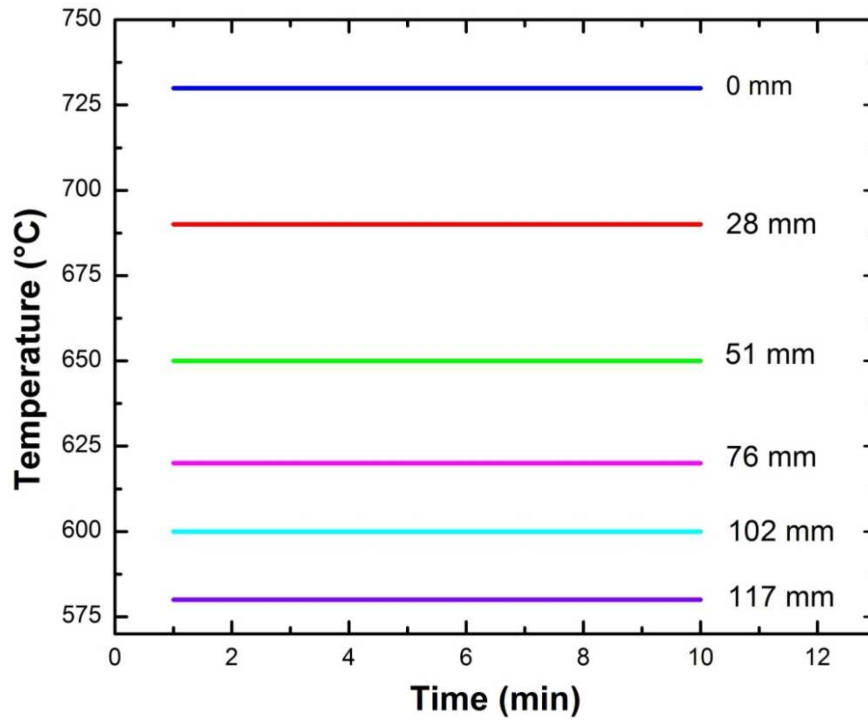

Figure 2.11 Position of Boron Nitride during growth at 0 mm, 28 mm, 51 mm, 76 mm, 102 mm and 117 mm away from the center of furnace.

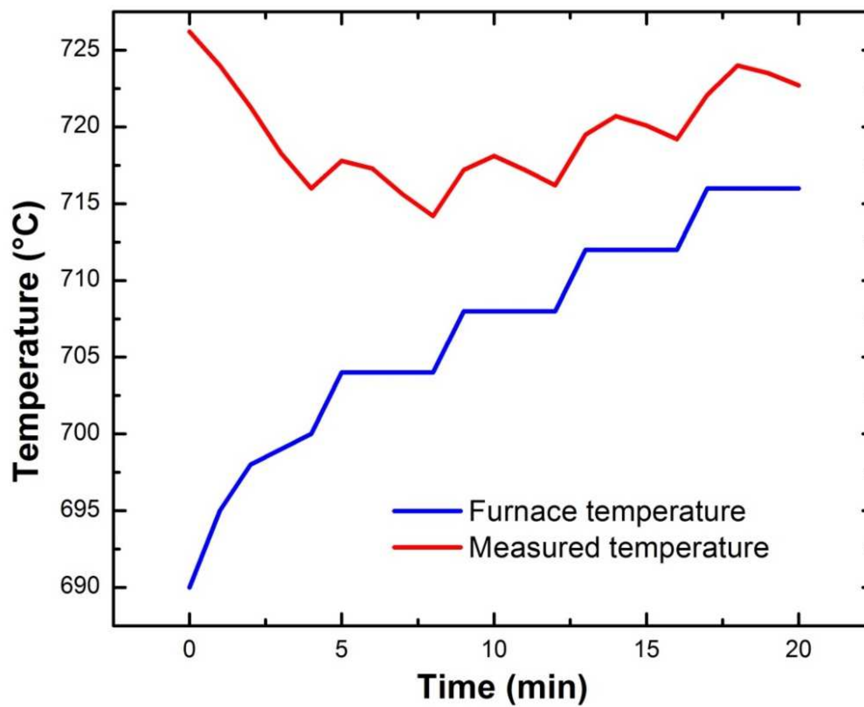

Figure 2.12 Temperature profile for 5 different segments: 700 °C, 704 °C, 708 °C, 712 °C and 716 °C.

According to previous experiments, a temperature profile is required to control the growth mechanism and the temperature should be kept constant, ~690 ºC, during nanowire growth. There are four modes of the temperature control, including ramp-up, temperature stabilization, process flow and cool down, in the temperature profile, as shown in **Figure 2.13**. Once the temperature is done ramping up and the furnace temperature controller reaches 690 ºC, a 10 minute wait period is necessary, because during this time the temperature gets stabilized and reaches a constant value. At the beginning of this 10 minute wait period it is observed that the temperature overshoots and reaches 730 ºC, a much higher value that could damage the growth quality. After the stabilization time the growth process continues as normal by introducing the required gases into the chamber. Once the growth is done, the furnace is cooled down rapidly by opening the furnace few inches and using a fan to remove the hot air.

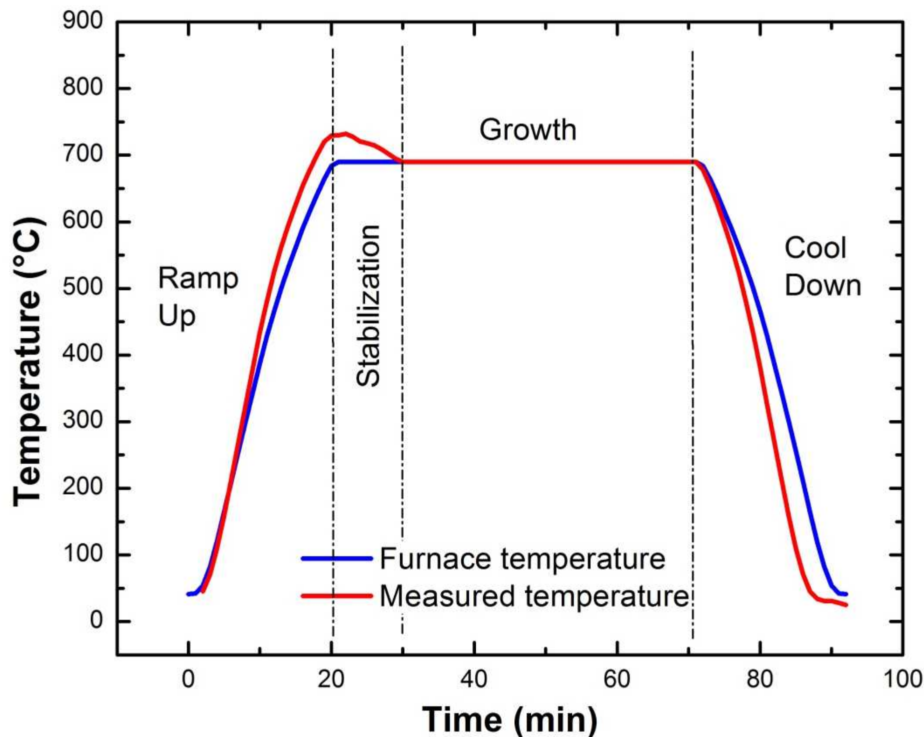

Figure 2.13 Temperature-time curve for InN NW synthesis using a CVD furnace.

2.5.2 *Effect of O_2 flow rate*

To determine the role of oxygen in the synthesis of InN NWs one needs to consider the O_2 mediated dissociation mechanism of NH_3. Depending on the reaction conditions and catalysts involved (typically Fe, Pd, Pt, Au), O_2 mediated dissociation of NH_3 can lead to the formation of atomic nitrogen (N), molecular nitrogen, NO, N_2O, and even water and hydrogen, [52]-[56]. Although, NH_3 dissociation using Pt sponge and Pd catalyst are the most common [53], [54], recently, Lopez *et al*. reported the oxidation of NH_3 on atomic oxygen (O-atom) covered Au catalyst [55]. Direct dissociation of NH_3 on O-adsorbed Au surface is much easier than on clean Au surface since the activation energy for the former is much lower than the later due to proton scavenging role of the adsorbed O-atom that drives NH_3 decomposition [56]. The reaction scheme for the dissociation of ammonia involves three major steps, activation, dehydrogenation and termination step [56]. The 1st step is the activation step where the first H-atom is stripped off and resulting product NH_2 are attached between Au atoms. In the 2nd or dehydrogenation step, a second H-atom is abstracted by a unimolecular or bimolecular reaction, and only the N-atom sits between the Au atoms. We believe that in this step the reaction happens between the In atom present in the supersaturated Au-In alloy and the stripped off N atom, which dictates the nucleation of solid phase InN in the form of NWs [44], which is similar to GaN NW growth from Ni catalyst [57]. In the last step of ammonia dissociation, unreactive N atoms formed on the Au surface are eliminated as N_2 or NO byproducts. In actual growth process, Au catalyst surface with pre-adsorbed oxygen is prepared by flowing 10 sccm diluted O_2 (3% O_2 in balance N_2) after the chamber pressure is pumped down to ~10 mTorr. The O_2 flow is continued, while the

furnace temperature is slowly ramped up to the NW growth temperature, which results in the adsorption of O atoms on the Au surface. As the eutectic temperature of the Au-In alloy is reached, the 2 nm thick Au catalyst layer forms nanoparticles which then initiates the growth of NWs as discussed above. Thus, in the entire growth process, Au uniquely serves as a two-fold catalyst, first facilitating the dissociation of NH_3, and then promoting nucleation and VLS growth of the NWs.

To better understand the influence of oxygen on NW material quality, systematic growth experiments were performed with different O_2 flow rates varying from 0 to 20 sccm with all other growth parameters remaining the same. Representative SEM images of nanowires synthesized at different oxygen concentrations (0 – 14 sccm) are shown in **Figure 2.14**. From **Figure 2.14** (a) we find that with no O_2 flow, the NW growth is very much reduced, and the few NWs that are synthesized, readily decompose leaving only traces of their outline [as marked by an arrow in **Figure 2.14** (a)]. Although the dissociation of NH_3 is not activated on clean Au surface, at high enough temperature (690 ^{o}C) NH_3 can dissociate to some extent, releasing some atomic N to initiate the nucleation and growth of InN NWs. This is, however, not enough to create high enough N over pressure to prevent dissociation of NW at that temperature. At 2 sccm of O_2, there are portions of solid and decomposed NW as can be seen in **Figure 2.14** (b). At this flow rate, the N atom concentration is somewhat higher which prevents complete dissociation of the NWs. **Figure 2.14** (c)-(f) show the SEM images of the NWs synthesized at 4, 8, 10 and 14 sccm of oxygen flow rates, respectively. With 4 sccm flow rate, localized decomposition along the length of the NW is still visible [**Figure 2.14** (c)]. However, for higher concentrations (8 – 14 sccm), no significant decomposition is observed and the

NW becomes uniform with good crystalline quality. Increased oxygen concentration ensures high N atomic concentration from high rate of decomposition of NH_3, which leads to rapid nucleation and growth of the NWs, and inhibition of InN decomposition regardless of the higher growth temperature. It was observed that higher oxygen flow rate

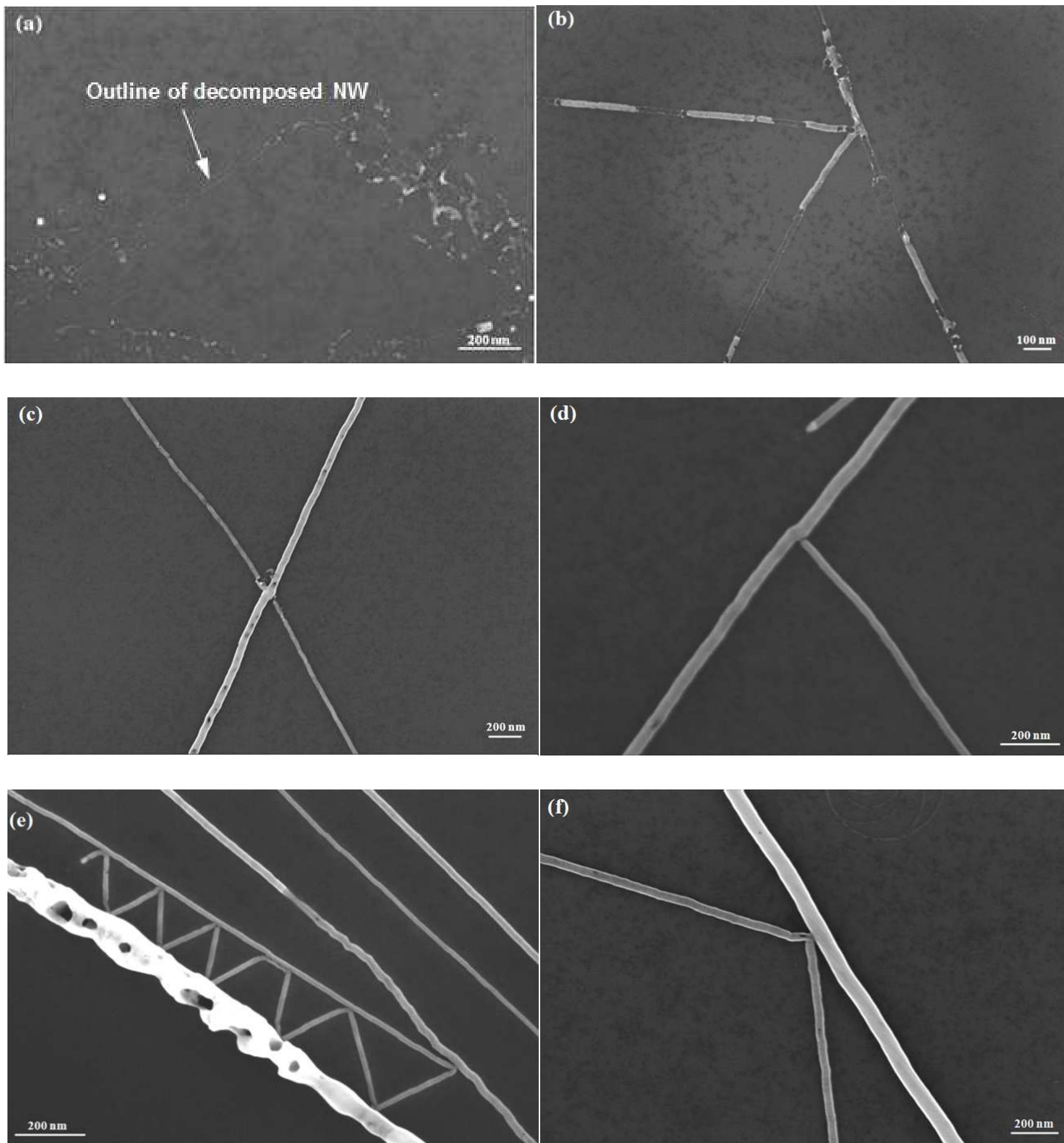

Figure 2.14 SEM images showing NW morphologies at different dilute oxygen flow rates: (a) 0 sccm, (b) 2.0 sccm, (c) 4.0 sccm, (d) 8.0 sccm, (e) 10.0 sccm and (f) 14.0 sccm.

generally resulted in better quality NWs. We performed NW synthesis utilizing up to 20 sccm of oxygen flow rates, although after 14 sccm the NW quality was not found to be significantly improved. It should be mentioned here that although high quality thin NWs (diameter <40 nm) is regularly obtained at higher O_2 flow rates (> 6 sccm), thicker NWs (diameter >60 nm) can still have significant defects and decomposition as seen in **Figure 2.14** (e).

To verify the structure and chemical composition of the NWs synthesized at different oxygen concentrations, HRTEM and EDS imaging of the NWs was performed. **Figure 2.15** (a)-(d) show the HRTEM images of the NWs for 2, 4, 10 and 14 sccm of oxygen flow rates respectively, while the insets show the FFT spectra. The lattice resolved TEM images indicate good crystalline quality of the NWs, while the FFT spectra indicate the wurtzite structure for all the oxygen flow rates. Some contrast in the TEM images can be seen, consistent with other reports [45], possibly arising out of strain in these NWs. The NWs grown at different O_2 flow rates were further investigated for chemical composition using EDS. The results are shown in **Figure 2.16** (a)-(d) and **Figure 2.17** (a)-(d) for 4 and 10 sccm of O_2 flow rates, respectively. The imaging results for both the flow rates are very similar to those corresponding to 6 sccm oxygen flow rates (see **Figure 2.8**). Like in **Figure 2.8**, the In and N peaks are clearly observed, while a reverse contrast is observed for O. Since for different oxygen concentrations only In and N elemental peaks are observed but no O peaks, we conclude that the NWs are made of pure InN, and the role of oxygen is limited to only enhancing the NH_3 dissociation and production of N-atoms.

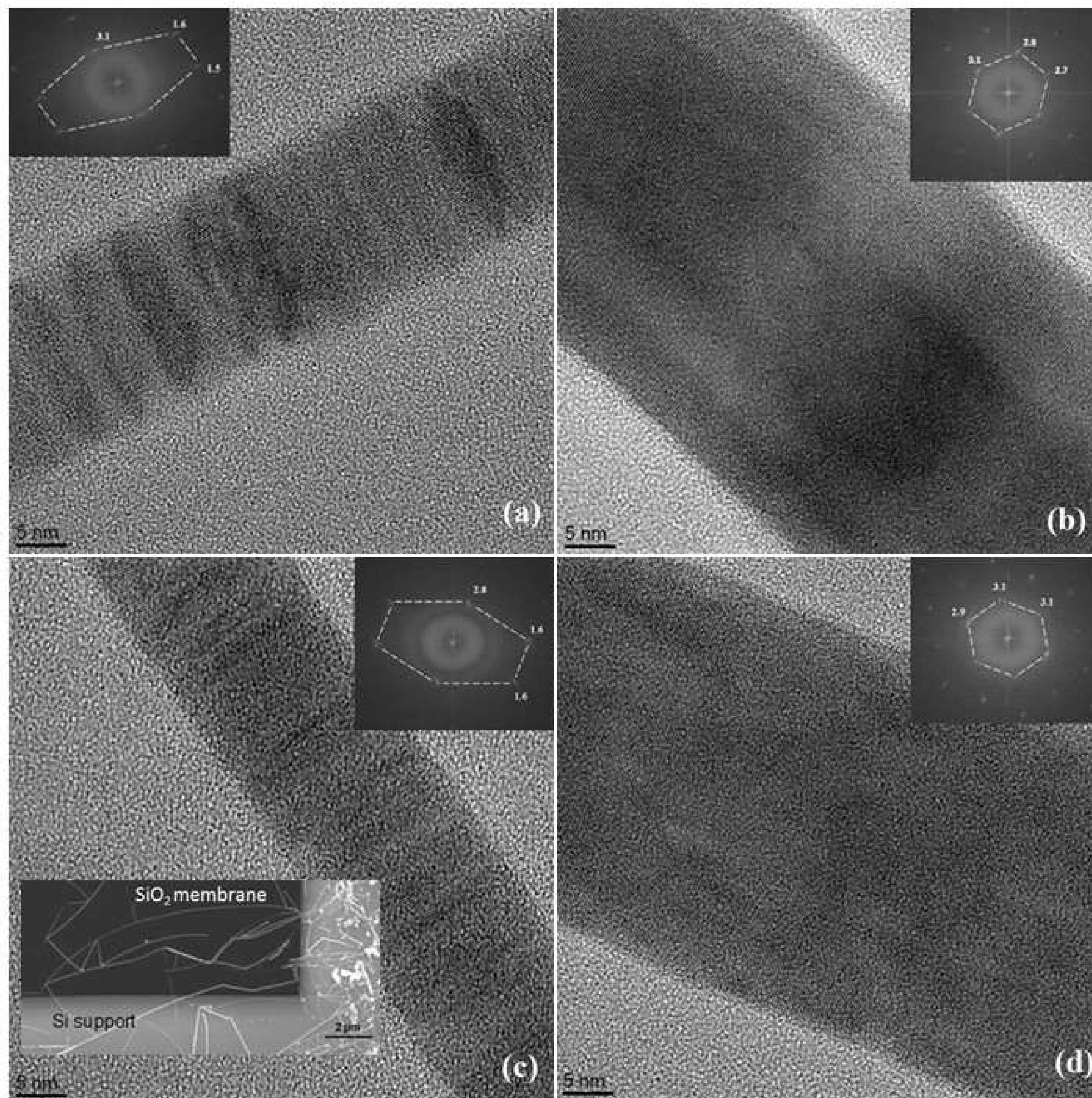

Figure 2.15 HTREM images of single NWs (on 40 nm SiO_2 membranes) grown at different oxygen (3% in balance N_2) flow rates: (a) 2 sccm; (b) 4.0 sccm; (c) 10.0 sccm; (d) 14.0 sccm. Careful observation shows lattice planes in the images. Insets in the images show the respective hexagonal FFT spectra. Bottom left inset of (c) shows a typical SiO_2 membrane window with NWs growing from catalyst spots on the Si support to the SiO_2 membrane.

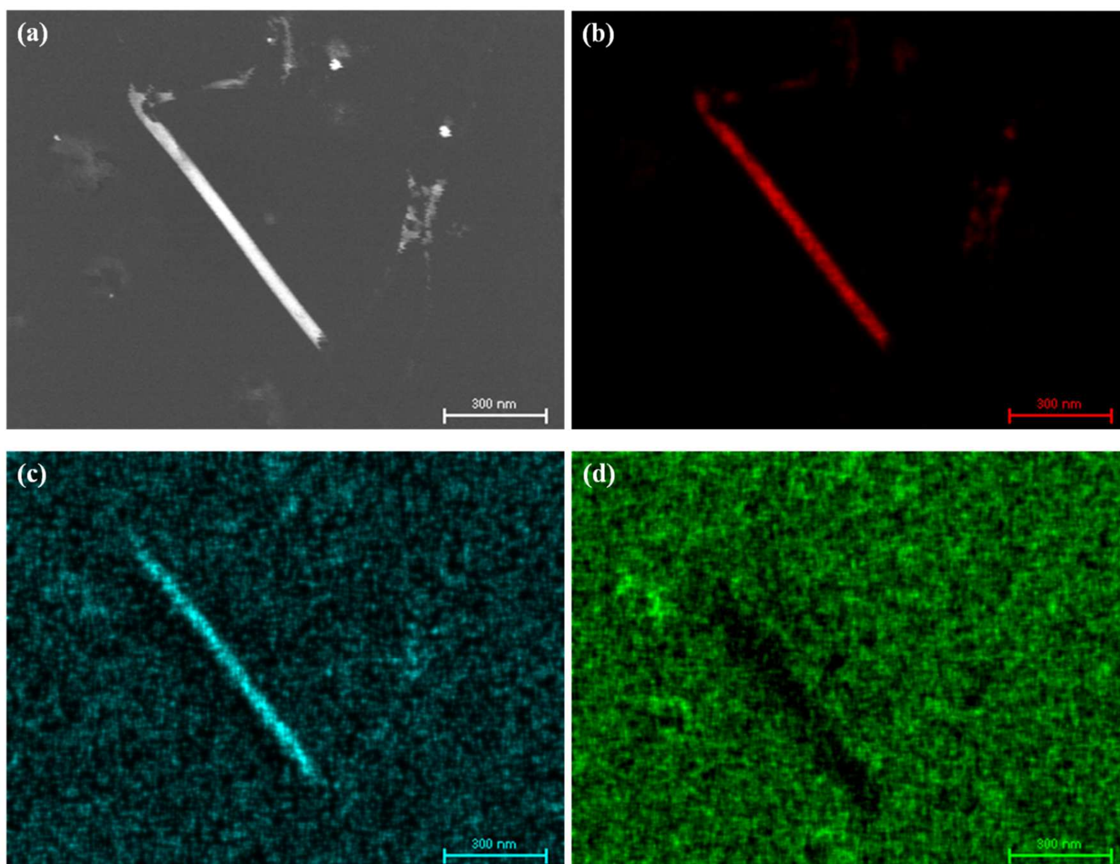

Figure 2.16 Energy Dispersive Spectroscopy (EDS) mapping on section of a partially decomposed nanowire grown with 4 sccm of oxygen flow. (a) STEM Image, (b) In elemental mapping, (c) N elemental mapping and (d) O elemental mapping along the nanowire. The scale bar is 300 nm for all sub parts.

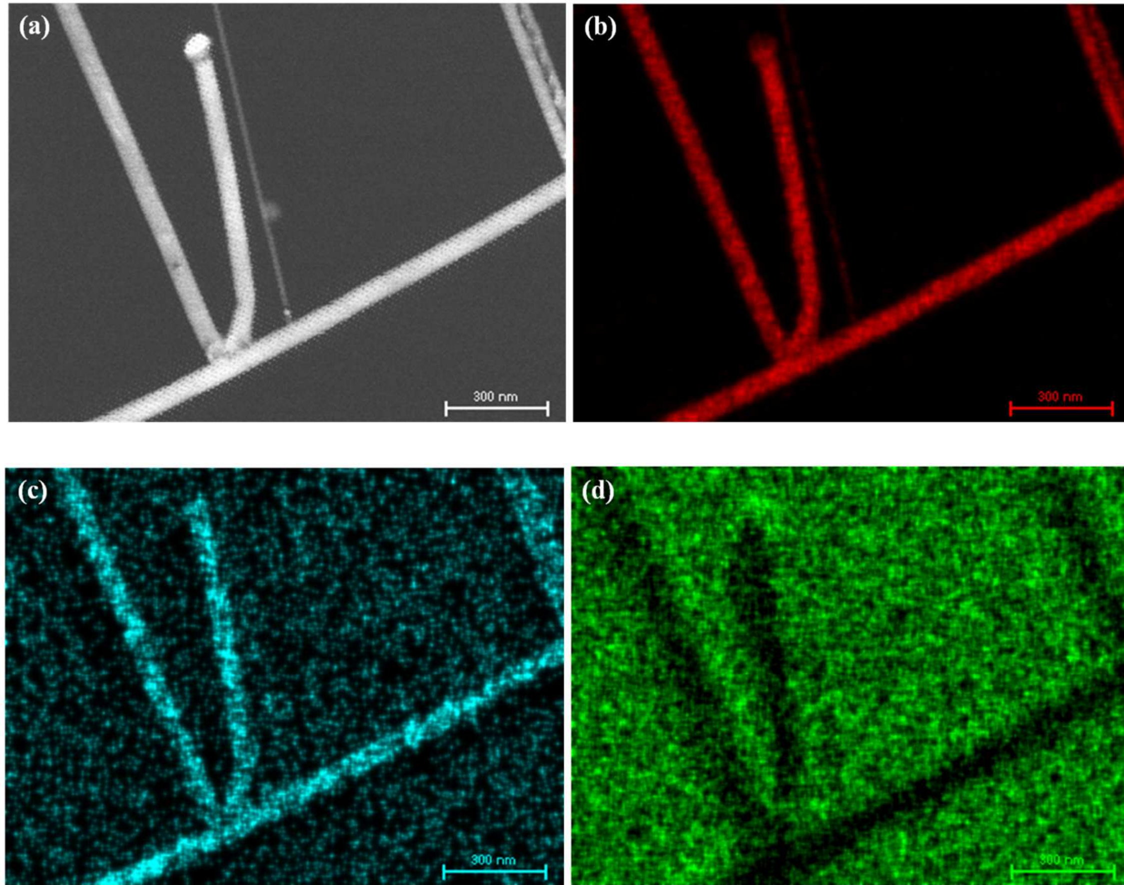

Figure 2.17 Energy Dispersive Spectroscopy (EDS) mapping around a NW K-junction. The growth was performed with an oxygen flow rate of 10 sccm. (a) STEM Image, (b) In elemental mapping, (c) N elemental mapping and (d) O elemental mapping around the K-junction. The scale bar is 300 nm for all sub parts.

2.6 Growth direction modulation

The synthesized InN NWs exhibit two distinctive properties: (i) they are almost always coplanar, especially when growing on the plane of the substrate, and (ii) they change their growth direction either spontaneously or upon meeting an obstacle in their growth path [30]. **Figure 2.18** (a) shows an example of spontaneous bending of the NW, where it bends by an angle of ~30°. Barrier-induced multiple bending of InN NWs can be seen in **Figure 2.18** (b), where the growth of the middle NW is guided by multiple

deflections from two other guiding NWs with nanoscale precision. It should be noted here that, for multiple deflections to occur, it is necessary that all three NWs be in the same plane with precise positional accuracy better than a few nanometers, and the guiding NWs should be parallel to or at a slight angle to each other. The angles of deflection of the NWs were generally found to be close to 30°, 60° or 90°.

The geometrical precision of the NW growth and deflection indicates that this is not a random behavior exhibited by the NWs, but is determined by NW material properties. The bending of the NWs at multiples of 60° can be understood from the fact that InN wurtzite crystal has hexagonal symmetry with equivalent free energy of growth along equivalent $\langle 110 \rangle$ or $\langle 1\bar{1}0 \rangle$ directions [see inset of Figure 2.18(d) for the equivalent directions]. The 30° (or 90°) bending of the NWs happens due to a change in the NW growth direction from $\langle 110 \rangle$ to $\langle 1\bar{1}0 \rangle$ direction (and vice-versa), which is possible if the free energies in these growth directions are similar.

To find out if the NWs can also be guided by lithographically patterned barriers, we deposited 100 nm thick SiO_2 barriers along with adjacent Au catalyst spot as shown in **Figure 2.18** (c). We find that an InN NW indeed deflects back and forth several times at specific angles (~90°) forming nanoscale V-shaped patterns. If catalyst pattern is deposited right at the edge of the lithographic barrier, and the growth is performed for a short enough duration, a single deflection resulting in a V-shaped structure can result. These special V-shaped structures can be readily used to make V-shaped nanocantilevers (VNCs), by etching the underlying SiO_2 layer, and could be used for a variety of applications.

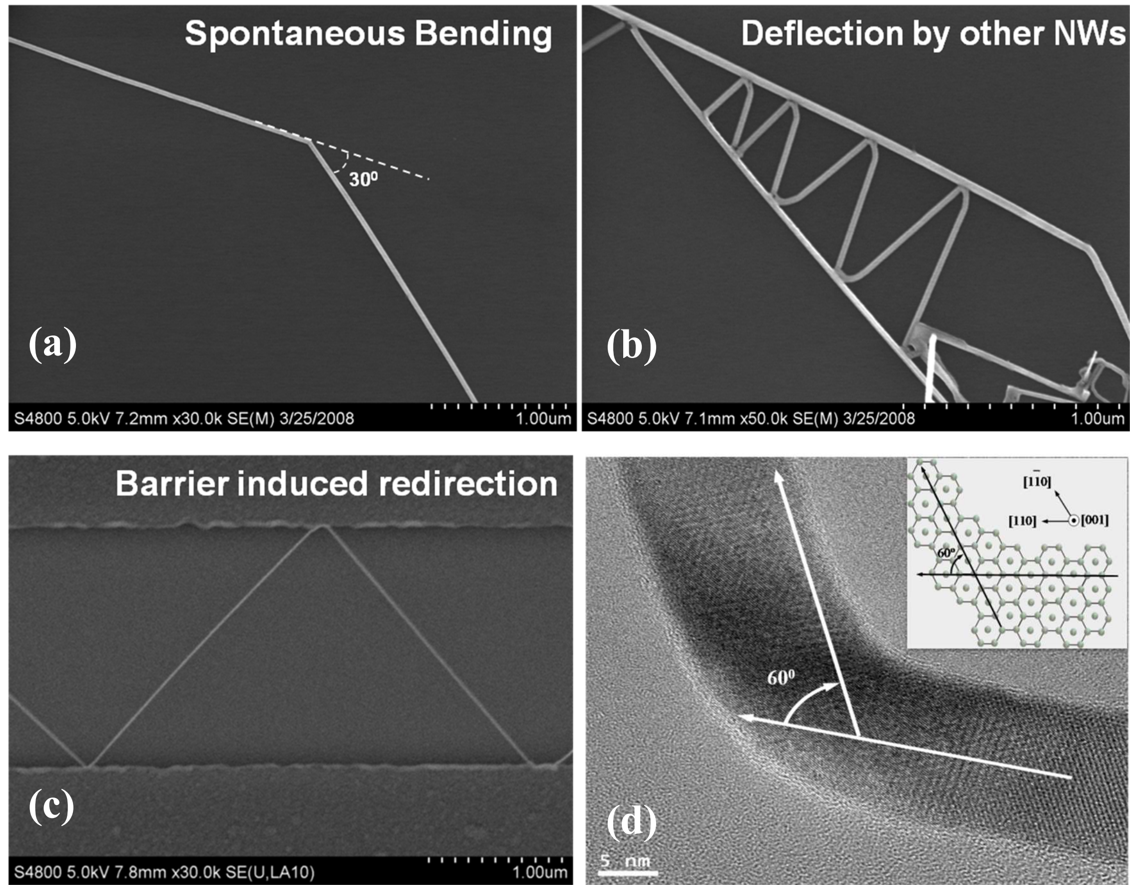

Figure 2.18 SEM images showing (a) spontaneous bending of InN NW, as well as bending caused by (b) two InN NW guides (c) lithographically deposited 100 nm SiO2 barriers and (d) Lattice resolved TEM images of a NW showing atomic arrangement as the growth direction is changed from [110] to another [1$\bar{1}$0], inset shows schematic diagram of atomic configurations for 60° (similar to 120°) bend.

CHAPTER 3

INDIUM NITRIDE NW BASED SENSORS

3.1 Introduction

One-dimensional nanostructures (1D) such as nanowires and nanotubes have been of great interest for future nanoscale building blocks and substantial promise for integrated nanoscale systems when the current silicon (Si) or other conventional semiconductor technology reaches their physical limits. To sustain the historical scaling trend beyond CMOS, novel one-dimensional structures, including carbon nanotubes (CNTs) and semiconductor nanowires (NWs), have been proposed as the active components (as well as interconnects) in future nanoscale devices and circuits. In this case, the critical device size is defined during the growth (chemical synthesis) process and can be controlled with atomic scale resolution. To date, great efforts and progress have been made in the field of CNTs, although CNT based applications are still hindered by difficulties to produce uniform, semiconducting nanotubes. On the other hand, semiconductor NWs can be prepared with reproducible electronic properties in high-yield, as required for larges cale integrated systems. Furthermore, the well-controlled NW growth process implies that materials with distinct chemical composition, structure, size and morphology can be integrated [24]. Such an ability to build specific functions into the system during growth may in turn lead to bottom-up assembly of integrated circuits [65], which offers the potential of parallel production of massive number of devices with

similar material and electrical/optical properties. Drastically different from the 'top-down' paradigm commonly used in today's semiconductor industry, this 'bottom-up' paradigm, analogous to the way that nature works, may prove to be a suitable solution to the technological challenges as devices approach atomic size.

From a fundamental physics point of view, the low dimensional nanowire structure is an ideal platform to probe properties which may be inaccessible or hard to achieve in larger devices, due to the reduced device size and ideal material properties. This is because electrons in nanowires are quantum confined laterally and thus occupy energy levels that are different from the traditional continuum of energy levels or bands found in bulk materials. The major characteristics of a nanoscale sensor are strongly influenced by the properties of the material (usually semiconductor) from which it is made. Usually, for *chem*-FET type sensing (based on surface depletion caused by adsorbed molecules) the material should have a high carrier density, high mobility, chemical inertness, and thermal stability. InN NWs, which have been investigated only in the last few years, exhibit two special properties: firstly, there is a high density of carriers present in the NW (from unintentional doping), a large fraction of which is on the surface [66]; and secondly, these NWs exhibit spontaneous and barrier induced growth redirections while otherwise growing straight on the substrate surface [67]. The first property, when combined with high mobility of these NWs, can lead to highly sensitive deflection transduction (based on surface depletion change).

3.2 Field effect transistor fabrication

A field effect transistor (FET) is a device that has a conduction channel between a source terminal and a drain terminal. A nanowire field effect transistor forms a source

region, a channel region and a drain region. The conduction in this channel region can change significantly when the nanowire is in proximity with different gas molecules. Transconductance, gate modulation, mobility, sensitivity are only few parameters that can be obtained from the measurements of a FET. To achieve such results we fabricated InN NWs FET devices using as-grown coplanar NWs on Si/SiO_2 substrate, using optical lithography for pattern fabrication and electron beam lithography for fabrication of single nanowire devices. Gold catalyst with 2 nm thickness was thermally or electron beam deposited as different patterns. The procedures for sample fabrication using optical lithography include basic wafer cleaning, resist coating, UV exposure, resist development, metal deposition and lift-off. After fabrication, the sample is introduced in the growth chamber executing the synthesis procedure explained in detail in Chapter 2. Once the nanowires are grown, sample goes for electron beam lithography procedure to achieve single/multiple NW FETs.

3.2.1 Optical lithography

Optical lithography, also known as UV lithography, is a process used in microfabrication to pattern areas of thin films or a surface of a wafer. This process uses light to transfer a geometric pattern, either from a photomask or a projection mask, to a light-sensitive photoresist. The fundamental limit of optical lithography is not determined by the optical system alone, the end result depends on the overall contribution of the optics, resist, development and etching processes.

While it is possible to use any kind of SiO_2 as the gate dielectric/barrier, we have found out that dry thermal oxide offers the best gate modulation and the lowest leakage. We used commercially grown n-doped Si wafers as our substrate. The wafers were

cleaned using industry standard RCA-1, RCA-2 and HF cleaning recipes. Then 100 nm thick dry thermal oxide was grown using Tystar Poly Furnace at 1050 °C.

The lithography process starts with cleaning the sample surface. This is a mandatory process before all other procedures, because any dirt or residues can affect the quality of the lithography process. The solvents used for cleaning the sample are acetone and isopropanol alcohol (IPA), in sequence. Acetone is a known solvent that dissolves organic residue and IPA dissolves acetone residue and some residue not soluble in acetone.

The recipe for cleaning the sample is as follows:

1) Place the sample in acetone ultrasonic bath for 5 minutes.
2) Place the sample in IPA ultrasonic bath for 5 minutes.
3) Dry the sample using nitrogen.

After the sample is cleaned, the sample is coated with photolithography resist, as shown in **Figure 3.1**. The resist used for this fabrication is S1811, a positive resist, commonly used for positive mask exposure. A baking step is used to improve the adhesion and remove any remaining solvent from the resist.

The recipe for coating the sample is as follows:

1) Spin coat the sample with S1811 positive resist at 4000 rpm for 30 sec.
2) Bake the sample at 100 °C for 1 min.

After the sample is baked it is placed under the UV light using the desired mask. The exposure time is no more than 5 seconds, followed by developing the resist from the exposed areas. The developer it is a mixture of DI water and Microposit MF-351 with 5:1 ratio. After UV exposure, metal material (in this case 2 nm Au) evaporates from the

source of thermal evaporation or electron beam (e-beam) evaporation, and covers the sample with a thin film at a pressure of ~10^{-6} Torr.

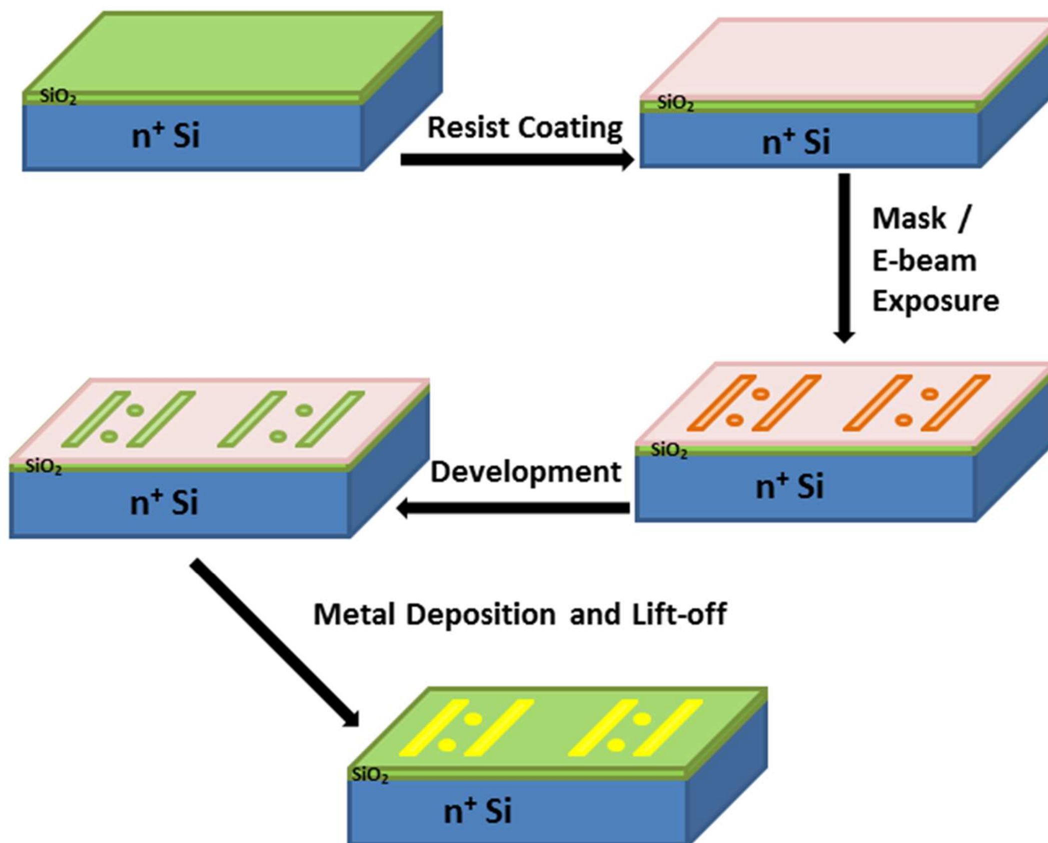

Figure 3.1 Schematic of the basis procedures of optical lithography process for catalyst patterns. The size of the lines is 3 μm x 30 μm, and the circle diameter is 3 μm.

Following the metal deposition, the excess metal film outside the exposed pattern is removed by the lift-off procedure. The sample is emerged entirely in acetone for few hours, while the excess metal film starts to peel off until it is completely lifted off. If metal takes longer to lift off, slight agitation of the beaker will help to speed the process, but the ultrasonication should be avoided, as it could remove the metal deposited in the wanted areas as well. The patterned metal thin film is left after the lift-off procedure, as shown in **Figure 3.2**.

Figure 3.2 Optical images of 2 nm Au pattern. (a) Size of lines is 3 μm x 30 μm and the diameter of the circles is 3 μm. (b) The size of the patter is 50 μm x 50 μm.

Following the lift-off procedure, InN nanowires were grown in the horizontal furnace through direct reaction between metallic In and NH_3. The growth steps are explained in Chapter 2, section 2.3. Once the growth is completed (**Figure 3.3**) the sample will undergo several steps using e-beam lithography to achieve single InN NW FET.

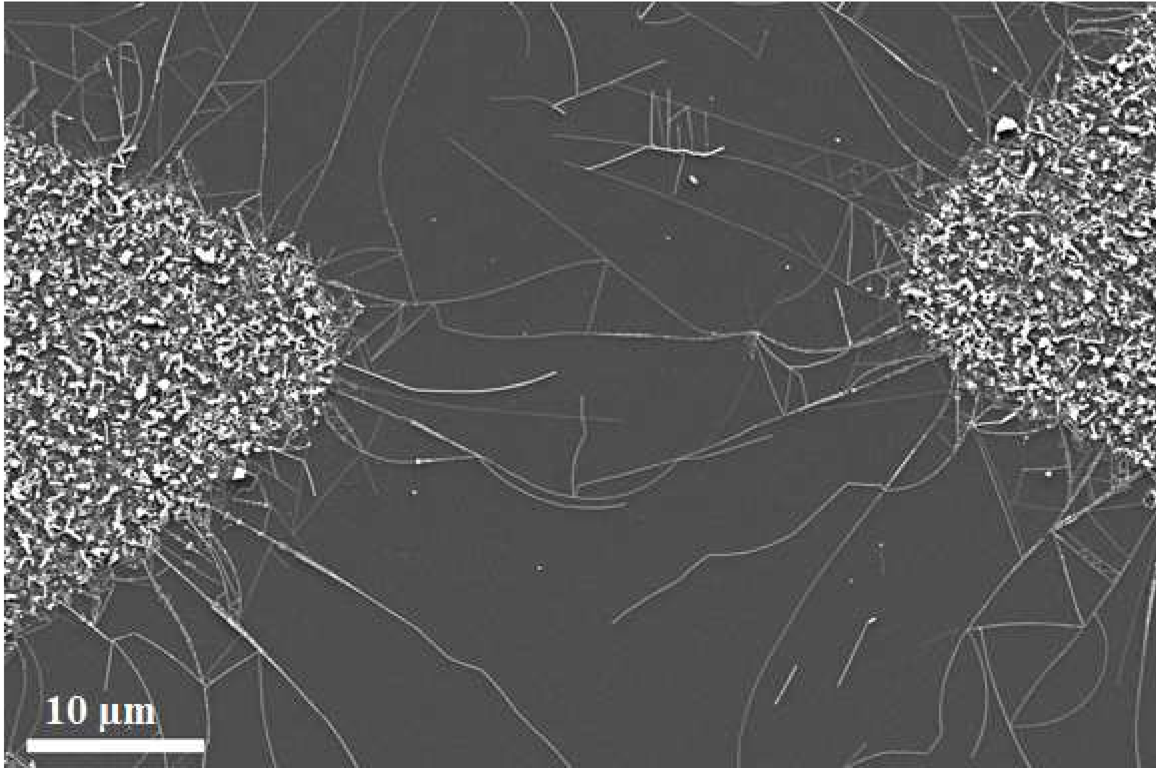

Figure 3.3 SEM image for a network of NW. Scale bar is 10 μm.

3.2.2 Electron beam lithography

Electron beam lithography (usually spelled e-beam lithography) is a procedure that draws a custom pattern by scanning a beam of electrons across the sample surface covered with a resist (PMMA) thin film, and of selectively removing either exposed or non-exposed regions of the resist by developing. E-beam lithography has the ability to create nanoscale structures in the resist that can subsequently be used for the nanoscale electronic devices (sub 10 nm resolution).

Before starting the lithography process, the sample is cleaned using the steps presented in Chapter 3, section 3.2.1. After cleaning, the sample is coated with an e-beam sensitive material. One of the most commonly used resists for high resolution work is

polymethyl methacrylate (PMMA). PMMA is typically used as the imaging resist for lift-off process.

The recipe for coating the sample with PMMA is as follows:

1) Spin coat the sample using PMMA 495k at 6000 rpm for 40 sec
2) Bake the sample at 180 °C for 2 min
3) Spin coat the sample using PMMA 950K at 6000 rpm for 40 sec
4) Bake the sample at 180 °C for 2 min

PMMA 495k is more sensitive to light and it is used as the first layer because it causes an undercut in the resist. The baking step after each coating layer is used to improve adhesion and remove solvent from the PMMA. After coating the sample with the two layers of PMMA and baking, the thin film of resist is ready for exposure.

The brief procedures of e-beam lithography are described as follows:

1) Before e-beam exposure, get coordinates of the grown InN NW pattern using PAINT software.
2) Design the contact pads using DesignCad software.
3) Focus on the sample (not on the resist, otherwise the writing will not give results) by making focusing spots at $6x10^{-11}$ A current.
4) Align the sample using the existing patterns by using x and y coordinates and rotation as well.
5) Set SEM parameters such as measured specimen current, magnification and writing dose.
6) Write the designed pattern on the PMMA in SEM.
7) Develop the exposed sample using the recipe explained below:

a. Immerse sample into 1:3 MIBK:IPA development solution (Methyl Isobutyl Ketone:Isopropyl Alcohol) at 23 °C for 40 seconds.
b. Immerse sample in IPA and shake the sample for 35 seconds
c. Dry the sample using nitrogen.

The last step, after e-beam exposure and PMMA development, is to deposit metal in the opened spaces. Contact pads were deposited by electron-beam (e-beam) lithography technique using four layer metal stack Ti/Al/Ti/Au (20/50/20/50 nm) (**Figure 3.4**). The e-beam lithography process offers the ability to create custom patterns in desired locations, unlike photolithography, which is important for realizing discrete sensor devices.

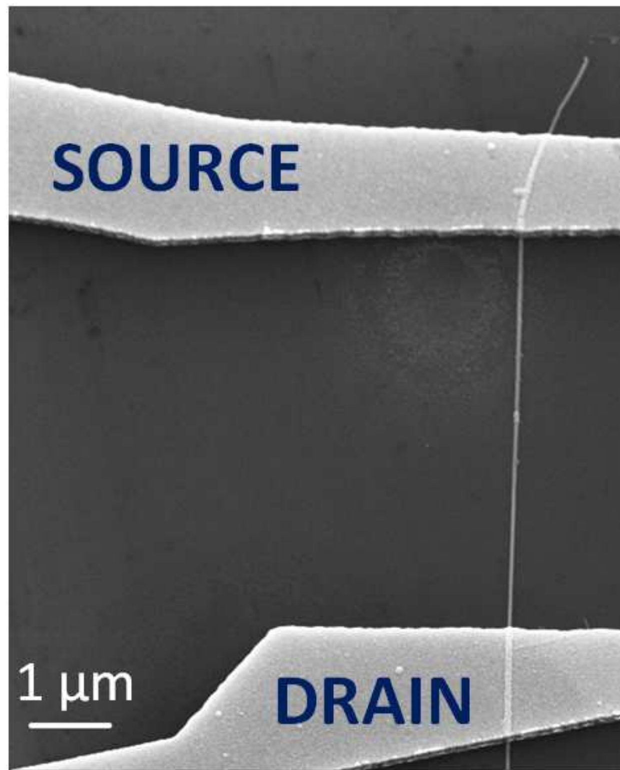

Figure 3.4 SEM image of InN NW FET with source and drain contact deposited on each side of the nanowire.

3.3 Electrical characterization

For electrical characterization both Agilent B2902 and Keithley 2612A source measuring units (SMUs) were used. Samples were mounted on a metal disc using silver paint and the characterization was performed using a probe station. The sample and metal disc were mounted on the stage using a vacuum chalk.

3.3.1 Current-Voltage measurements

Figure 3.5 (a) and (b), respectively show the I_d-V_d and I_d-V_g characteristics of the multiple InN NWs device, measured in air at room temperature. I_d-V_d curve show great gate control, excellent drain current modulation and device complete shutdown for gate voltage of -15 V. The I_d-V_d curves are linear and for a drain voltage of 1 V, and we notice a change in drain current of 1.8 μA for ~ -15 V gate bias. The drain current decreases for negative bias voltages, which indicates that the carriers in the NWs are n-type (electrons). **Figure 3.5** (b) represents the I_d-V_g curves and shows a threshold voltage of -15 V and maximum transconductance dI_d/dV_g as ~ -0.12 μA/V under the measurement conditions of $V_d = 1$ V.

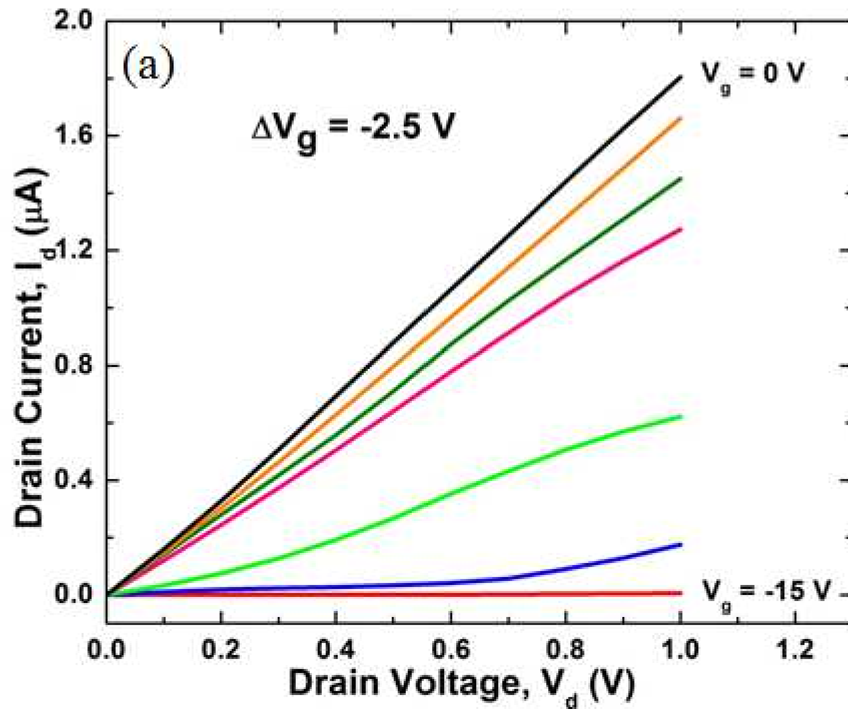

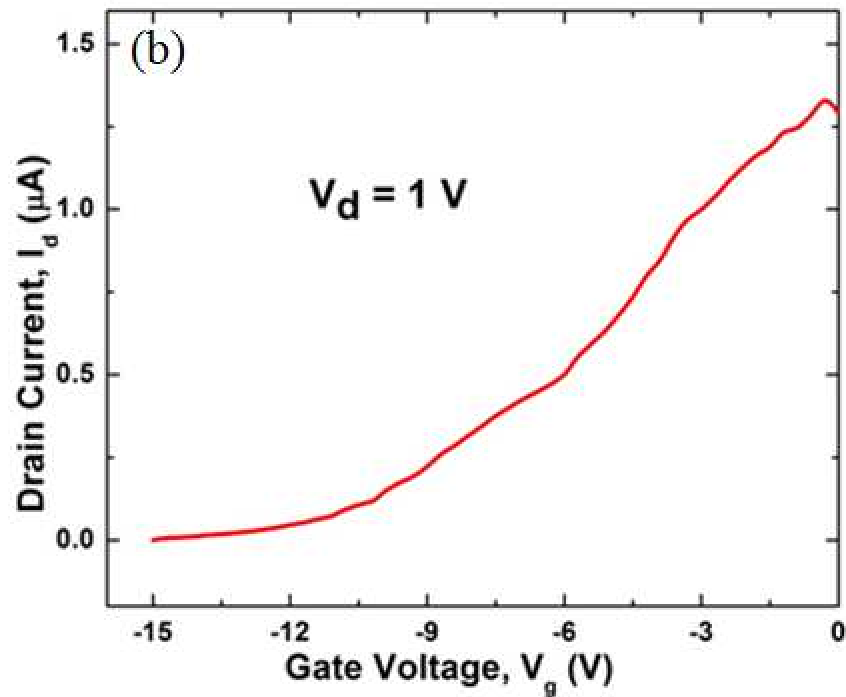

Figure 3.5 (a) I_dV_d curves for InN NW FET at gate bias voltages varying from 0 to -15 V with intervals of -2.5 V and (b) I_dV_g curve measured at Vd = 1 V.

For this device, there was an average of 3 NWs between the source and drain with average length of 10 μm, average diameter of 20 nm. Using the formulation for an FET with multiple conducting NWs [22]

$$\frac{dI_d}{dV_g} = \mu_e\left(\sum_{i=1}^{n} \frac{C_i}{L_i^2}\right)V_d \quad (1)$$

where L_i and C_i are length and capacitance for the *i*th NW in the FET and V_d is the drain voltage bias, and the capacitance given by [22]

$$C_i = \frac{2\pi\varepsilon_{eff}\varepsilon_0 L_i}{\ln\left(\frac{2h}{r_{nw,i}}\right)} \quad (2)$$

where h is the oxide layer thickness, $r_{nw,I}$ is the radius of the *i*th NW and ε_{eff} is the effective dielectric constant, we can obtain an average mobility of 267 cm^2/Vs, which is very good for InN NWs.

3.3.2 Field emission

Highly sensitive detection of analytes is possible but their unique identification can be a challenge. It has been shown that selective gas detection is possible, based on different threshold voltages for current turn-on, using various nanostructures such as, whiskered gold nanowires (Au NWs) [63] and carbon nanotubes (CNT) [64].

To determine the suitability of InN NWs for gaseous detection based on tunneling current and unique identification of analytes from the threshold voltages, we investigated field emission using the InN NWs. For this purpose, the NWs were made to grow outward, and overhang from the sample edge as shown in **Figure 3.6**. These NWs were then used for tunnel device measurements.

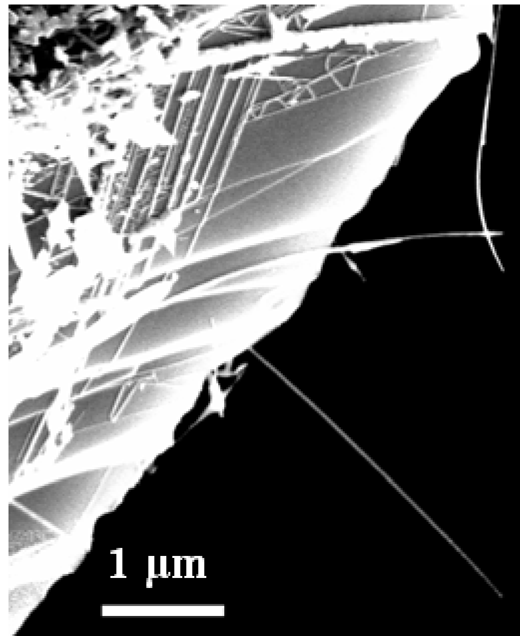

Figure 3.6 SEM image of NW overhang from the edge of the sample.

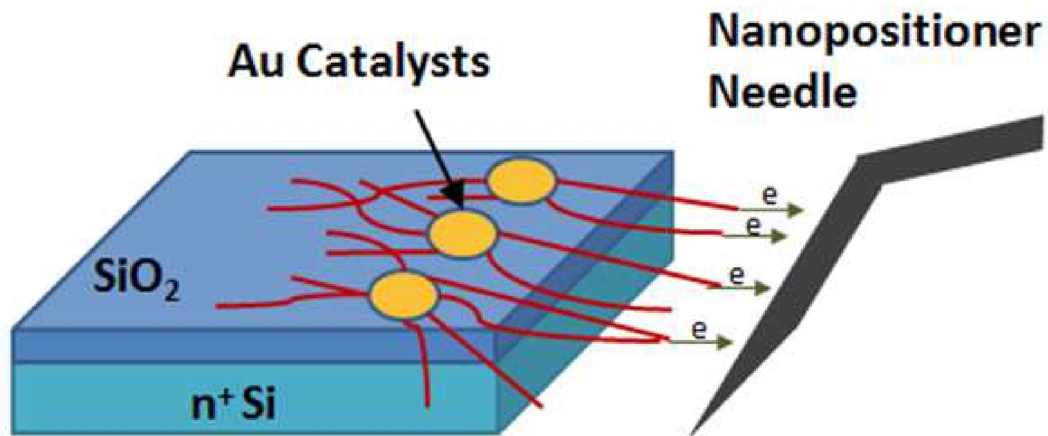

Figure 3.7 Schematic of experimental set up for the field emission studies from the InN NWs.

A schematic diagram of the tunneling measurement setup is shown in **Figure 3.7** and hanging NWs grown from Au catalysts are observed. From the diagram we can see that NWs grow along the surface, but at the end of the sample, NW continue growing

resulting in hanging NWs, and sometimes the nano-network mentioned earlier, it forms also while hanging. The needle approaches the NWs by a nanopositioner that is controlled by computer software.

In case of Au NWs reported by Sadeghian *et al* various threshold voltages for field emission is observed for various analyte gases, which can be used to identify them [63]. Unfortunately, the threshold voltages are rather broad, and not very suitable for discerning gases with closely spaced threshold voltages. Our InN NWs with very high carrier density (>10^{19} cm^{-3}), and narrow diameter (even < 10 nm) is uniquely suitable for gaseous detection based on the field emission method, with very specific and narrow turn-on voltage expected for InN NWs. Specifically, these NWs would offer: (i) much lower electric field (and hence applied voltage) for turn-on due to narrow diameter and very low resistance (due to high carrier density and high mobility), (ii) extremely high sensitivity possible since, unlike the FET type sensor where the current change is linear, the tunneling current depends exponentially on the change in surface work function (SWF) on InN.

The experimental results for the field emission studies are shown in **Figure 3.8**, where we performed preliminary testing with InN NWs to determine their tunneling behavior. **Figure 3.8** shows I-V curve of two different sized InN NWs with plate distance of ~1 μm for the longer one. The distance was controlled using a Au-coated tungsten needle attached to a nanopositioner. Initially, the needle was made to touch the sample, and then it was slowly moved away, until the current reduced to zero. The voltage bias was then slowly increased and the I-V characteristics were recorded, and shown in **Figure 3.8**. We find that there is a sharp change in NW current when voltage supplied

increased to ~2 V. With further increase in voltage to ~3.5 V, we can see that the current increased again, with the other NW is contributing to the tunneling current. The inset shows similar I-V characteristics for a single NW. It is noteworthy that the tunneling threshold voltage is almost same in both cases at ~2 V [which is expected, since the gaseous medium was same in both cases (air)].

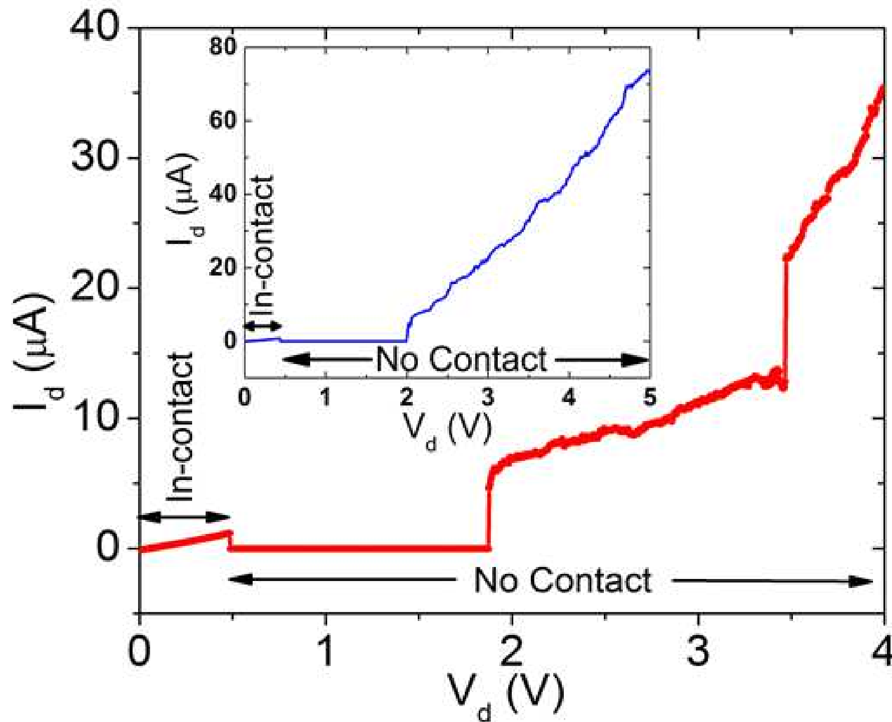

Figure 3.8 I-V curve showing field emission of InN NWs starting at different voltages. The inset shows the field emission for a single InN NW.

3.4 Sensing results

Figure 3.9 shows a schematic diagram of experimental setup of single InN NW FETs and multiple InN NW FETs measurements. The devices were evaluated in a sealed chamber with electrical feed through and gas inlet/outlet. Sensing experiments were carried on by purging and degassing a series of gases (air, pure N_2, and NO_2 diluted in

N_2 in different concentrations) at room temperature. Drain and gate electrodes were biased by Agilent E3649A Dual O/P DC power supply and the sensing was collected by Agilent 34970A Data Acquisition/ Switch unit. The I_d-V_d data was collected by Keithley source measurement unit (SMU) 2612.

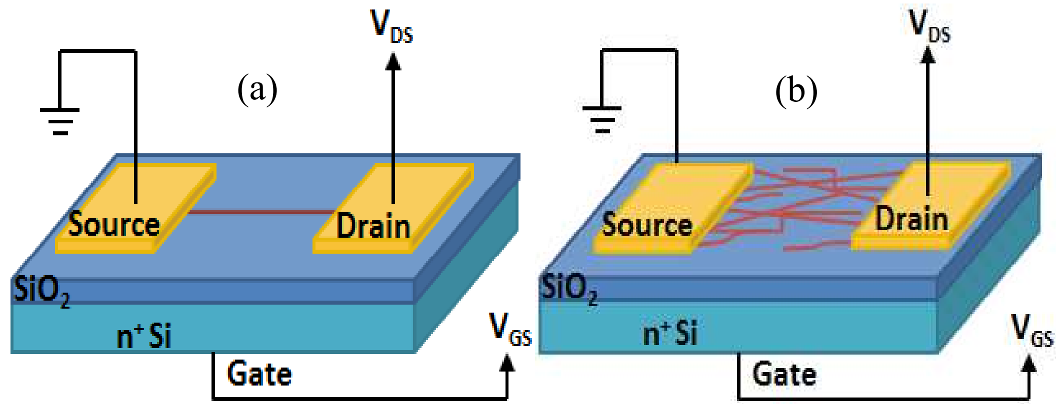

Figure 3.9 Schematic diagram of (a) single InN NW FET and (b) multiple InN NW FET.

Figure 3.10 shows a picture of the gas sensing setup. From the image it can be seen that the sample is mounted on a metal disc using silver paint, which is then held in place tightly using a regular vacuum chuck. The two probes serve as the source and drain contacts and are connected directly to the SMU. The micropositioner probes are on the source, drain and the metal disc (back gate contact), and positioned using a microscope with 20x lens. The gas flowing was obtained by using a Teflon tube and a mass flow controller connected directly to MKS type 247 channel readout.

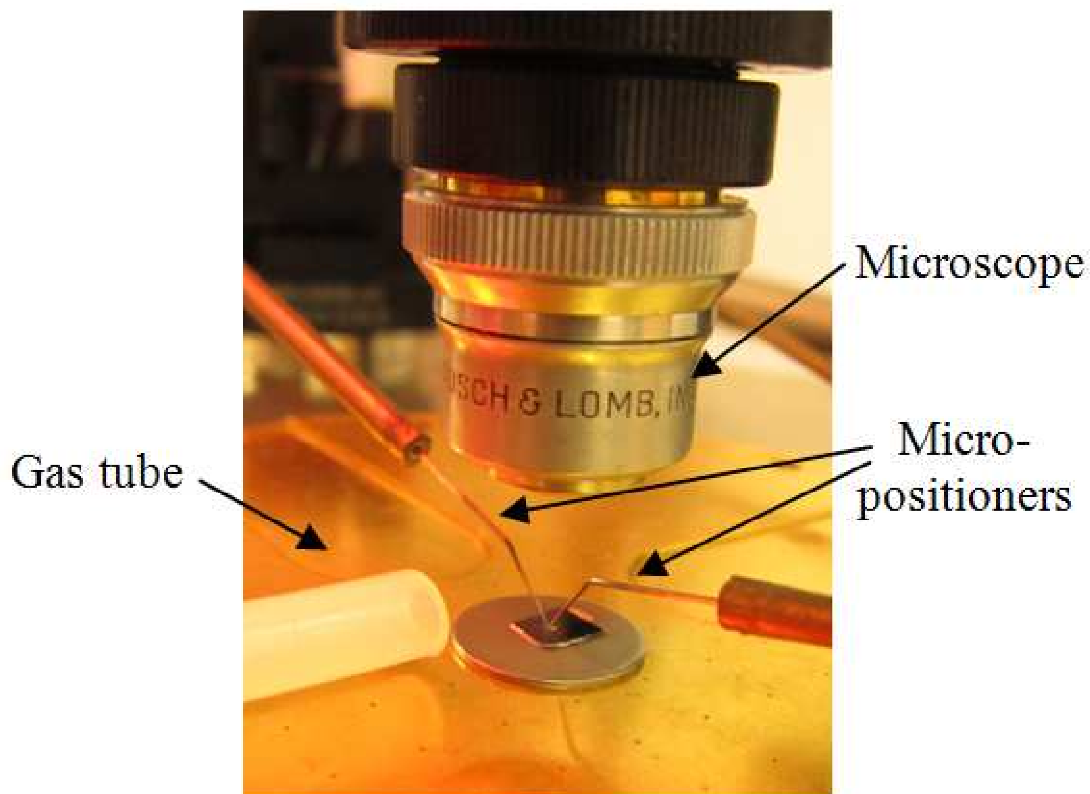

Figure 3.10 Picture of sensing setup showing the device under test (DUT) and the gas flow line.

Using these NW FETs we obtained preliminary sensing results with dilute acetone (saturated vapor diluted 10 times with N_2), and the results are shown in **Figure 3.11** (a). Very good sensing response was also observed as the FET was exposed to diluted water vapor shown in **Figure 3.11** (b), and NO_2 at various concentrations (down to 45 ppb, data not presented) [62].The sensing experiments with acetone and water vapor were performed by passing dry nitrogen through bottles filled with acetone and water and then diluting appropriately to obtain desired concentration of the vapors. In both graphs of **Figure 3.11**, we can notice that when the vapors are turned on, a sudden decrease in current is observed, which is repeatable for each time the on-off switch was applied.

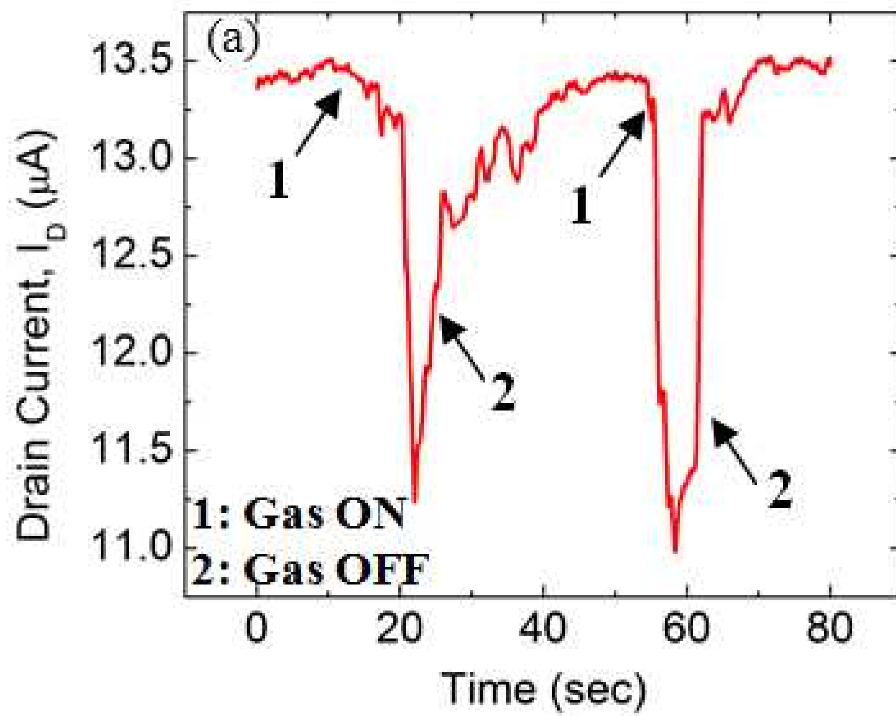

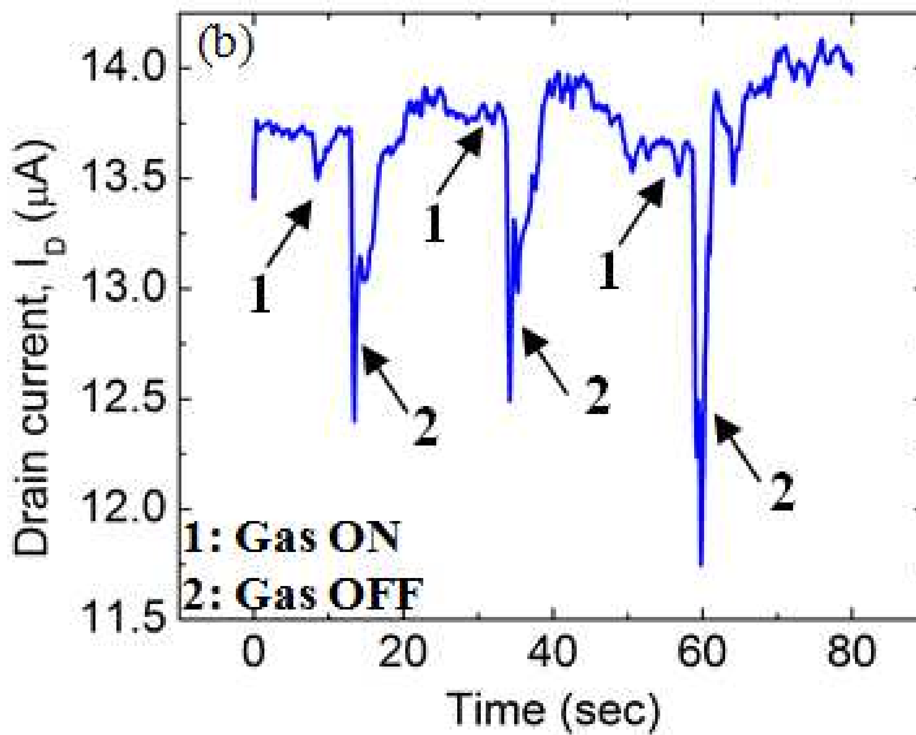

Figure 3.11 Sensing results using InN NW FET with (a) acetone vapor and (b) water vapor.

CHAPTER 4

InN NEMS Based Sensors

4.1 Introduction

One of the most recent significant applications based on nanowire in the last few years is the nanoelectromechanical devices. Nanoelectromechanical systems (NEMS) are devices that integrate electrical and mechanical functionality at nanoscale level. NEMS are the next miniaturization step from the microelectromechanical system (MEMS) [69]. An example of a silicon nanowire based nanoelectromechanical device is shown in

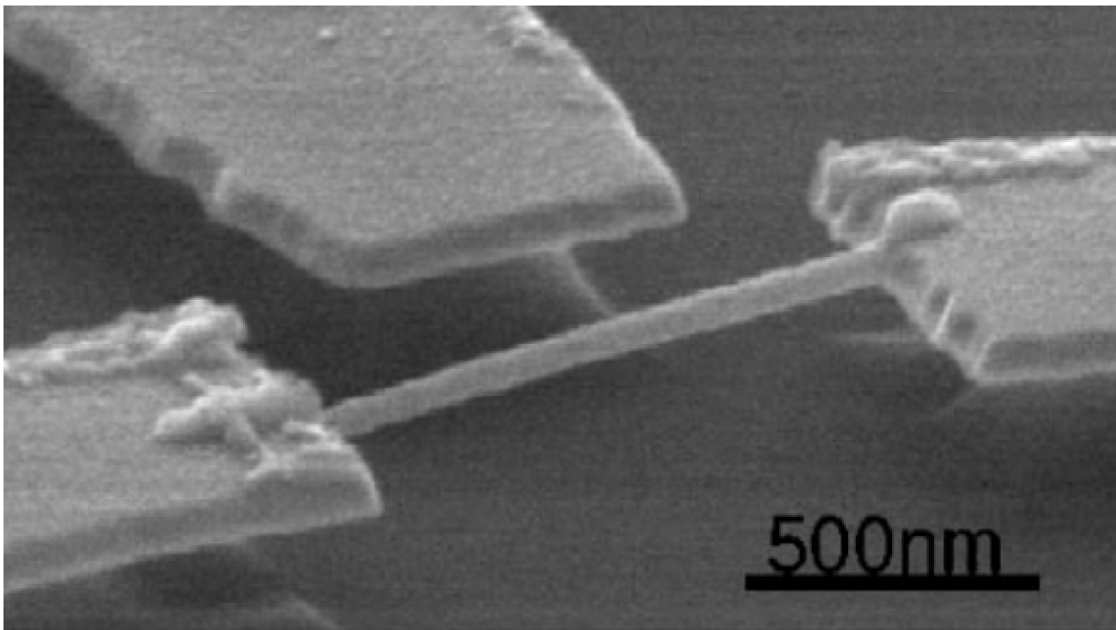

Figure 4.1 SEM image of a suspended Pt NW with 1.3 μm length and diameter of 43 nm (Ref. [68]).

Figure 4.1. The interest in such devices is due their promise as sensors and actuators, and because of the interest in their mechanical functionality at the nanoscale.

In nanoscale regime, NEMS come with extremely high fundamental resonance frequencies, diminished active masses, and tolerable force constants. The quality factors of resonance are in the range from 10^3 to 10^5—significantly higher than those of electrical resonant circuits. These attributes collectively make NEMS suitable for a multitude of technological applications including resonant sensors for ultrahigh-resolution mass sensing [70], force detection [71], quantum electromechanics [72], electromechanical signal generation and processing [73], and high-speed logic and computation [74].

In NEMS based sensors the system stimulation and transduction is sought to perform by electrical means, but the actual sensing is performed mechanically, taking advantage of the exceptionally high quality factors (in resonance) available in these systems that are normally not possible to achieve in electrical systems. There have been attempts to fabricate NEMS devices based on NWs and nanotubes (NTs). However, in addition to the problem of integration as mentioned above, NEMS sensors in general, and those based on NWs (or NTs) in particular, suffer from the problems of transduction of the mechanical signal into electrical form. Due to the fabrication difficulties, NEMS sensors have not witnessed a rapid progress in the last two decades, compared to MEMS based cantilever sensors.

Nanoelectromechanical systems (NEMS) resonators have the potential to have significant impact in

- Resonant sensors for ultrahigh-resolution mass sensing

- Force detection
- Electromechanical signal generation and processing
- Biosensor applications

Various techniques have been employed to transduce the mechanical deflection of the NEMS device, which includes optical, electron beam, magnetic, radio-frequency transmittance, and piezoresistive [71]-[75], [77]. A considerable effort has been devoted to fabricate NEMS devices using the top-down approach; however this technique has been limited due to size capabilities of the lithography system [76].

To date, most NEMS resonators have been fabricated using chemical-synthesis-based bottom-up approach and here in this project we have followed this technique. Apart from the well-known bottom up approach our InN NWs have certain distinct advantages over other type of nanostructures due to

- Having high crystalline quality
- Planar growth which is easier to process and fabricate sensors
- Less than 10 nm diameter NWs possible

4.2 Suspended NWs fabrication

InN NEMS based sensors were investigated by 3 different approaches: *1. wet etching* – NWs were first grown and trenches were patterned by e-beam lithography; once trenches were patterned, then they were etched with BOE for 1 min; *2.dry etching* – NWs were first grown and trenches were patterned by e-beam lithography; the patterns were then etched using RIE*; 3. growth of InN NWs over already etched trenches* – trenches were patterned by lithography and etched with BOE for 1 min first and then grow the NWs.

4.2.1 Wet etching

In the first method, where the NWs were grown first and then the trench was patterned, we initially performed isotropic wet etching using BOE to release the NWs from the SiO_2 layer. Of course, the etching step was preceded by the metal deposition to make contacts to the two ends of the NW. To obtain suspended NWs, trenches of 2 - 3 µm width were patterned using electron beam lithography over a certain section of the NW, and then exposed to buffered oxide etch (BOE) solution to remove the SiO_2 from underneath. However, producing NWs that are nicely suspended over the trench was found to be difficult as the SiO_2 tend to get etched as the BOE trickles along the length of the NWs. This makes the NW fall lower, and may even make them sink to the bottom level of the trench (**Figure 4.2**). In addition, the NWs can also get torn apart due to the effect of surface tension of the liquid etchant as it dries up [**Figure 4.2** (a)].The details of the fabrication process is explained next.

InN NWS were synthesized from the catalyst spot by VLS mechanism in the CVD chamber as discussed previously in the NW synthesis section (Chapter 2). The substrate consists in Si/SiO_2, 500 µm Si and 100 nm SiO_2. After the growth, single and multiple InN NWs FET were fabricated using e-beam lithography for designing and writing the patterns and e-beam deposition for metal contact pads, as explained in Chapter 3. After device fabrication, trench design and fabrication followed similar steps explained in Chapter 3 for FET fabrication. The results after trench pattern exposure are shown in **Figure 4.3**.

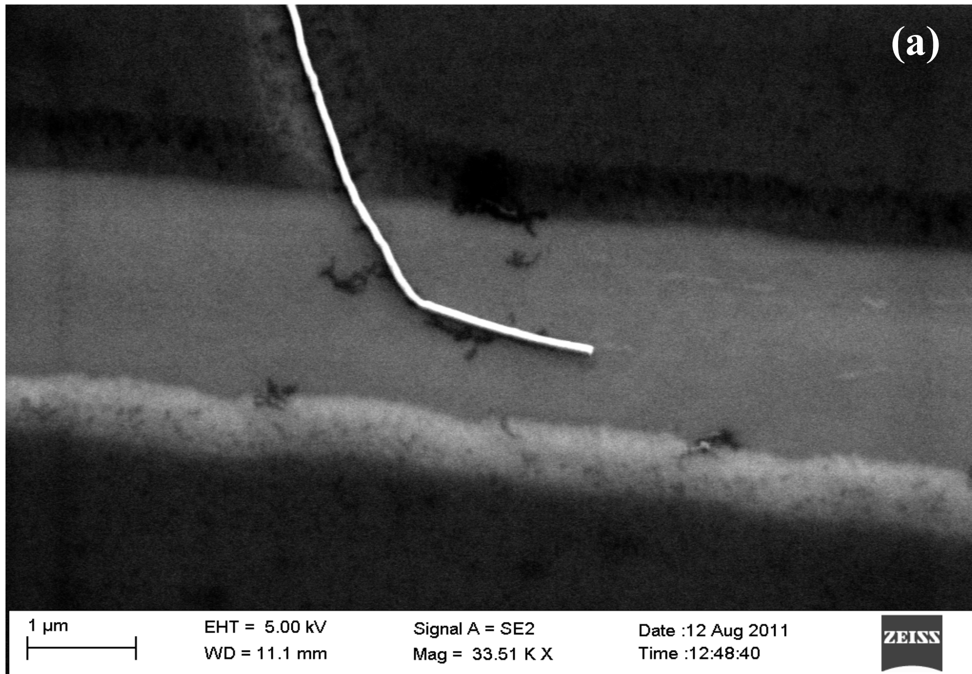

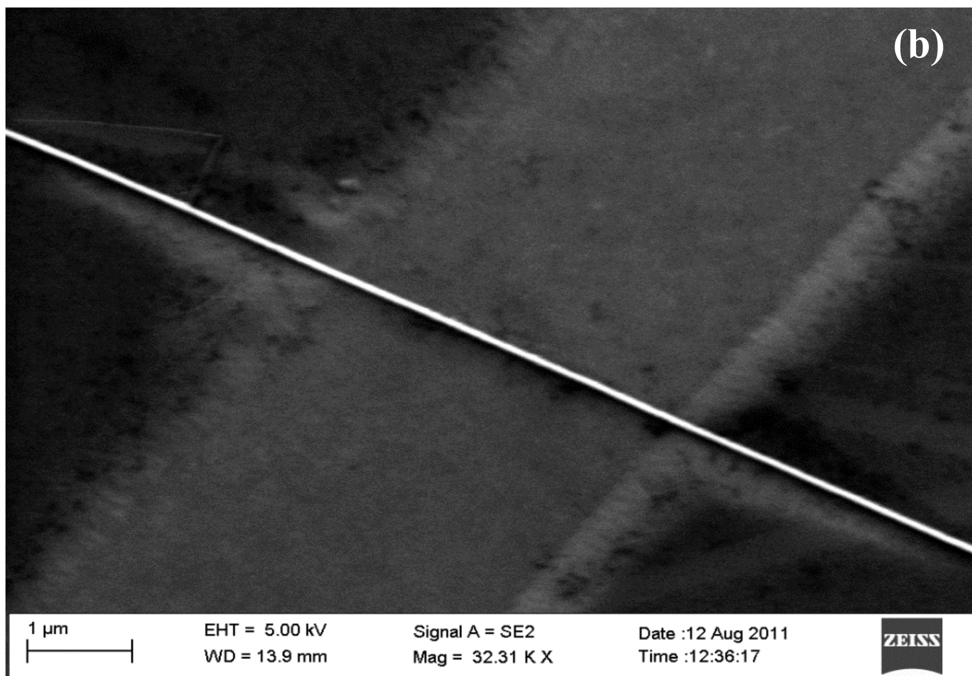

Figure 4.2 (a) A part of a NW, and (b) a complete NW hanging over a trench etched post NW growth. Note that the NWs are hanging shallowly as the SiO2 is also etched along the NW.

Here we can clearly see the opened pockets (trenches) in between the contact pads. Using e-beam lithography we were able to pattern 3 μm wide trenches in the desired location. The opened pockets were etched by submerging the sample in buffered oxide etch (BOE) solution for 1 minute. BOE is a common wet etchant using to remove thin films of silicon dioxide or silicon nitride. It is also known as buffered HF or BHF and it is used in micro and nano fabrication. BOE consists of a mixture between ammonium fluoride (NH_4F) and hydrofluoric acid (HF) [78]. One of the most common BOE solution concentrations is the 6:1 volume ration of 40% NH4F in water to 49% HF in water. The etch rate for BOE is 2 nm/sec at 25 °C [79]. Temperature can be increased to raise the etching rate. After removing the sample from BOE solution, the sample it is rinsed with DI water and the PMMA is removed by submerging the sample in acetone and then rinsed with IPA. BOE etches SiO_2 isotropically and it is observed that it etches along the NW growth direction and ultimately the NW lands on the trench surface as seen in **Figure 4.2**.

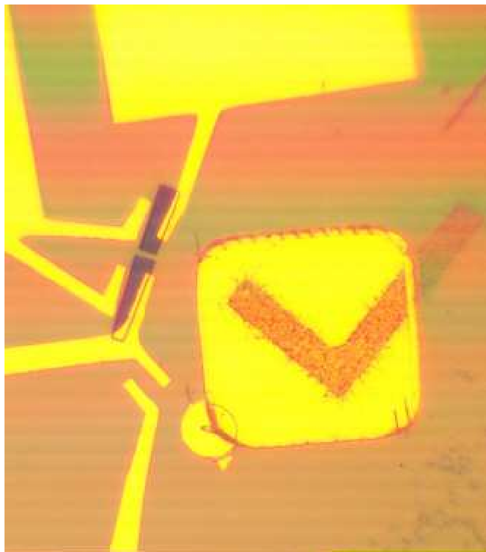

Figure 4.3 Optical image showing trench patterns after exposure and the rest of the sample being covered with PMMA.

4.2.2 Dry etching

To avoid the previous issue, of NWs sagging to the bottom of the trench, we tried the isotropic dry etch method, using carbon tetra fluoride based dry etch chemistry for SiO_2, which resulted in very nice and clean anisotropic etch. The etching results are shown in **Figure 4.4**. We can clearly see that the etching is nearly perfect with nice vertical sidewalls around the NW and the edge of the photoresist covered area. Unfortunately, there is a problem with this approach, which is that the InN NW acts as the etch-stop layer for the SiO_2 underneath, so the SiO_2 does not get etched. To fix the

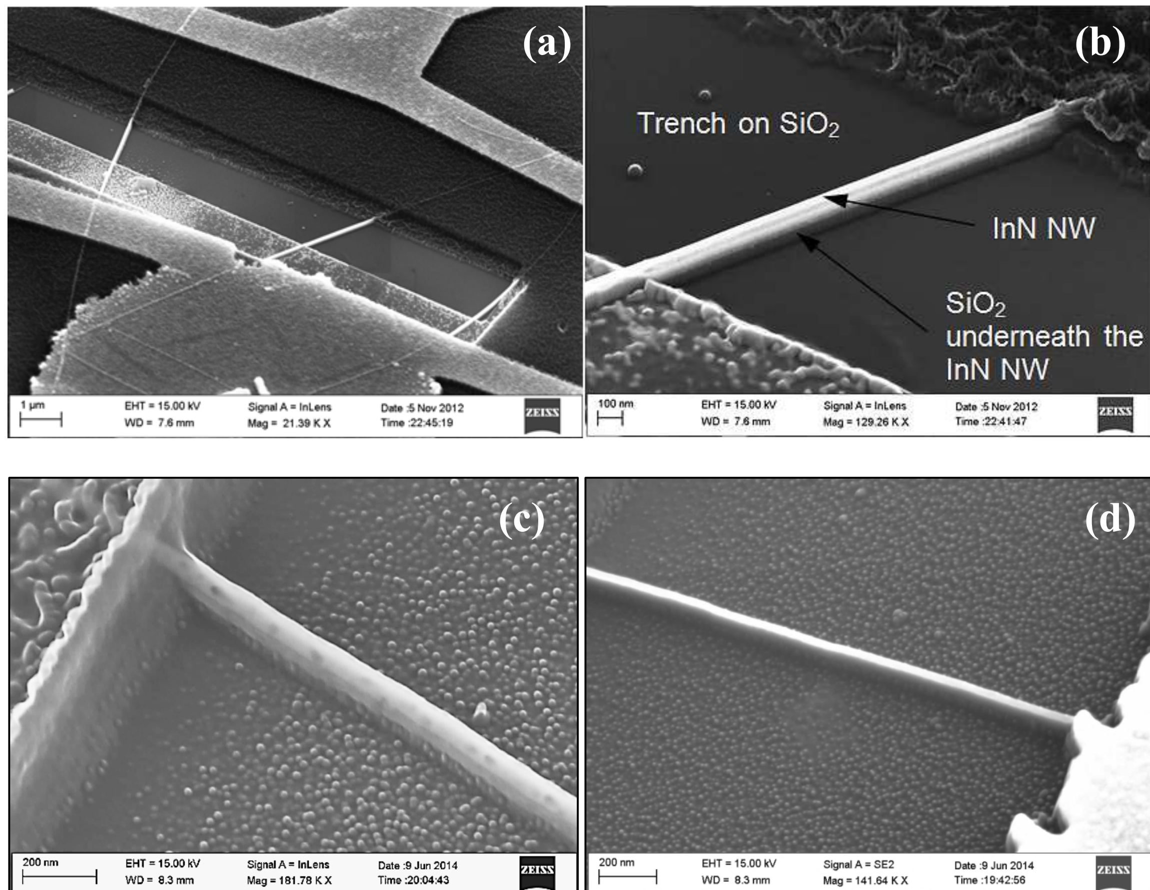

Figure 4.4 Trench etched on the SiO_2 layer, with (a) multiple InN NWs going across and (b)-(d) single NW going across trench.

issue we etched this layer by tilting the sample at 45° on alternate sides and we were able to achieve partially hanging NWs. The details of the fabrication steps are explained next.

InN NWs were synthesized by the technique explained in Chapter 2 and devices were fabricated by methods described in Chapter 3. Just like in section 4.2.1, trenches were designed and exposed using e-beam lithography (steps explained in Chapter 3, subsection 3.2.2). The opened pockets (exposed trenches) were etched this time using reactive-ion etching (RIE) technique. RIE is a dry etching technology used in micro and nano-fabrication that uses chemically reactive plasma to remove material deposited on the surface of a sample. High energy ions from the plasma attack the surface of the sample and remove the material in the designated areas [81]. Schematic of a RIE system is shown in **Figure 4.5** and consists of 2 electrodes (1 and 4), which create an electric field (3) meant to accelerate ions (2) towards the surface of the wafer (5) [80].

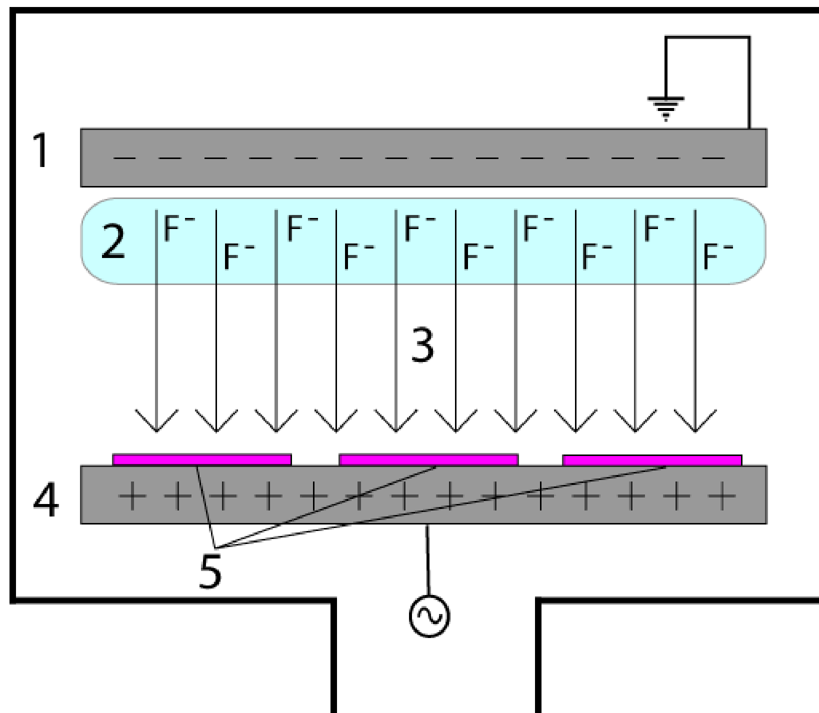

Figure 4.5 Schematic diagram of a RIE system (Ref. [80]).

RIE recipe used to etch SIO_2:

- Gases: CHF_3 and O_2
- Pressure: 200 mT
- Power: 200 W
- Time: 3 min
- Total gas flow: 24 sccm

The results are showing in **Figure 4.4** and we can clearly see that SiO_2 forms a wall underneath the nanowire due to anisotropic etch of this technique. To remove the remaining layers of SiO_2 we performed RIE, but tilting the sample 45° from both sides. The results of three different samples (A, B and C) are shown in **Figure 4.6**. Even though this procedure was successful by getting partial suspended NWs, it is not an efficient technique, as our NWs grow in different directions. It is very difficult to fabricate single NW devices on the same sample and have them oriented in the same direction. This is very important when etching from both sides of the NW using RIE technique.

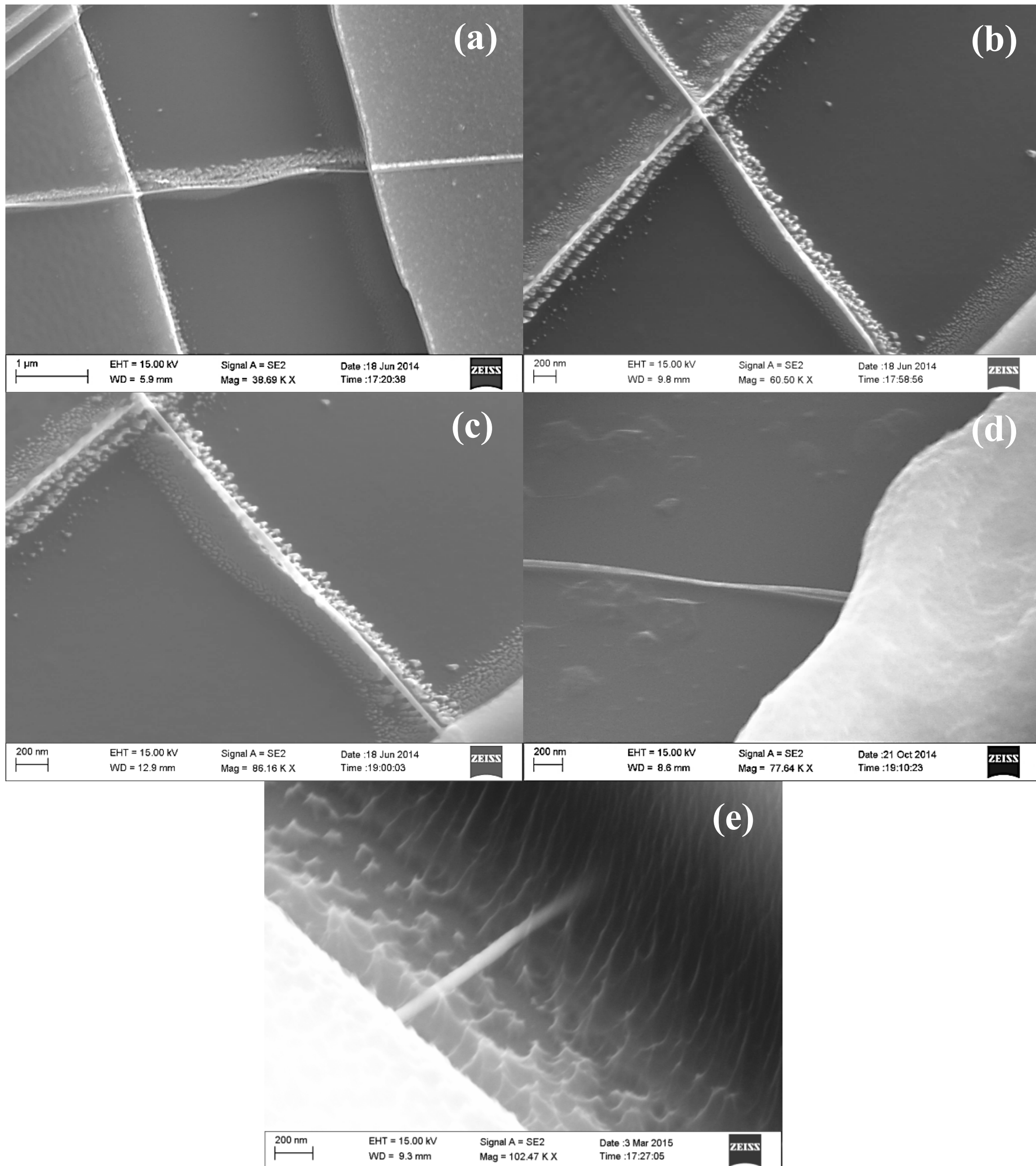

Figure 4.6 SEM images of NWs etched by RIE. (a) sample A from top, no tilt, (b) - (c) sample A tilted 40°, (d) sample B tilted 40°, (e) sample C tilted 40°.

Another technique used to release the NWs was a combination of RIE and BOE vapor etch. In this case we noticed that the NWs were moved sideways after the etch (**Figure 4.7** and **Figure 4.8** white dotted lines) and they also looked separated from the

oxide in place, but no apparent sideways movement was observed (**Figure 4.7** and **Figure 4.8** green dotted lines). This approach has a possibility in getting suspended nanowires, but the etch process needs to be optimized first. The BOE vapor etch method has an advantage over the wet etching process in that the oxide along the NWs will not get etched and cause the NWs to fall at the bottom of the trench.

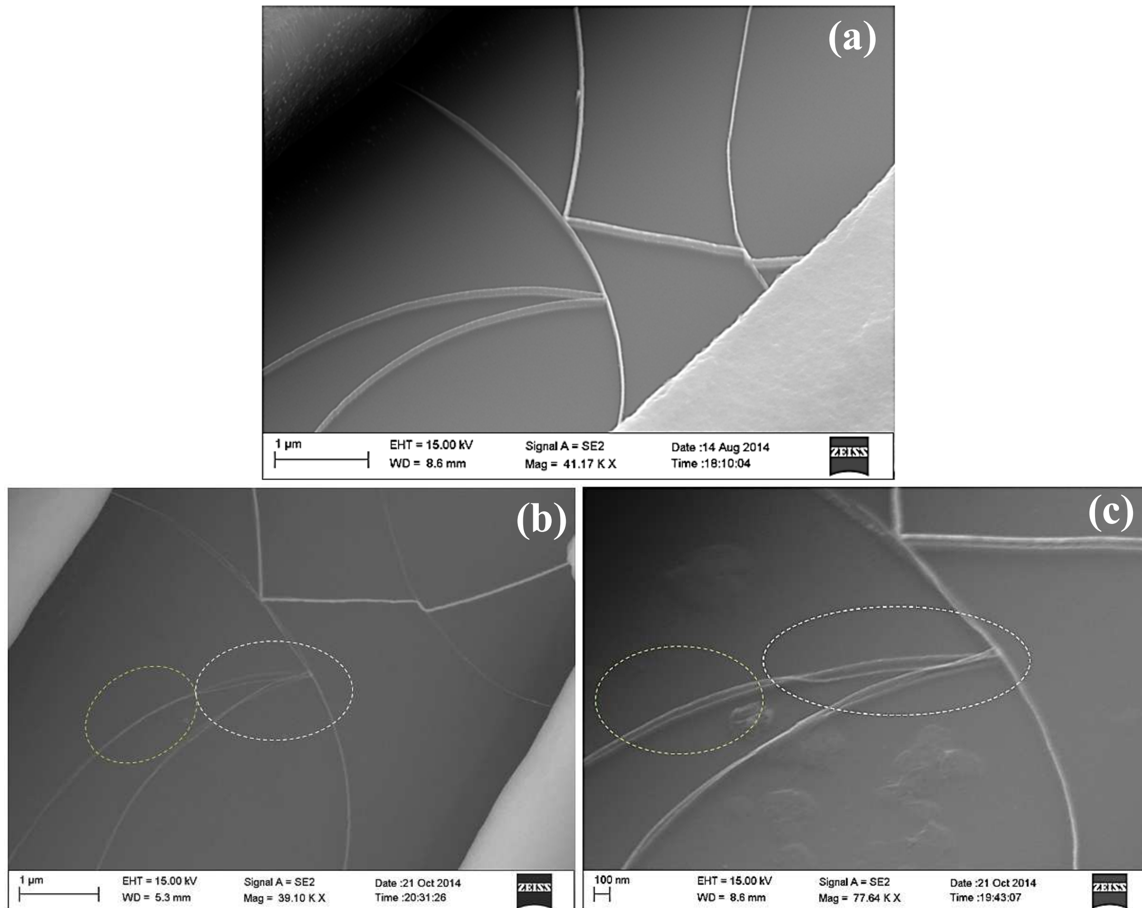

Figure 4.7 SEM image of InN NW etched (a) by RIE, tilted 40°, (b) by RIE and BOE vapor etch without tilt and (c) by RIE and BOE vapor etch, tilted 40°.

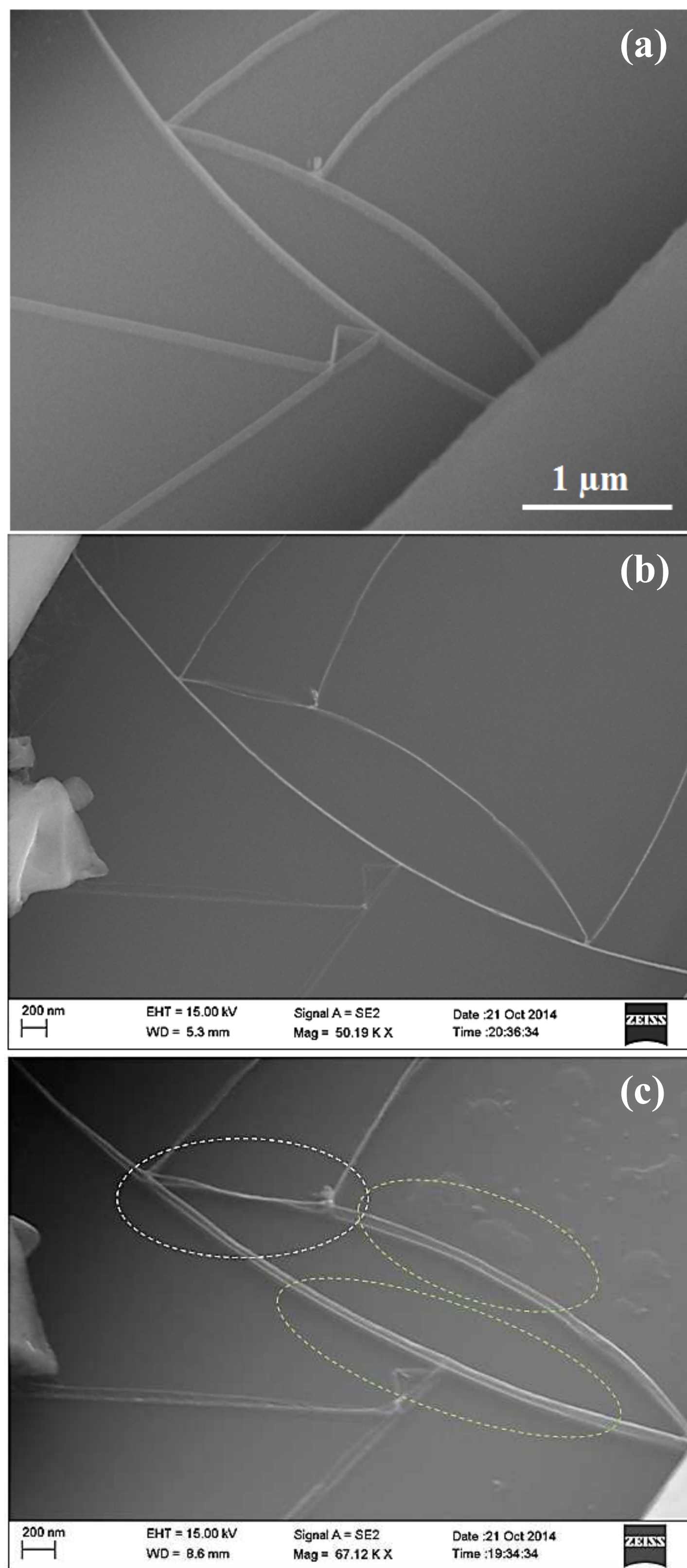

Figure 4.8 SEM image of InN NW etched (a) by RIE, tilted 40°, (b) by RIE and BOE vapor etch without tilt and (c) by RIE and BOE vapor etch, tilted 40°.

4.2.3 Growth of InN NWs over already etched trenches

In this approach, the trenches were etched first and the NWs were then grown. **Figure 4.9** (a) shows an array of trenches with Au catalyst spots on two sides of each trench. **Figure 4.9** (b) shows a magnified image where the trench can be seen to have a width of 2 μm, and the catalyst spots are seen to have a mean diameter of 1 μm for easy growth of the NWs. To solve the previous issues, the trenches were etched first and the NWs were then grown, and a fraction of the NWs grew over the trenches spontaneously, getting suspended over the trenches, which can then be used as resonators after contacts deposition at both of their ends by focused ion beam (FIB) technique. **Figure 4.9** (c) shows an SEM image showing NWs growing randomly from catalyst spots patterned near a particular trench, of which only a few would actually be going over the trench. **Figure 4.9** (d) shows a single NW going over a trench which is also suspended. This technique will avoid previous issues, such as oxide getting etched along the NWs and causing them to sag, and also oxide not being etched under the NWs if using RIE process.

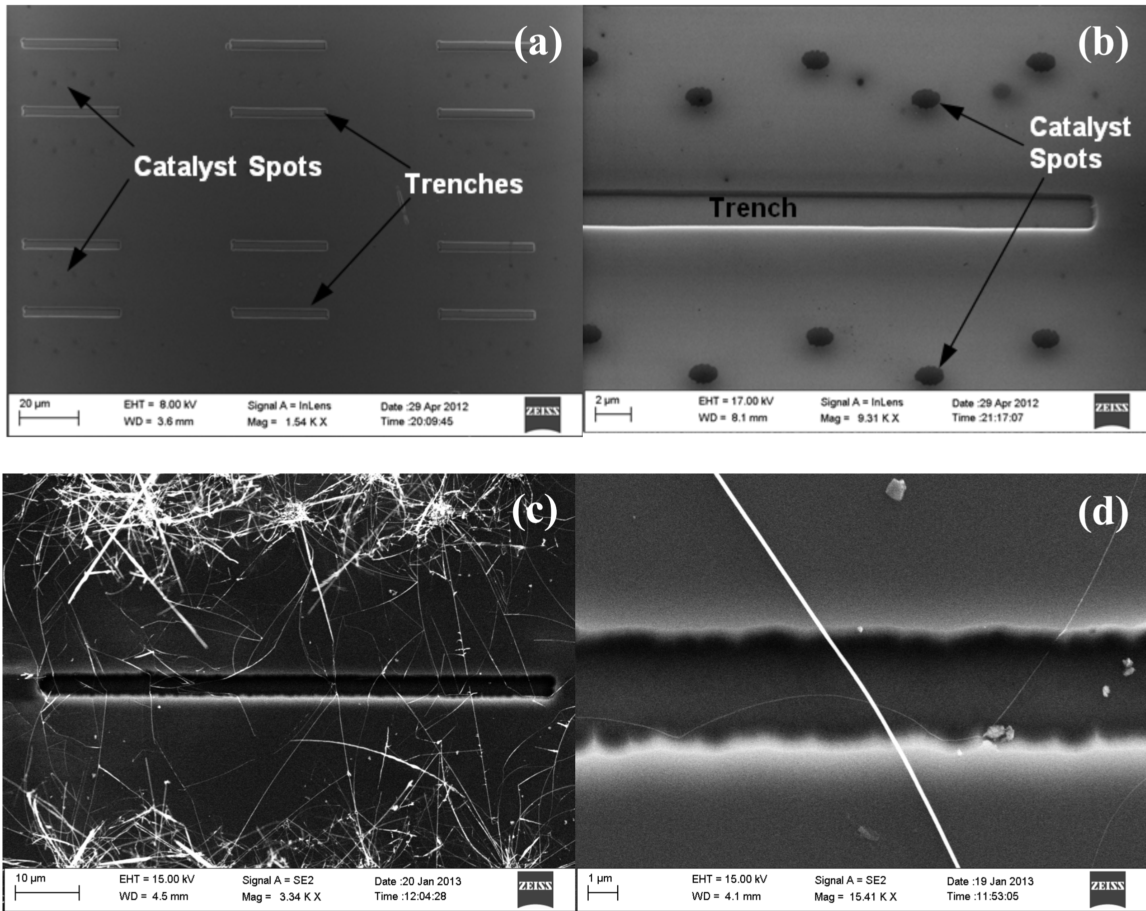

Figure 4.9 (a) SEM image of trenches made using e-beam lithography, with multiple Au catalyst spots patterned around them. (b) A magnified image of a trench pattern with Au catalyst spots around it. (c) NWs growing randomly from catalyst spots deposited near a pre-patterned trench. (d) A single suspended NW going over the trench.

CHAPTER 5

GRAPHENE/INN THIN FILM BASED SENSORS

5.1 Introduction

Gas sensors are critical to many applications in defense and homeland security. Present technology thin film gas sensors use metal oxide films, for which the conductivity changes due to electron or hole doping by adsorbed gas molecules. The resulting resistive gas sensors are useful in industrial process control and monitoring applications. However, metal oxide based gas sensors typically have limited sensitivity and selectivity, which is not sufficient for defense related detection of chemical and biological threats. InN is a unique semiconductor material, which can have a high surface accumulation of electrons. Electrical conductivity for InN films is concentrated in a thin surface layer, and can be extremely sensitive to adsorbed gas molecules. This chapter describes development of high sensitivity gas sensors based on InN thin films.

InN and graphene are two materials that are being extensively studied in recent years because of their exceptional properties. InN is well-established for optoelectronic and sensing applications because of unique characteristics such as high electron accumulation near the surface, long term chemical stability, high sensitivity to various gases, organic chemical species and bio molecules [82]-[92].

There have been only a few reports regarding InN sensing, but Lu *et al* reported electrical response of InN thin films surface under the exposure of various chemicals

[93]. These films range from 20 nm to 80 nm thickness and showed a fast response to exposure of some solvents (methanol, water and isopropanol) with results in increase of surface carrier density. Kao *et al* reported a sub-ppm acetone gas sensor using 10 nm thick InN [94]. They showed that ultrathin InN epilayer has high sensitivity due to its strong electron accumulation on roughly 5–10 nm deep layers from the surface. Platinum as catalyst can increase output current signals by 2.5-fold as well as reduce response time by 8.4-fold in comparison with bare InN. Basilio *et al* presented electrochemical characterization of InN thin films for biosensing applications [95]. They showed potentiostatic and photo response measurements indicating detection of dopamine in various solutions.

Graphene, at the same time, offers exceptionally high carrier mobility and surface sensitivity due to high surface to volume ratio. Graphene has become highly attractive because of its essentially two-dimensional nature, which allows absorbed molecules to readily affect its conductivity through surface adsorption by changing carrier concentrations. Graphene gas sensors based on changes in surface work function, conductance, low frequency noise and frequency of the surface acoustic waves have been reported and ultra-high sensitivity down to a single gas molecule has been demonstrated [96]-[99]. In a recent work by Singh *et al*, electrical tunability of molecular doping of graphene by NO_2 and NH_3 was demonstrated using back-gated field effect transistors [100].

Though sensors based on InN and graphene have already been reported, sensing properties of graphene/InN heterostructures have not been explored yet. In this chapter, we will present how we designed and fabricated graphene/InN heterojunction devices

that are suitable for gas sensing because of the tunable barrier height and conductivity across the heterojunction in presence of different analyte gas and vapor molecules.

The device structure consists of a 100 nm thick InN thin film grown on GaN layer on sapphire substrate. High quality graphene is grown separately using CVD growth technique and transferred on an insulated region of InN thin film with partial overlap on the InN thin film to form a heterojunction. After making ohmic contact to both graphene and InN, the device is used to study sensitivity to various toxic gases and volatile organic compounds under appropriate biasing conditions.

5.2 Fabrication of devices

InN samples were obtained from Structured Materials Industries (SMI), Inc where approximately 100 nm thick InN thin films were deposited on 4 μm thick GaN on c-axis (0001) epi-ready Al_2O_3 substrates in an experimental vertical MOCVD reactor. The reactor pressure was varied from 100 Torr to atmospheric pressure with growth temperature being 450-580 ^oC. Indium precursor was Trimethyl Indium (TMIn) with 1.1-10.5 μM/min flow rate and primary nitrogen source was Ammonia (NH_3) with 11.2-100 mM/min flow rate in presence of nitrogen carrier gas. InN formation and electrical properties were confirmed by SMI, Inc via optical microscopy, Interferometry, X-Ray Fluorescence Analysis (XRF), X-Ray Diffraction (XRD) and four point probe measurements.

Graphene samples were synthesized through chemical vapor deposition (CVD) on 99.999% pure Cu foil in a quartz tube furnace at 1000 ^oC and 4-10 Torr pressure. CH_4 was used as the precursor (flow rate 2-40 sccm) along with H_2 (flow rate 15-50 sccm).

The quality of graphene was determined using Raman spectroscopy and atomic force microscopy (AFM).

The fabrication process started with etching one portion of InN film away using hot 10 M KOH solution. The etched region was then encapsulated using epoxy. Graphene was then transferred on the insulating layer with partial overlap on the InN thin film to allow vertical conduction between graphene and InN. The transfer process of graphene involves several steps. The top side of graphene (grown on Cu foil) is protected by spin coating of PMMA twice at 3000 rpm for 40 sec. The PMMA coated sample is loaded upside down in the RIE chamber to expose the bottom of the graphene. Graphene grows on both sides of Cu foil, but the bottom side is of inferior quality compared to the one grown on top. This bottom side layer of graphene is removed by oxygen plasma at 150 W for 180 sec. After that, the sample is placed in concentrated Cu etchant ($FeCl_3$) over night for complete removal of Cu. This results in graphene/PMMA layer floating in the solution, which it is rinsed multiple times with DI water. Once sample is cleaned, InN thin film sample is placed underneath the floating graphene/PMMA and positioned in the needed area. The substrate containing graphene/PMMA is allowed to dry overnight in air at room temperature and then baked at 220 °C for 5 min to allow reflow of PMMA in order to heal the wrinkles in graphene and to ensure good adhesion of graphene on the substrate. The sample is then dipped in acetone for 3-4 hours to remove PMMA from top of transferred graphene and followed by organic cleaning of the sample with acetone and IPA. After graphene transfer, ohmic contacts were formed on InN and grapehen by depositing Cr/Au (20/80 nm) using e-beam deposition.

Figure 5.1 shows a schematic diagram of the experimental setup of graphene/InN sensor. The inset shows a photograph of the device before the contacts were deposited and graphene was coated with PMMA.

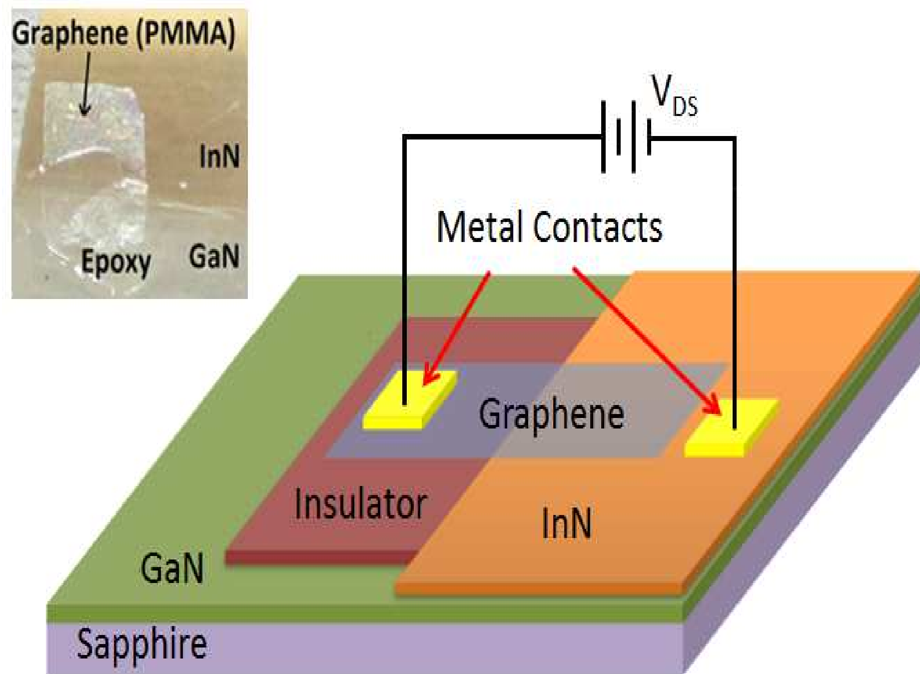

Figure 5.1 Schematic diagram of the graphene/InN sensor. Inset shows a photograph of the device before putting contacts, graphene is coated with PMMA.

5.3 Electrical characterization

The I-V measurement was performed using Keithley source measurement unit (SMU) 2612. In **Figure 5.2**, the measured I-V characteristic of the graphene/InN heterojunction is shown. It is observed that the device shows reasonably good Schottky behavior with a threshold voltage of 0.6 V and a reverse breakdown voltage of -1.8 V. The I-V characteristics have two regions around 0.6 V and -1.8 V where conductivity changes sharply. These two biasing regions are ideal for sensing as a little change in

barrier height due to the presence of gas molecules can result in rapid change in conductivity.

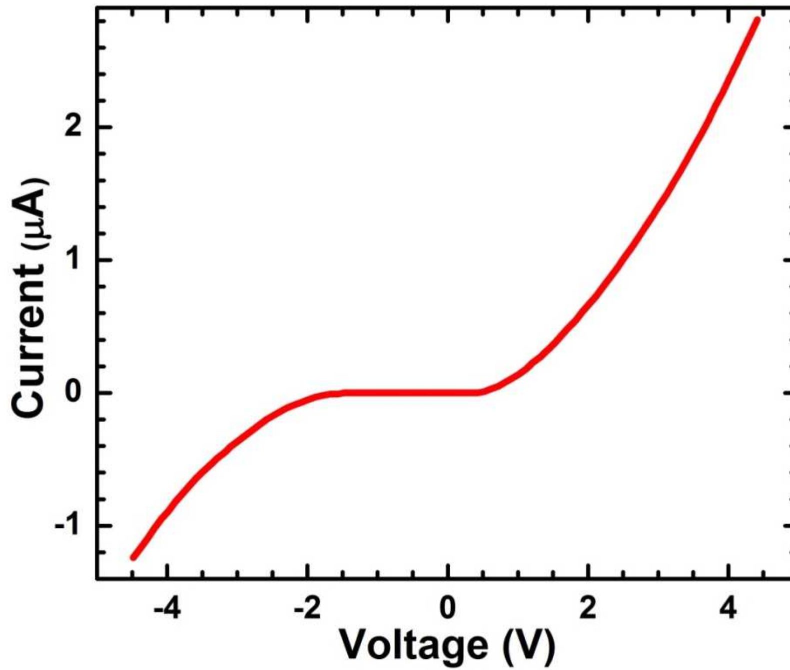

Figure 5.2 Graphene/InN junction I-V characteristics which exhibits Schottky behavior.

5.4 Sensing results

The experiments were done by placing the devices in a sealed chamber with electrical feed through and gas inlet/outlet. Sensing experiments were carried on by purging and degassing a series of gases (air, pure N_2, diluted NH_3 and NO_2 and vapors in various concentrations) at room temperature. A bubbler was used to flow pure N_2 as carrier gas in water and acetone, the saturated vapor from the outlet of bubbler was then mixed with pure N_2 to make the desired concentration of vapor. For electrical measurements, drain and gate electrodes were biased by Agilent E3649A Dual O/P DC power supply and the sensor output was acquired by Agilent 34970A Data Acquisition/ Switch unit.

Figure 5.3 and **Figure 5.4** show a comparative image of graphene/InN heterojunction device and simple InN thin film device in terms of sensitivity to water vapor. For graphene/InN device, water vapor diluted with N_2 brings about 5% change in current whereas for InN thin film device, the change is less than 0.5%. Besides, the former device exhibits a recovery time less than 5 seconds which is significantly better than the 30 seconds recovery time of the later one.

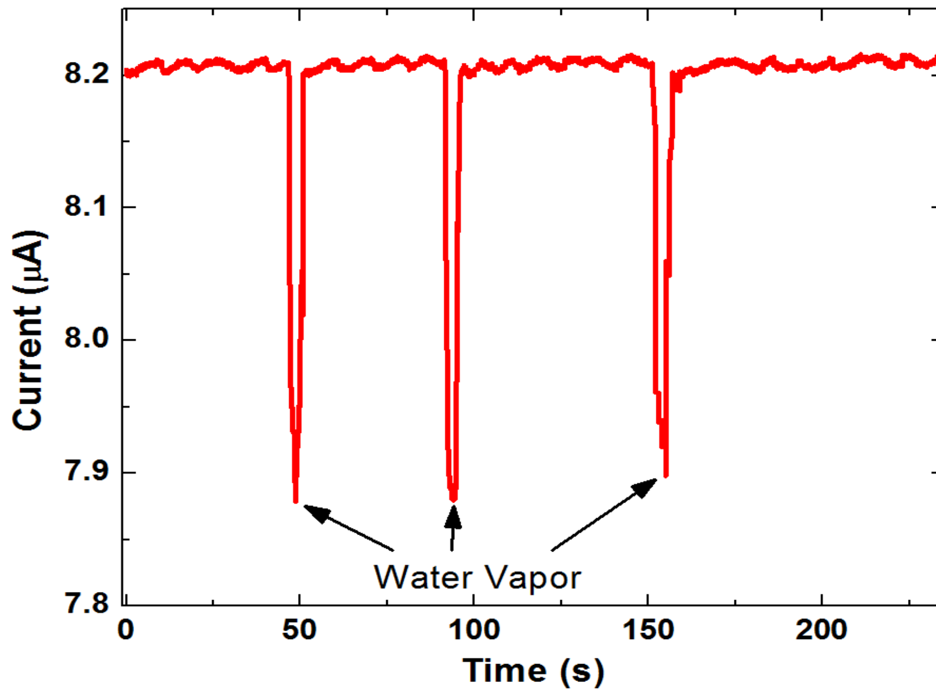

Figure 5.3 Water vapor sensing by graphene/InN thin film sensor under a bias voltage of 0.5V.

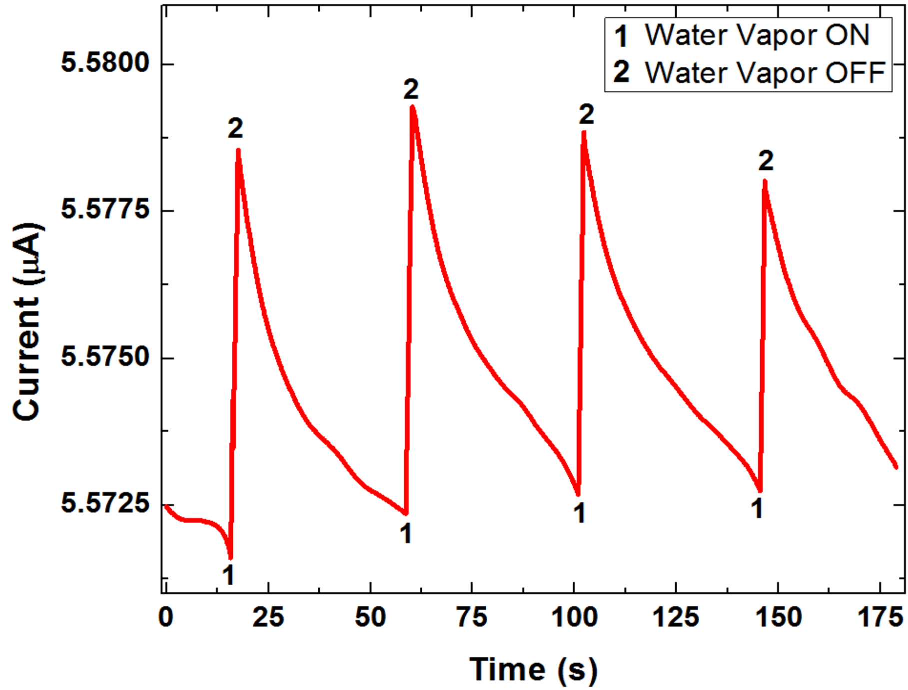

Figure 5.4 Water vapor sensing by InN thin film sensor under a bias voltage of 0.5V. "1" and "2" denotes the beginning and stopping of the water vapor flow.

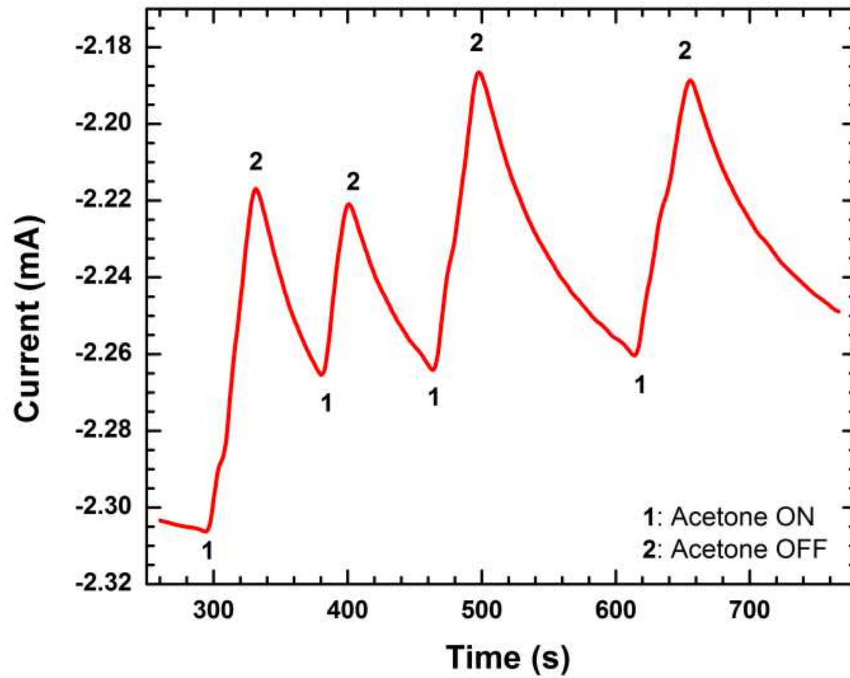

Figure 5.5 Diluted acetone vapor (100 ppm) sensing by graphene/InN sensor under -5V bias. "1" and "2" denotes the beginning and stopping of the acetone vapor flow.

In **Figure 5.5**, sensing result for 100 ppm acetone vapor is shown. In **Figure 5.6**, the sensing responses of the sensor upon exposure to various concentrations of NO_2 and NH_3 (from 100 ppm to 30 ppb) are shown. An extremely high sensitivity is observed with a clearly distinguishable response down to 30 ppb (**Figure 5.6** (a)). We can notice that sensing started from 10 ppm where a change of more than 700% in current was observed. For lower concentrations it takes longer to reach steady-state because of the low amount of gas flowing, but still for 30 ppb a change of about 80% was observed. This means that lower concentration sensing might be possible. For NH_3, the sensing response is opposite to NO_2 (due to well-known donor and acceptor behavior of NH_3 and NO_2, respectively) as seen in **Figure 5.6** (b). Although the device showed quite high sensing response, down to 100 ppb, with a change of 3% in current, the magnitude of sensing response for NH_3 is much smaller than NO_2 due to its lower charge transfer per molecule.

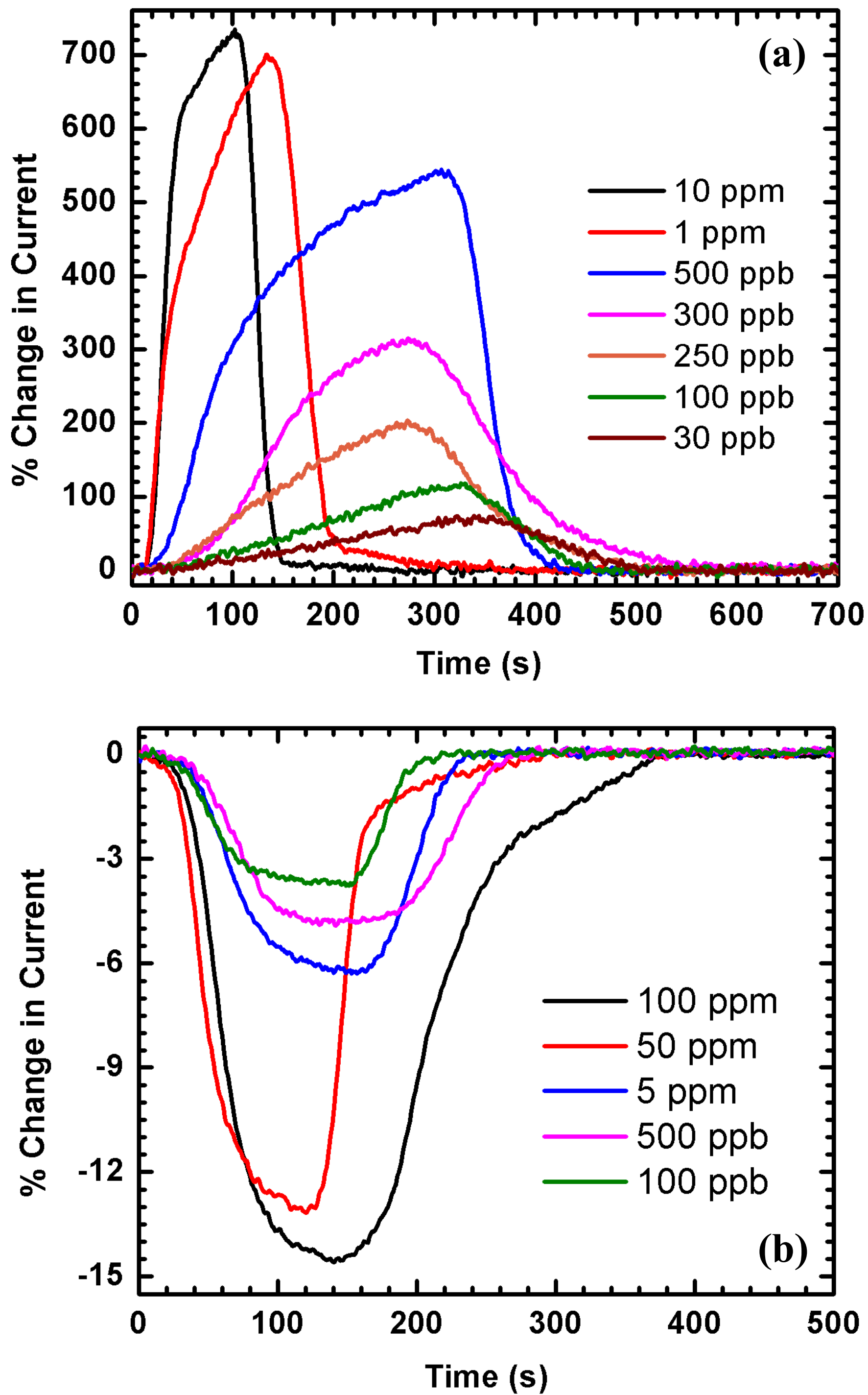

Figure 5.6 Sensing responses for (a) NO_2 and (b) NH_3 gas for graphene/InN thin film device under a voltage bias of 1V.

CHAPTER 6

GRAPHENE/INN NW BASED SENSORS

6.1 Introduction

Volatile organic compounds (VOC) are organic chemicals with high vapor pressure at room temperature. Some of the sources that emit VOCs are biological (produced by plants, animals, microbes, fungi) and anthropogenic (paints, benzene - found in environmental tobacco smoke, methylene chloride - found in adhesive removers, perchloroethylene – used in dry cleaning, chlorofluorocarbons and chlorocarbons – used in cleaning products and refrigerants) [101]-[103]. Carbon monoxide is a very dangerous gas, which is odorless and difficult to detect. Ammonia, a gas with a pungent smell, is toxic and in excess could cause irritation to the eyes and mucous membranes (respiratory and digestive tracts). These are only a few out of many dangerous gases that surround us and are harmful not only to humans, but animals and plants as well.

Gas detectors are devices that detect the presence of gases in an area. Gas adsorption onto a semiconductor produces a conductance change and this phenomenon was observed by Bardeen *et al*. 60 years ago. Since then, a great amount of research has been focused to realize commercial semiconducting devices for gas detection [104]. There are two main lines being developed at the same time: first is to modulate the properties in order to enhance the sensitivity, selectivity and stability to a particular gas, and second is to realize an array of such sensors [105].

InN is a unique semiconductor material, which has a high surface accumulation of electrons and the electrical conductivity is concentrated in a thin surface layer, and can be extremely sensitive to adsorbed gas molecules [106]. Graphene, on the other hand, has drawn huge research interests in sensing applications due to its extraordinary material properties including high charge carrier mobility [107], very high thermal conductivity [108], mechanical strength [109] and high degree of chemical inertness at room temperature [110].

There are more than two hundred types of VOCs found in human breath and abnormal concentrations of it correlate with unhealthy body conditions, like acetone for diabetes [111] and ammonia gas for renal disease [112]. Kun-Wei Kao *et al*. reported the fabrication of a gas sensor made of 10 nm thickness InN thin film that achieved the detection of 0.4 ppm acetone. A gas sensor device with sub-ppm acetone detection capability is very important in the development of non-invasive monitors of early diagnosis of diabetes [113]. Pt-coated InN nanorods were fabricated and reported by Kryliouk *et al*., and the devices were used for hydrogen detection at room temperature [114]. Hydrogen is an odorless, carbon-free gas that is becoming a concern regarding climate change, being difficult to detect due to lighter mass than air and rapid diffusion.

Graphene, a true two-dimensional (2D) crystal, has been investigated in the last few years due to the amazing properties it possess mentioned earlier. Graphene based sensors have been demonstrated to be capable of detecting down to a single analyte molecule [115]. Two types of graphene sensors have been demonstrated so far such as physical sensors, which have been shown to sense physical quantities such as pressure, magnetic field, strain etc., and chemical or biological sensors, which have been shown to

sense various analytes such as ppm or sub-ppm level of NO_2 and various kinds of bio-molecules and bio-markers.

Though sensors based on InN (mostly thin films) and graphene have already been reported, sensing properties of graphene/InN NW heterostructures have not been explored yet. Graphene/InN NW heterostructure based sensors offer the possibility of surface barrier modulation and high detection sensitivity. Graphene on InN serves the dual purpose of an electrode as well as a functionalization layer. Since InN NWs have much higher surface area better sensitivity is expected.

Two different methods of fabricating graphene/InN NW heterostructures have been investigated. In the first method, the heterojunction was constructed by transferring graphene on the NW sample, where partial overlapping of graphene and NWs were achieved by bare hand. The non-lithographic method, found out to be very crude and vastly unrepeatable, was succeeded by a different approach where a controlled overlapping was achieved through optical lithography. The fabrication steps for each method and characterization results will be explained in details in the coming sections.

6.2 Non-lithographic patterning of graphene on InN NW sample

6.2.1 Fabrication of devices

Patterns for nanowire growth were fabricated using optical lithography and 2 nm Au was deposited using e-beam evaporator (both methods are explained in details in Chapter 3). Graphene was transferred on already grown InN NW sample (**Figure 6.1**). The steps of transfer process consist of PMMA coating of the graphene grown on Cu foil and etching of Cu with $FeCl_3$ to release the graphene/PMMA bi-layer. Once the graphene/PMMA bilayer is transferred on the sample, the PMMA is removed with

acetone (full details of graphene transfer process are explained in Chapter 5). Ensuring that graphene touches the NWs, but not the catalyst (which would produce a short during electrical characterization of the device) was done merely by visual inspection. If the result was not satisfactory, the graphene/PMMA bilayer, still soaked in water, was moved using a tweezer. This technique is very challenging for several reasons: (1) it requires moving the bilayer by a few microns only using bare hands while naked eye cannot see the NWs; (2) it is hard to avoid damaging the graphene due to the multiple movements of graphene using the tweezer; (3) while drying, the bilayer gets stretched and may end up in an unfavorable position; (4) it is hard to align the graphene layer consistently along the Au catalyst throughout the sample. These issues are observed in **Figure 6.1** where it can be seen that only a corner of graphene is touching the NWs, also the edge of the graphene got torn due to the multiple movements. This is a serious problem; as it greatly reduces the probability of obtaining good working devices, and it will never be possible to achieve consistency and repeatability through this process.

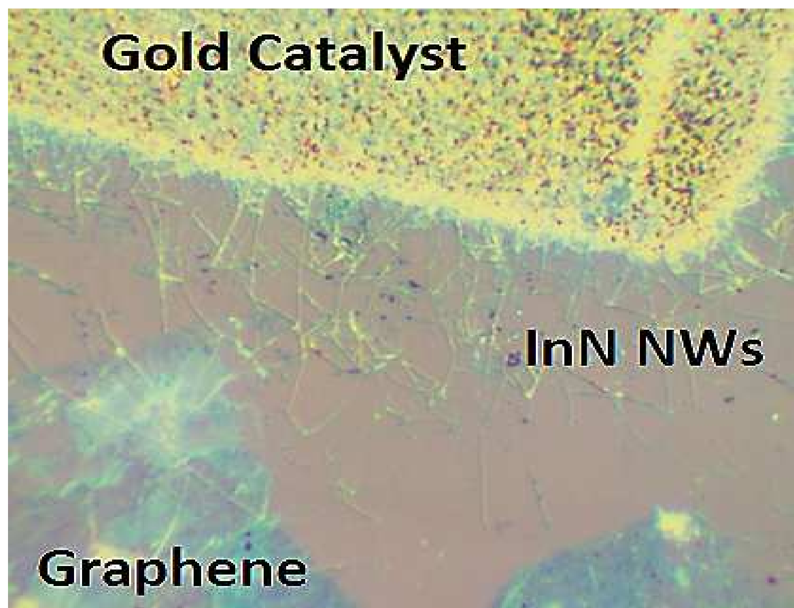

Figure 6.1 Optical image of graphene/InN NW heterojunctions.

6.2.2 Electrical characterization

The I-V characteristics (**Figure 6.2**) of this device show reasonably good Schottky behavior with a threshold voltage of 0.8 V and a reverse breakdown voltage of -1.3 V. These two regions are very important due to the exponential change in conductivity, which makes these devices ideal for sensing. However, obtaining a working device like this one requires lots of trials due to the lack of control in the overall process.

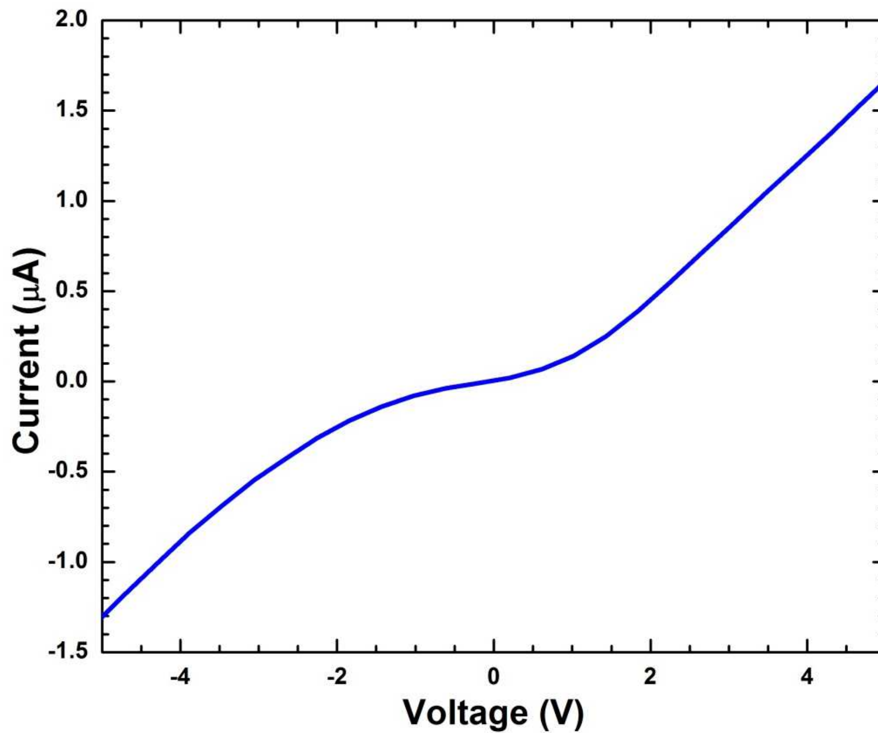

Figure 6.2 Graphene/InN NW heterojunction I-V characteristics which exhibits Schottky behavior.

6.3 Lithographic pattering of graphene on InN NW sample

In this method, devices were fabricated on Si/SiO_2 wafer as well. Although it is possible to use dry or wet thermal oxide for this purpose, we primarily used dry thermal oxide due to its superior quality as outlined in Chapter 3. Fabrication method includes

various steps such as growth, metal contacts deposition, graphene transfer, graphene etch. These steps are explained in detail in the next subsection.

6.3.1 Fabrication of devices

Optical lithography (mask aligner Karl Suss MJB3) was the primary tool used for fabricating InN NW/graphene heterostructures. As mentioned before, photolithography uses light to transfer a geometric pattern from a photomask to a light-sensitive photoresist. This process is more precise and gives us the ability to fabricate microscale devices. The substrate used was 100 nm dry thermal SiO_2 on 500 μm Si; the advantages of using this type of wafers were mentioned in Chapter 3. After cleaning the sample (steps mentioned in Chapter 3), the sample was coated first with HMDS, an adhesion promoter;, and then coated with positive resist AZ1518. A baking step was used to improve the adhesion and remove any remaining solvent from the resist. The sample was then placed under the UV light using a positive mask and exposing the sample for 10 seconds. After exposure the sample was developed in a mixture of AZ400K and DI water and rinsed with DI water. 2 nm Au was deposited in the opened areas using e-beam deposition and excess metal film outside these areas were removed by submerging the sample in acetone for 5 minutes. The lift-off process did not take long in this case due to the thin metal deposited.

The recipe for using positive resist AZ1518 is as follows:

1) Spin coat the sample with adhesion promoter HMDS at 5000 rpm for 10 sec.
2) Spin coat the sample with AZ1518 at 5000 rpm for 30 sec.
3) Bake the sample at 110 °C for 90 sec.

4) Expose sample for 10 sec.

5) Develop sample in AZ400K : DI water (1:4) for 60 sec.

6) Rinse sample with DI water for 30 sec.

Following the lift-off procedure, InN NWs were grown in the horizontal furnace according to the growth process explained in Chapter 2 and the results are showing in **Figure 6.3**.

Figure 6.3 InN NWs grown out of 2 nm Au catalyst (catalyst pattern dimensions: 5 μm x 100 μm and 5 μm x 200 μm).

Before the next fabrication step, sample was cleaned using the procedure presented in Chapter 3. To remove any dust particles or residues, the sample was cleaned using solvents as mentioned before. Then the sample was coated with AZ1518 and was exposed to UV light using the mask aligner. After exposure and development (**Figure 6.4** (a)), the sample was introduced in e-beam evaporator chamber and 20nm/80nm Cr/Au metal contacts were formed (**Figure 6.4** (b)). Graphene was transferred on the sample as explained in Chapter 5, followed by the same optical lithography process again to open areas outside of device boundaries.

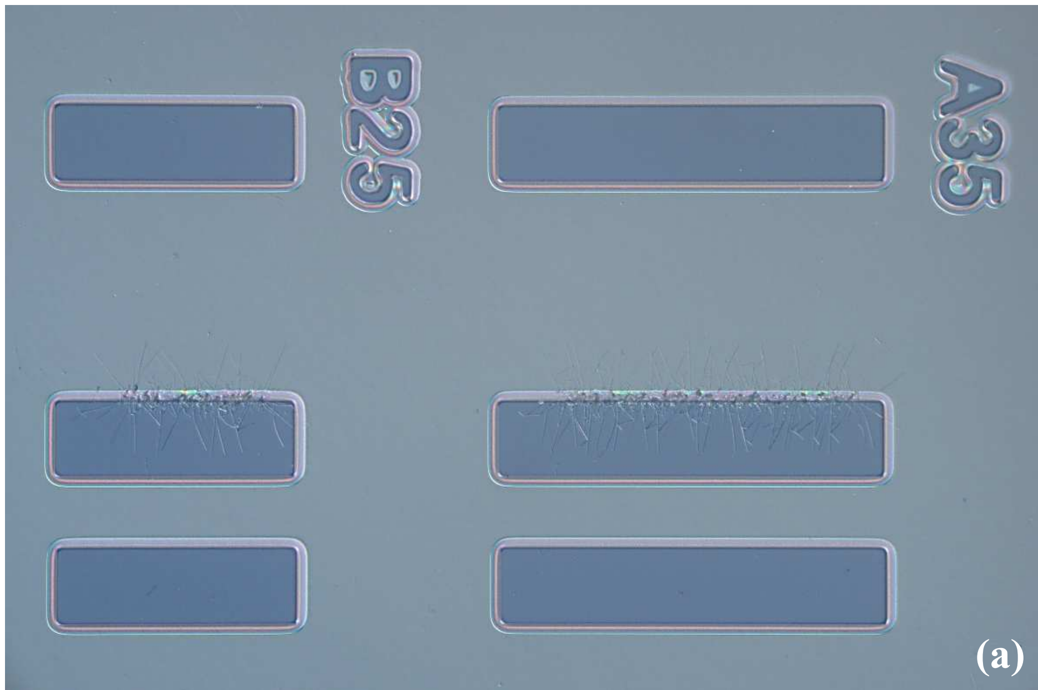

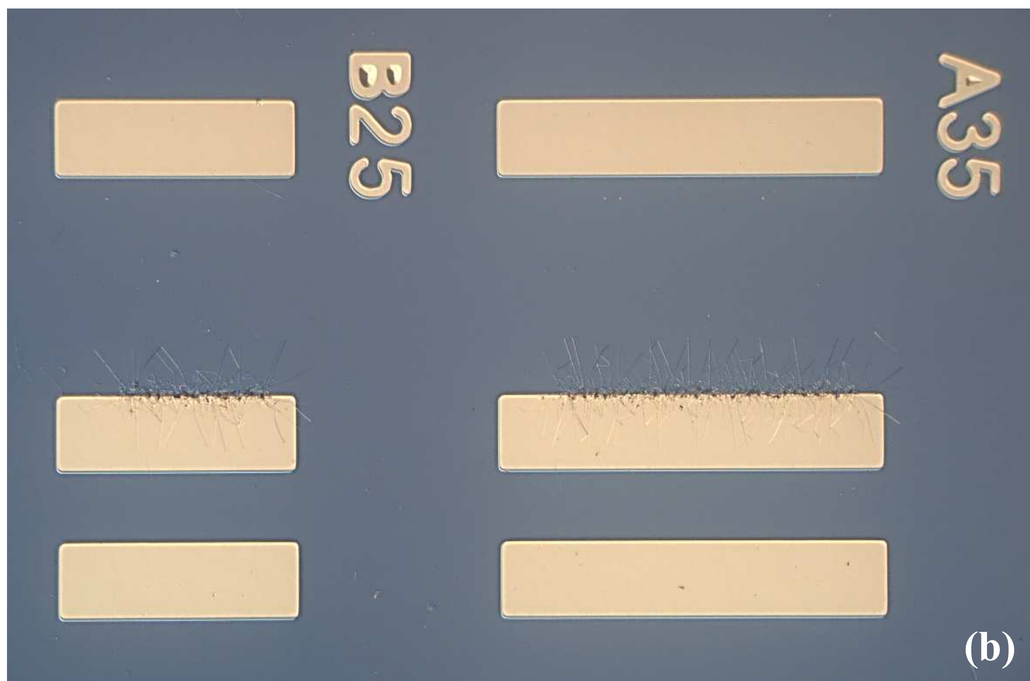

Figure 6.4 Optical microscope images of (a) optical lithography pattern of metal contacts and (b) 20nm/80nm Cr/Au metal contacts deposited by e-beam evaporator (metal contact dimensions, B25: 50µm x 160 µm, A35: 50 µm x 260 µm).

These opened areas having graphene needed to be etched, in order to eliminate any short circuit in between devices. The sample was placed in the RIE chamber and exposed using O_2 plasma for 5 minutes and the results are showing in **Figure 6.5**., where we can see that the areas outside the resist are clean and the graphene was etched. The sample was then submerged in acetone to remove the photoresist and the end results for 2 devices and multiple devices are shown in **Figure 6.6** (a) and (b).

For some experiments, we partially oxidized the surface of the InN NWs after they were grown. We did that by putting the as-grown sample in the RIE (Reactive Ion Etching) system and expose it to O_2 plasma for 5-10 minutes.

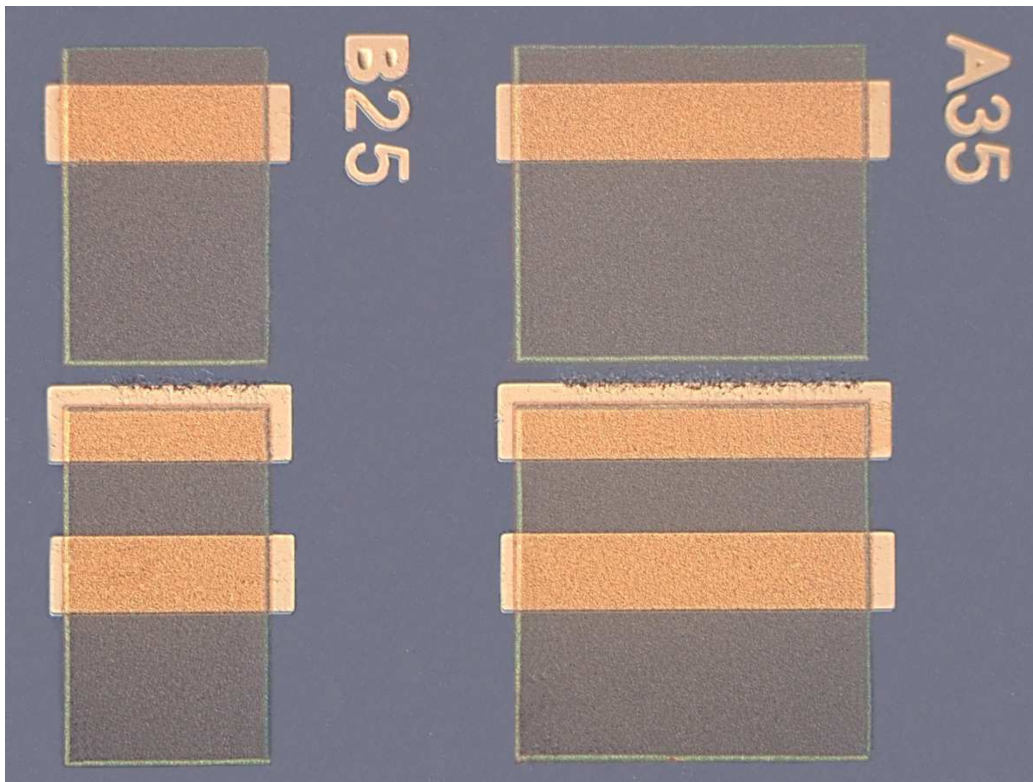

Figure 6.5 Optical image of patterned photoresist on graphene.

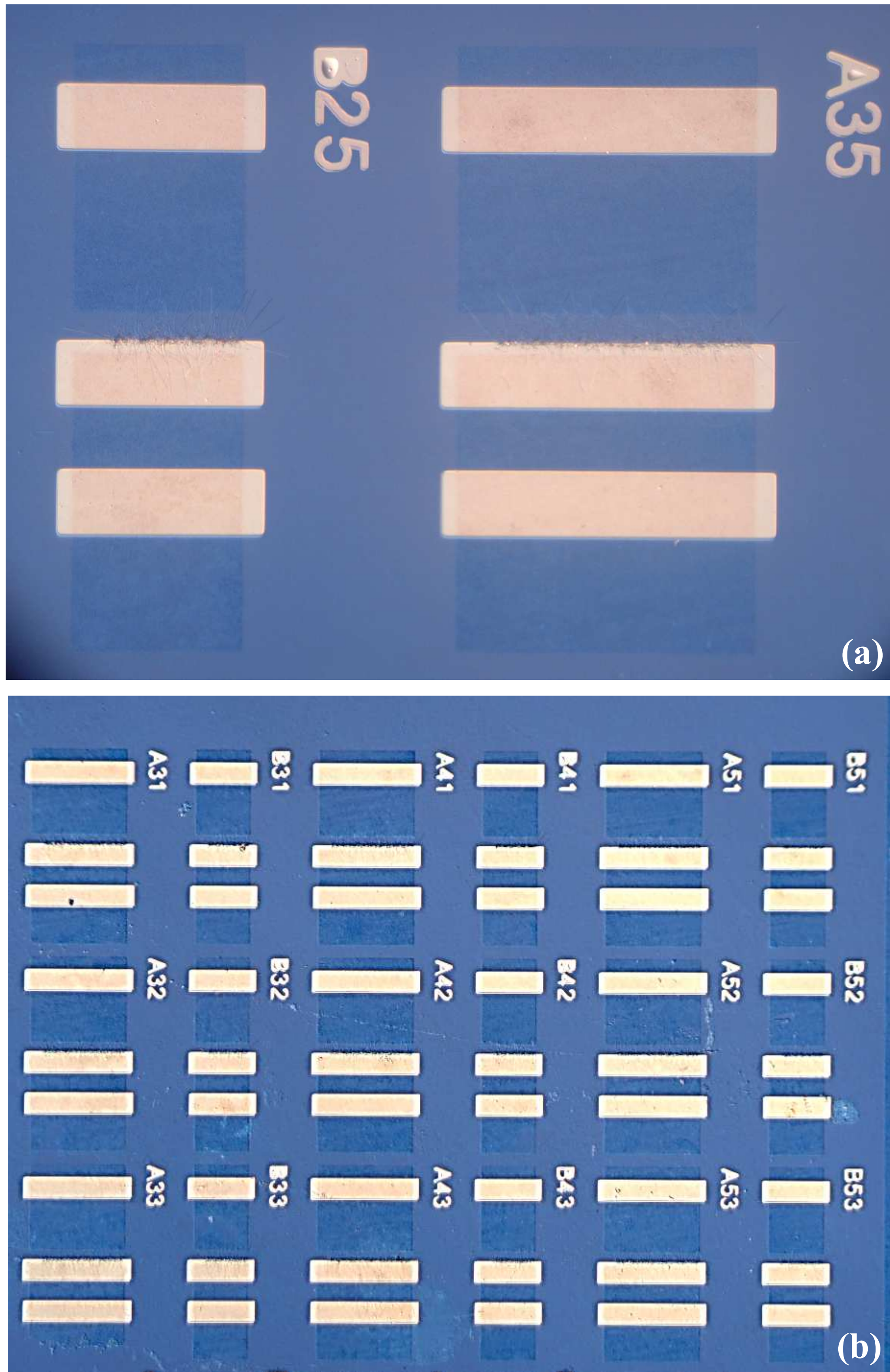

Figure 6.6 Optical images of (a) 2 devices and (b) multiple devices, after graphene transfer, graphene etch and resist removal.

6.3.2 Electrical characterization of graphene/InN NW heterojunction

We performed electrical characterization in both diode and barristor configurations and the results are shown below.

6.3.2.1 Electrical characterization of graphene/InN NW diode

The current-voltage measurements were performed using a Keithley 2612A System Source Meter unit. In **Figure 6.7** (a), we show the I-V characteristics of the pure InN NW/graphene heterojunction. Compared to **Figure 6.2**, this one is much less noisy and exhibits a larger Schottky barrier on both sides (-1.8 V on the negative side and 1.3 V on the positive side). This is due to the better and more controlled overlapping of graphene with NWs. Another important aspect is that, many devices on multiple samples showed results very close to this one, this consistency and repeatability would not be possible without using a precise fabrication process. When devices were fabricated, one extra metal contact was deposited on the graphene side of the device, in order to perform electrical characterization of graphene only and compare the results with those of the heterojunction. In **Figure 6.7** (b), we show the current-voltage measurements for a graphene field effect transistor, where Ohmic behavior is observed. This is obviously different from the results shown in **Figure 6.7** (a), which proves that the Schottky behavior is due to the heterojunction between graphene and InN NWs. The inset of both **Figure 6.7** show a schematic diagram of the measurement setup.

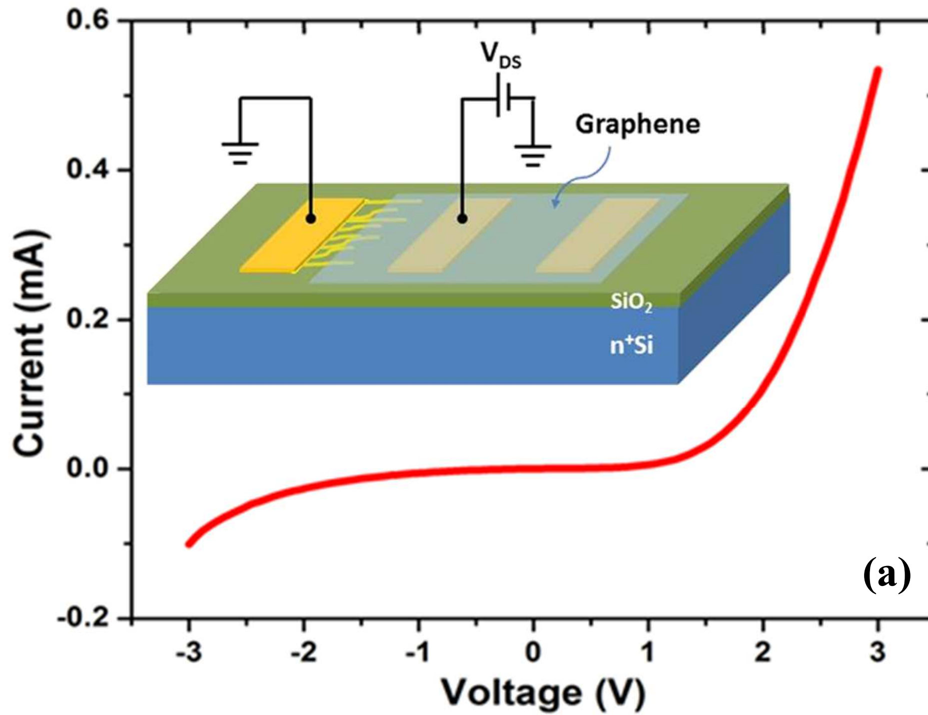

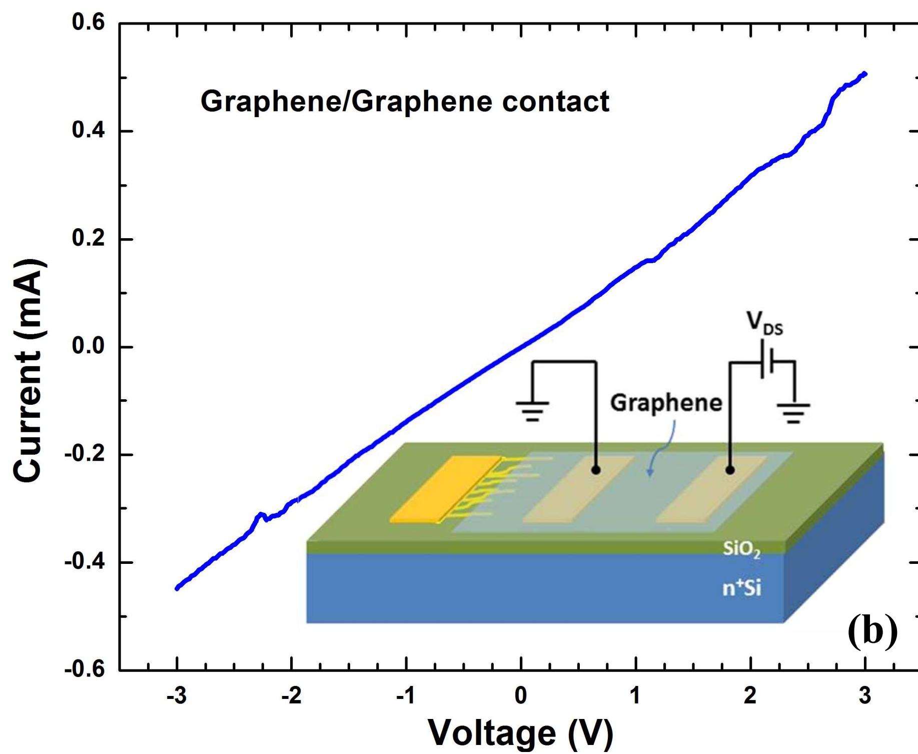

Figure 6.7 I-V characteristics for (a) InN NW/graphene heterostructure with inset showing the schematic diagram of the device and (b) graphene field effect transistor with inset showing the schematic diagram of the measurement.

6.3.2.2 Electrical characterization of graphene/InN NW barristor

The term *barristor* was first introduced in 2012, when a research group from Samsung Advanced Institute of Technology (SAIT), Korea, proposed a novel three-terminal device that could overcome the problems of integrating graphene into circuits. It is known that solid-state transistors and integrated circuits based on silicon have been more practical for complicated logic circuits. Even though silicon transistors have improved their speed and integration density, they exceeded the limit of channel lengths, causing leakage currents. To overcome these challenges, SAIT developed a three-terminal device based on graphene/Si heterojunction that could switch off the current in graphene without degrading its mobility. The on/off ratio current modulation of 10^5 (exceeding the minimum requirement for logic transistors) was achieved by adjusting the gate voltage to control the graphene/Si heterojunction Schottky barrier [116]. Similar to SAIT, Ojeda-Aristizabal *et al.* fabricated a vertical thin-film barristor device consisting of graphene/pentacene junction where the current across the device was modulated by the Fermi energy level of graphene by applying a gate voltage. The modulation energy barrier between graphene and pentacene was demonstrated to be as large as 300 meV [117].

For the first time, we demonstrated a three-terminal active device, a graphene variable barrier, barristor, in which the key is an atomically interface between graphene and InN NWs. Since the device has a back-gate, it is possible to modulate the current through the heterojunction using the gate voltage as shown in **Figure 6.8**. In (a), we see the I_D-V_{DS} with V_{GS} being swept from -20 V to 20 V. A positive gate bias depletes the graphene while causing accumulation in the InN NWs. However, it also decreases the

barrier height, therefore the current increases. With negative gate voltage, NWs get depleted while graphene accumulates carriers, but the widening of the barrier causes the current to drop, as shown in **Figure 6.8** (a) (the inset shows the schematic diagram of the measurement setup). In (b) we show the current magnitude in log scale for the same data in (a) where the on/off ratio is seen to exceed two orders, which makes these devices very promising for sensing applications with low power consumption. In **Figure 6.9** (a), we see the I_D-V_{GS} with V_{DS} being swept from -2 V to 2 V. A large drain voltage makes it harder for the channel to shut down completely, increasing the threshold voltage significantly. We have observed threshold voltages as high as -25 V and -19 V for drain voltages of -2 V and 2V, respectively. For smaller drain voltages, we have recorded threshold voltages close to -10 V. Since it is more favorable for sensing to operate the device near threshold voltage, we did all our experiments at low gate and drain voltages where near-threshold behavior could be achieved with reduced power consumption and lower bias stressing. In **Figure 6.9** (b) we show the magnitude of the current in log scale for the same data recorded in (a), where it is observed that the maximum current changes from 1 μA to approximately 10 nA.

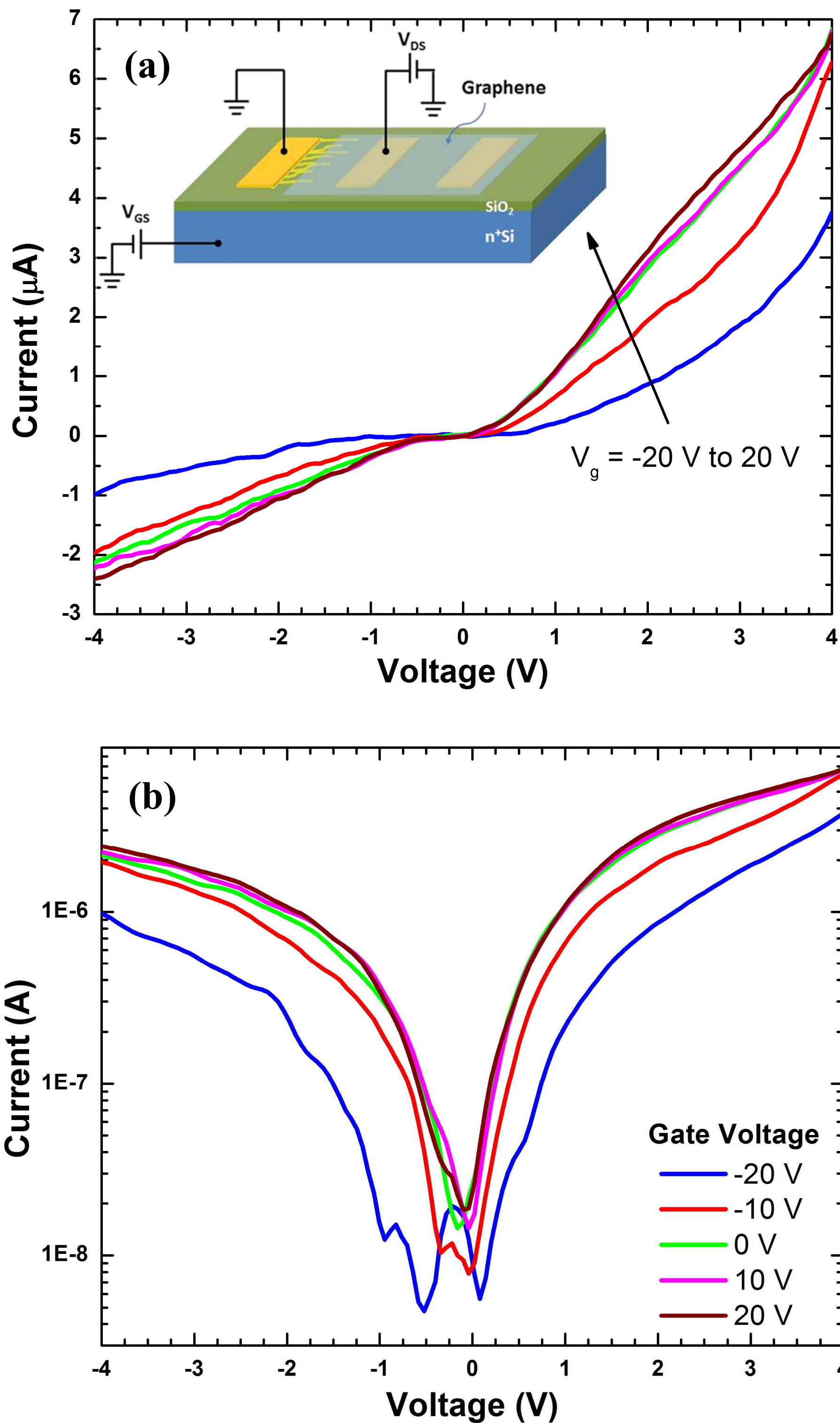

Figure 6.8 (a) I_d-V_d curves for graphene/InN NW heterostructure at gate bias voltages varying from -20 V to 20 V(the inset shows the schematic diagram of the measurement setup), (b) shows the magnitude of current in log scale for the data shown in (a).

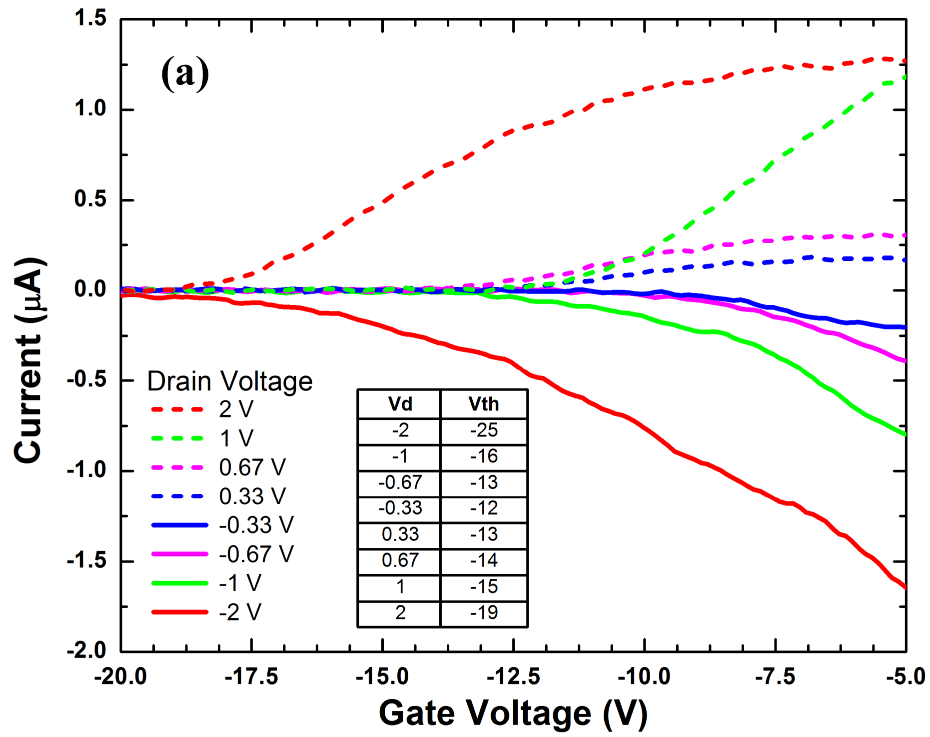

Vd	Vth
-2	-25
-1	-16
-0.67	-13
-0.33	-12
0.33	-13
0.67	-14
1	-15
2	-19

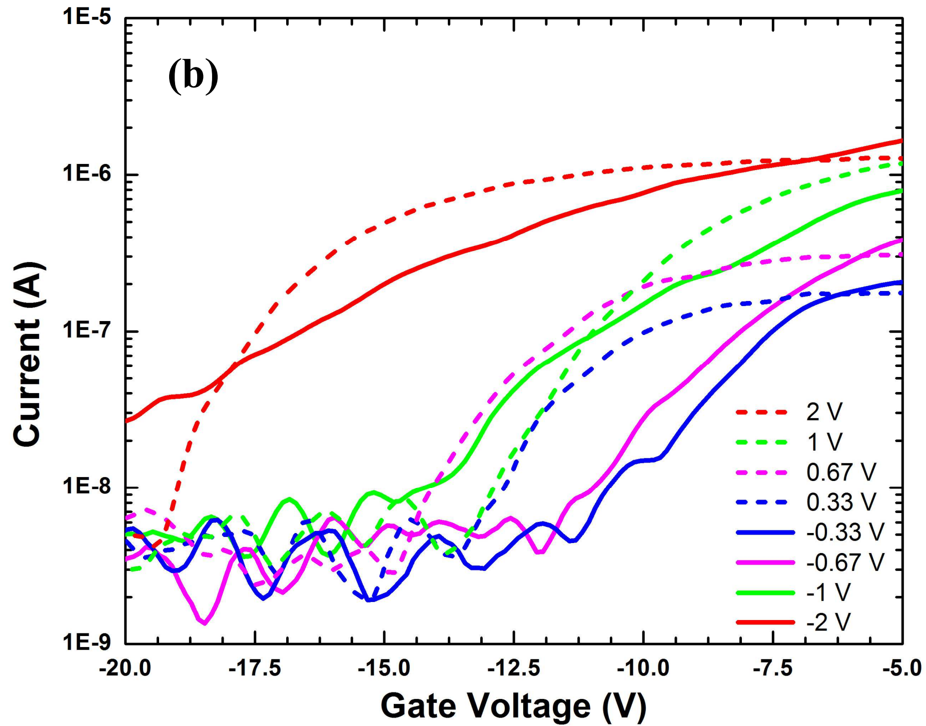

Figure 6.9 (a) I_d-V_g curve measured at drain voltages varying from -2 V to 2V, (b) shows the magnitude of current in log scale for the data shown in (a).

6.4 Effect of partial oxidation of InN NWs: bias stressing

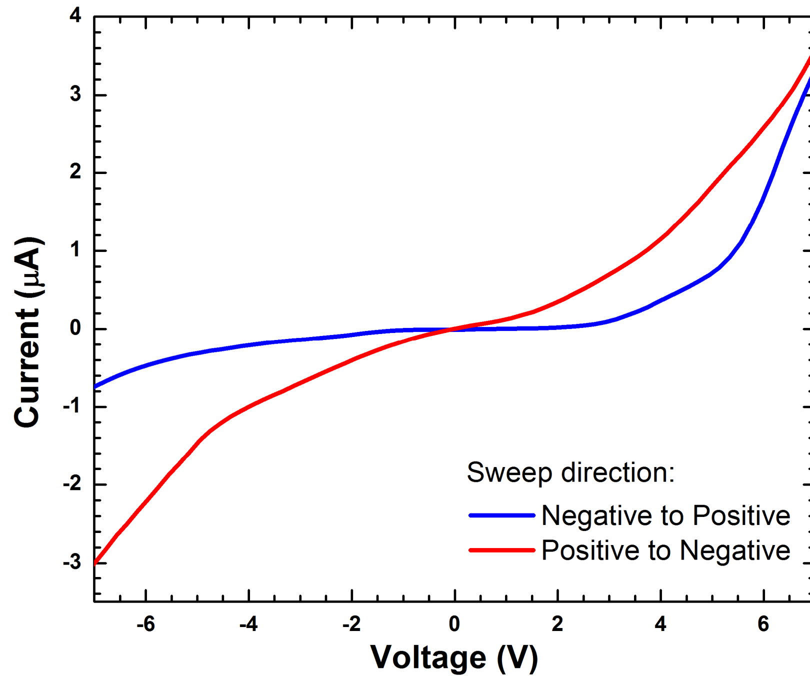

Figure 6.10 I-V characteristics of partially oxidized InN NW/graphene heterojunction, having the voltage swept from positive to negative and negative to positive direction.

In order to investigate the effect of high surface carrier concentration of InN NWs on the NW/graphene heterojunction, we tried passivation of the NW surfaces by partial oxidation of NWs before transferring graphene on them, as mentioned in the previous section. This resulted in some interesting phenomena – hysteresis was observed when the heterojunction was biased. In **Figure 6.10**, we see a heterojunction biased by a linear voltage sweep with direction being alternated from negative to positive and positive to negative. The I-V characteristics for both directions did not super-impose on each other, indicating the presence of hysteresis in the device. This happened due to the trapping of charges in the thin oxide layer on the surface of the NWs.

The trapped charges also play an important role when the heterojunction is

stressed by a sequence of dc bias voltages for particular time duration. In **Figure 6.11**, we see two different bias sequences; both show charging and discharging cycles with very large time constant, more than 100 seconds. In (a) and (b), the first thing to notice is the difference in current levels when the device is subjected to dc voltages of 8 V and -8 V. This is expected due to the strong rectifying behavior of the heterojunction. In (b), the y axis is enlarged to show the current levels for -0.3 V and 0 V more clearly. Here we see a gradual decay of current magnitude for constant bias levels of -0.3 V and 0 V, although it is more pronounced between the 8 V and – 8 V bias stages. Since the 8 V bias stage had a large current level, it caused a significant accumulation of trapped charges in the oxide, which were later discharged during the subsequent lower bias levels. The -8 V bias stage released the trapped charges, that is why no charging/discharging happened in the subsequent lower bias stages. The same thing happens in (c) and (d), where we apply 0.3 V and -1 V in the lower bias stages. Just like in (a) and (b), the current levels for the negative bias stages (-8 V and -1 V) are smaller than the ones for the positive bias stages (8 V and 0.3 V). We also see the discharging phases after the 8 V bias stage, until the -8 V bias stage reset the charge accumulation in the oxide, resulting in flat responses for the low bias stages afterwards.

Since the oxide traps only one kind of charges, it should just show the charging/discharging cycles for a particular polarity; therefore, the results that we observed here are not unusual. Since different chemical species may interact with these trapped charges differently, this observation may be utilized to enhance selectivity in sensing while the exponential response of the device could possibly result in high sensitivity at the same time.

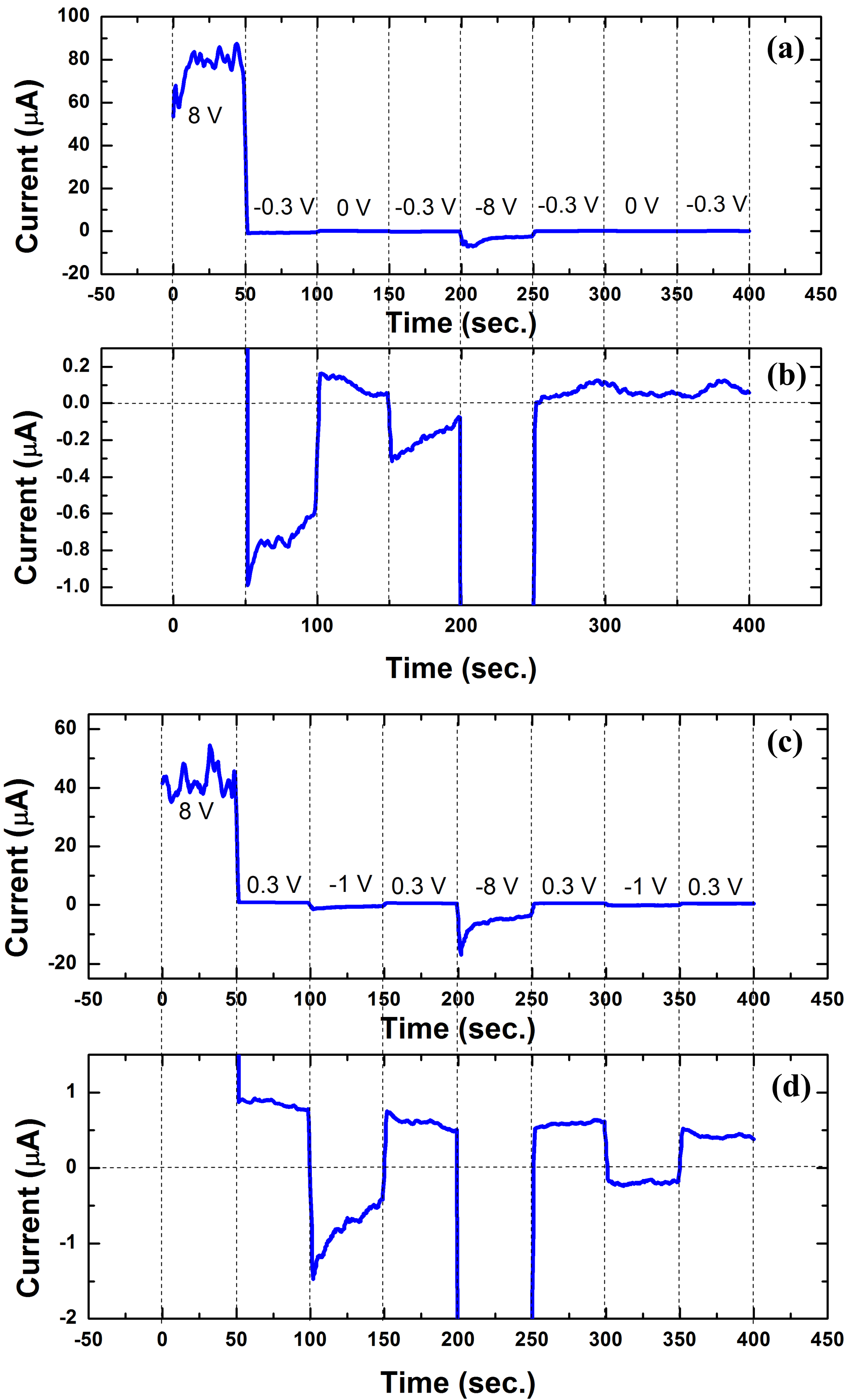

Figure 6.11 Effect of bias stressing and oxide charge trapping on the transient behavior of the partially oxidized InN NW/graphene heterojunction.

CHAPTER 7

CONCLUSION AND PROPOSED FUTURE WORK

7.1 Summary

The synthesis of high quality InN is challenging due to its low thermal decomposition temperature and the high equilibrium vapor pressure of nitrogen. In this work we have demonstrated a novel method for synthesizing single crystal InN NWs at temperatures much above their decomposition temperature by introducing controlled oxygen flow in the reaction chamber. It is proposed that oxygen adsorbs on the Au catalyst surface and accelerates the dissociation of NH_3, thereby enhancing the atomic N concentration and preventing decomposition of InN at the high growth temperature. Structural and compositional analyses of the NWs indicated that they are composed of only InN, with no presence of In_2O_3 detected for any of the oxygen flow rates used in this study. The quality of the NWs was found to improve with increasing oxygen flow rate, although, beyond a certain flow rate the changes became insignificant.

Electrical response of InN NWs in presence of certain chemical exposure has also been investigated. The InN NWs were used to fabricate multi NW (nano-network) based FET devices, which proved to have good gate control and great current modulation with a threshold voltage of -15 V for a drain voltage of 1 V.

Fabrication procedures for InN NEMS utilizing 3 different approaches have been investigated. First approach was to grow NWs and pattern trenches, etching them using

BOE (6:1). This technique resulted in having NWs sinking to the bottom of the trench due to surface tension and BOE sipping under the NWS etching the oxide underneath it. Second approach was similar to the first one, but etching the trenches was done by using carbon tetra fluoride based dry etch chemistry for SiO_2, which resulted in very nice and clean, isotropic etch. However, in this case the NW acted as a mask layer for SiO_2, so the oxide underneath the NW did not get etched. Last approach was done by patterning the trenches first and then grow NWs. NWs grew over the trenches spontaneously, getting suspended over the trenches. But putting contact pads on suspended NWs were a challenge due to large number of NWs growing and also number of patterns on one sample.

In this work, we also demonstrated a graphene/InN thin film heterojunction device that exhibits excellent sensitivity to a number of gases and analyte vapors. The heterojunction device offers better sensitivity to particular gases than plain InN or graphene based sensors because of the presence of Schottky barrier, which can be modulated by gas molecules. So far, high sensitivity to dilute NO_2 (30 ppb), NH_3 (100 ppb) and acetone vapor has been observed. These results are very encouraging, indicating the versatile and highly sensitive detection capabilities of our graphene/InN heterojunction sensors.

To explore promising alternative device approaches to address the challenges due to continuous shrinking of Si based devices in integrated circuits, we investigated for the first time graphene/InN NW heterojunction based vertical three-terminal active device. Two different methods of fabricating such devices have been investigated. First method, in which the heterojunction was constructed by transferring graphene on the NW sample,

where partial overlapping of graphene and NWs was done by hand, was proved to be very crude and unrepeatable. The second method was accomplished by using optical lithography to achieve a controlled overlapping. This variable transistor (or barristor) showed a very promising on/off ratio exceeding 100. This was achieved by adjusting the gate voltage to control the graphene/InN NW heterojunction Schottky barrier, which underlines the promise of these devices in low power device and sensing applications.

7.2 Proposed future work

7.2.1 Optimization process for NWs grown over trenches

Fabricating suspended NW devices is challenging due to the fact that NWs grow everywhere and it is hard to find the ones that are going over the trenches and deposit contact pads. To overcome the problem, we have proposed a technique where NWs will be synthesized on pre-growth trench, but in a controlled way where patterns will be made only on certain area of the sample. That way, contacts will be deposited by using Focused Ion Beam method (**Figure 7.1** and **Figure 7.2**). FIB trace deposition is usually done by electron beam induced deposition (EBID) mechanism. EBID is a process of decomposing gaseous molecules by electron beam leading to deposition of non-volatile fragments onto a nearby substrate. The electron beam is usually provided by a scanning electron microscope that results in high spatial accuracy (below one nanometer) and possibility to produce free-standing, three-dimensional structures.

Process steps involved:

- Pre-growth trench
- NW growth
- FIB trace deposition

- FIB contact pad deposition (mesh)
- FIB milling
- Wire bonding

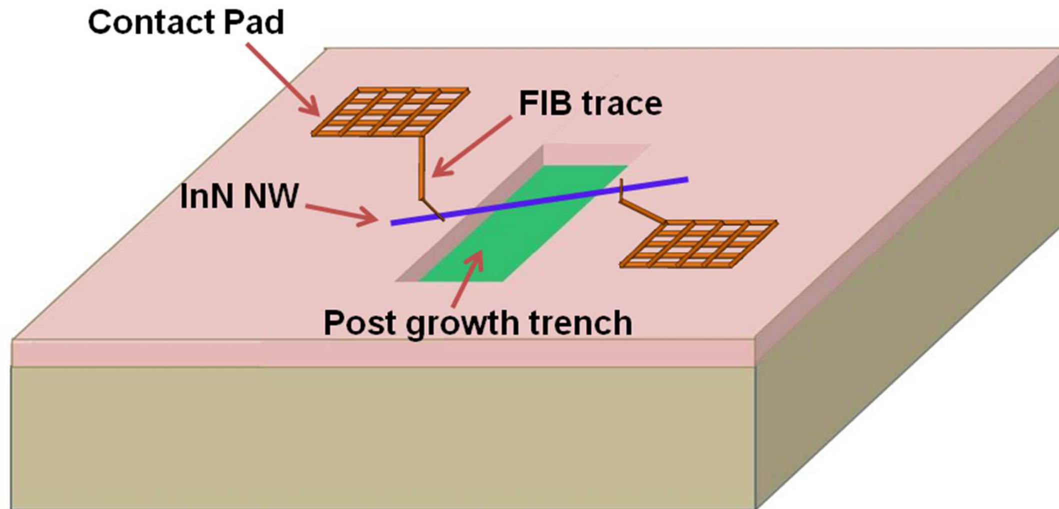

Figure 7.1 Schematic representation of NEMS resonator with contacts traced using FIB.

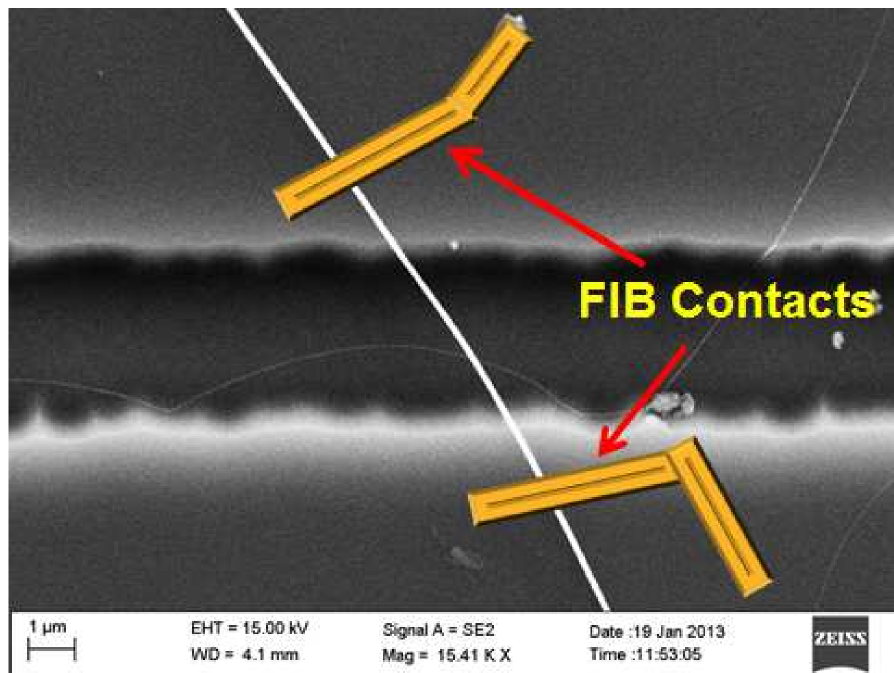

Figure 7.2 Proposed FIB method on NW grown on already etched trench.

7.2.2 Optimization of NW release process

In order to release the NWs it is proposed to use a combination of dry-HF vapor etch. NWs will be grown first and then pattern trenches that will be etched using CF_4 RIE method, followed by HF vapor etch (**Figure 7.3**). This will have the advantage of an anisotropic etch and release of NW due to HF vapors etching the SiO_2 from underneath the NW without having the surface tension caused by wet etching. This process proved to give results, but the vapor etch recipe needs to be optimized.

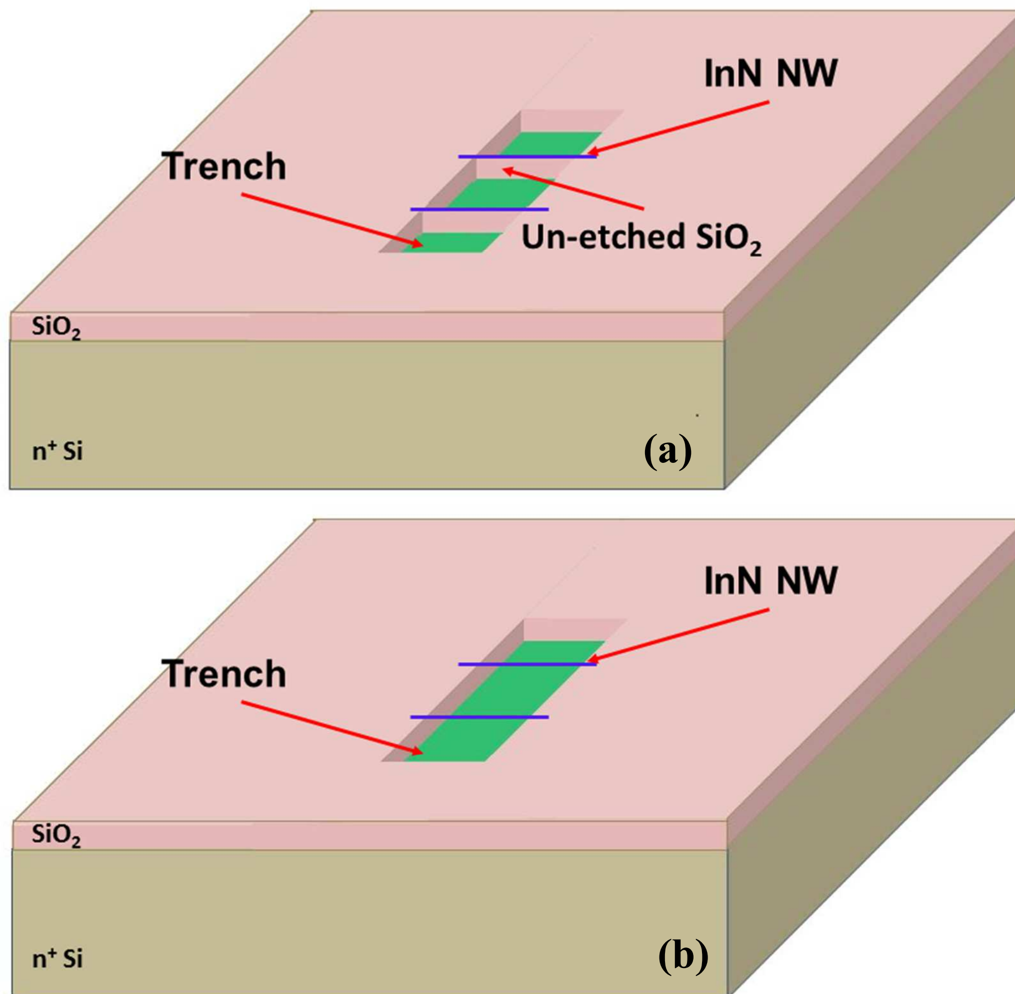

Figure 7.3 Optimization of InN NW release. (a) Shows a schematic diagram of trench etch using RIE and (b) shows a schematic diagram of NW release after etching the SiO_2 with HF vapor.

7.2.3 Graphene/InN NW heterojunctions

Graphene/InN NW heterojunctions will be further investigated and more devices will be fabricated.

7.2.2.1 Graphene/InN NW barristor

Graphene/InN NW barristor configuration (**Figure 7.4**) needs to be studied in more detail. It is a promising device due to preliminary results obtained and that has never been explored before. Three-terminal operation of graphene barristor offers numerous integrated device functionalities. The key operation of this triode takes place at the graphene/InN NW interface, where a Schottky barrier controls the charge transport vertically, by applying a back gate. The on/off ratio, exceeding 100 and obtained by adjusting the gate voltage to control the heterojunction Schottky barrier, underlines the promise of these devices of having low power consumption and be suitable for sensing applications.

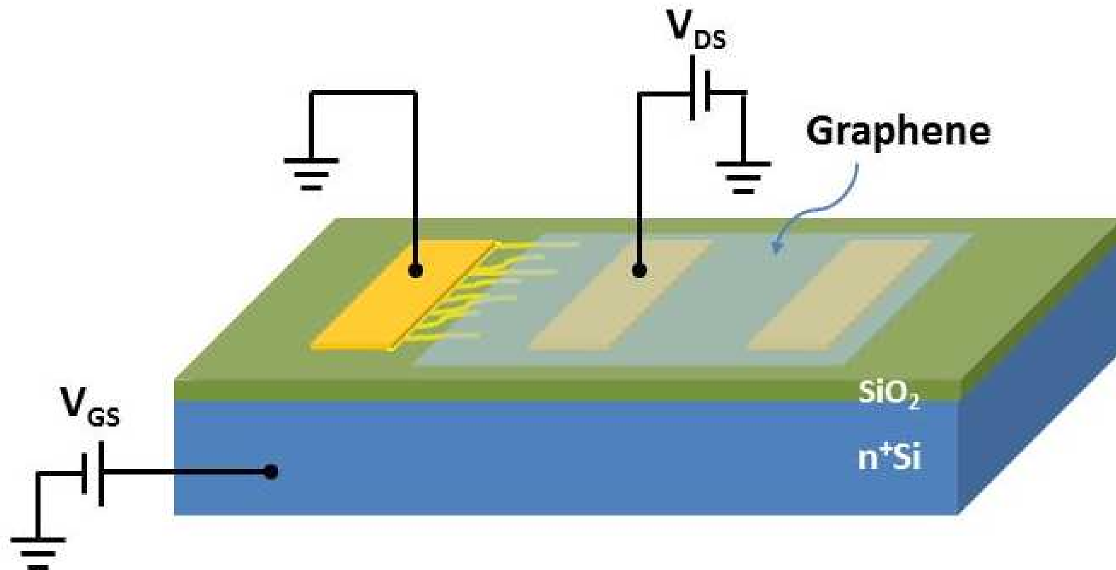

Figure 7.4 Graphene/ InN NW barristor configuration

7.2.2.2 Partial oxidation of InN NWs

Charge trapping effects need to be investigated further. The preliminary results showed a hysteresis behavior when the surface of the NWs was passivated by partial oxidation in the RIE chamber (**Figure 7.5**). This phenomenon happened when the heterojunction was biased and charges were trapped in the thin oxide layer on the surface of the NW. Different chemical species may interact with these trapped charges differently, so the further investigation of this passivation is important, as it could enhance the selectivity and as well the sensitivity of such devices.

Figure 7.5 Reactive ion etch system used for NW oxidation

7.2.2.3 Graphene/InN NW sensor

Better sensing results are expected compared to graphene/InN thin film heterojunction due to large surface to volume ratio at the junction between the two. Preliminary experiments were performed, but they need to be further investigated. The sensing setup is shown in **Figure 7.6** (a) where the device among with the probes acting

as source and drain can be seen on the screen. A close-up of the device is shown in (b) where three probes corresponding to source, drain and back-gate are observed. Due to the presence of a tunable Schottky barrier formed between graphene and InN NWs that can be modulated at different analyte gas molecules, and due to the large surface area to volume area at the junction mentioned earlier, these devices could offer better sensitivity than simple graphene or InN based sensors.

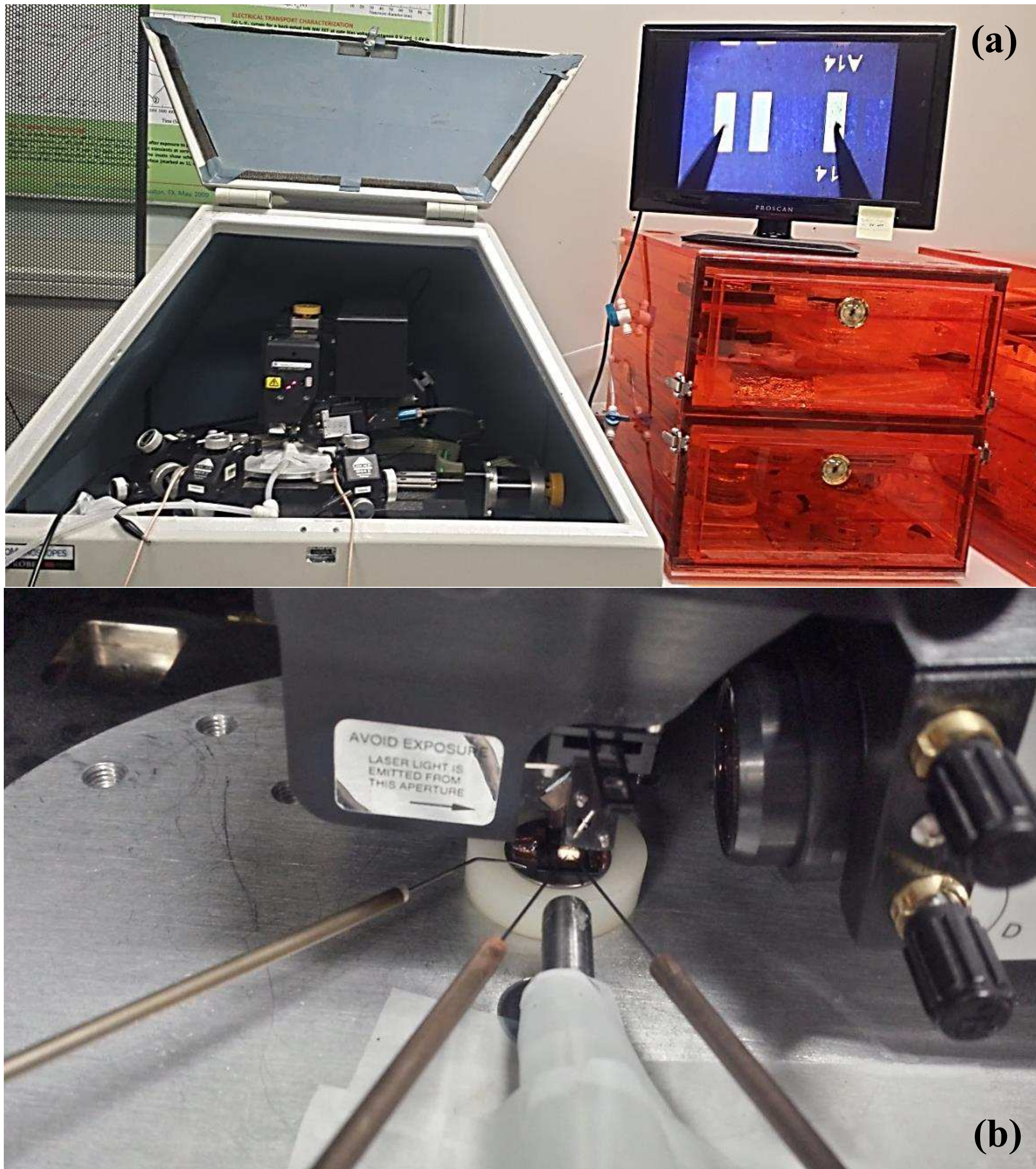

Figure 7.6 Graphene/InN NW heterojunction sensing setup (a) showing how the probes are placed on the sample and (b) showing a close-up of the device.

REFERENCES

[1] A. Hulanicki, S. Glab, and F. Ingman, "Chemical sensors definitions and classification," Pure & Appl. Chem., Vol. 63, pp. 1247-1250, 1991.

[2] M. M. Ayad and N. L. Torad, Talanta78 (4-5), 1280-1285 (2009).

[3] H. Sohn, M. J. Sailor, D. Magde and W. C. Trogler, *J. Am. Chem. Soc.*125 (13), 3821-3830 (2003).

[4] M. H. Yun, N. V. Myung, R. P. Vasquez, C. S. Lee, E. Menke and R. M. Penner, *Nano Lett.*4 (3), 419-422 (2004).

[5] Panev, N., et al., *Appl. Phys. Lett*. (2003) 83.

[6] K. L. Ekinci, and M. L. Roukes, *Rev. Sci. Instr*., 76, 061101 (2005).

[7] Y. T. Yang, C. Callegari, X. L. Feng, K. L. Ekinci, and M. L. Roukes, *Nano Lett.*, 6, 583 (2006).

[8] D. Rugar, R. Budakian, H. J. Mamin, and B. W. Chui, *Nature*, 430, 329 (2004).

[9] K. C. Schwab, and M. L. Roukes, *Phys. Today*, July, 36 (2005).

[10] X. L. Feng, C. J. White, A. Hajimiri, and M. L. Roukes, *Nat. Nanotech*. 3, 342 (2008).

[11] M. L. Roukes, In Technical Digest 2004 *IEEE International Electron Devices Meeting*, San Francisco, CA, December 13-15, p 539 (2004).

[12] X. L. Feng, R. He, P. Yang, and M. L. Roukes, *Nano Lett.*, 7, 1953 (2007).

[13] M. Law, J. Goldberger, P. Yang, *Annu. Rev. Mater. Res.* 34 (2004) 83.

[14] Ambacher O et al 1999 *J. Appl. Phys*. 85 3222–33.

[15] Polyakov V M and Schwierz F 2006 *Appl. Phys. Lett*.88 032101.

[16] Hullavarad S S et al 2006 *J. Electron. Mater*. 35 777–94.

[17] Ehtesham B. Quddus, Alina Wilson, Jie Liu, Zhihua Cai, Deepak Veereddy, Xinyong Tao, Xiaodong Li, Richard A. Webb, and Goutam Koley, *Phys. Status Solidi A*, 1-6 (2012).

[18] Matsuoka T, Okamoto H, Nakao M, Harima H and Kurimoto E 2002 *Appl. Phys. Lett.* 81 1246–8.

[19] Wu J, Walukiewicz W, Yu K M, Ager J W III, Haller E E, Lu H, Schaff W J, Saito Y and Nanishi Y 2002 *Appl. Phys.Lett*. 80 3967–9.

[20] Ch. Blomers, J. G. Lu, L. Hunag, C. Witte, D. Grutzmacher, H. Luth, and Th. Schapers, *Nanoletters* 12 (2012) 2768-2772.

[21] S. Zhao, O. Salehzadeh, S. Alagha, K. L. Kavanagh, S. P. Watkins and Z. Mi, *Appl. Phys. Lett* 102 (2013) 073102.

[22] Goutam Koley, Zhihua Cai, Ehtesham Bin Quddus, Jie Liu, Muhammad Qazi and Richard A. Webb, *Nanotechnology* 22 (2011) 295701.

[23] Mahboob I, Veal T D, Piper L F J, McConville C F, Lu H, Schaff W J, Furthmuller J and Bechstedt F 2004 *Phys. Rev. B* 69 201307.

[24] Aravind K, Su Y W, Ho I L, Wu C S, Chang-Liao K S, Su W F,Chen K H, Chen L C and Chen C D, 2009 Appl. Phys. Lett.95 092110.

[25] Colakerol L et al 2006 *Phys. Rev. Lett*. 97 237601.

[26] M. C. Johnson, C.J. Lee, E.D. Bourret-Courchesne, S.L. Konsek, S. Aloni, W.Q. Han, A. Zettl, *Appl. Phys. Lett*. 85 (2004) 5670.

[27] J. Zhang, B. Xu, F. Jiang, Y. Yang, J. Li, *Phys. Lett. A* 337 (2005) 121.

[28] S. D. Dingman, N.P. Rath, P.D. Markowitz, P.C. Gibbons, W.E. Buhro, Angew. *Chem., Int. Ed. Engl*. 39 (2000) 1470.

[29] X. M. Cai, F. Yeb, S.Y. Jing, D.P. Zhang, P. Fan, E.Q. Xie, *Applied Surface Science* 255 (2008) 2153–2158.

[30] Cai Z, Garzon S, Chandrashekhar M V S, Webb R A and Koley G 2008 *J. Electron. Mater*. 37 585–92.

[31] Ananta R. Acharya, Sampath Gamage, M.K. Indika Senevirathna, Mustafa Alevli, Kucukgok Bahadir, Andrew G. Melton, Ian Ferguson, Nikolaus Dietz, Brian D. Thoms, *Applied Surface Science* 268 (2013) 1– 5.

[32] S. Zhao, S. Fathololoumi, K. H. Bevan, D. P. Liu, M. G. Kibria, Q. Li, G. T. Wang, Hong Guo, and Z. Mi, *Nano Lett*. 2012, 12, 2877−2882.

[33] Tao Tang, Song Han, Wu Jin, Xiaolei Liu, Chao Li, Daihua Zhang, and Chongwu Zhoua, Bin Chen, Jie Han, M. Meyyapan, *J. Mater. Res*., Vol. 19, No. 2, Feb 2004.

[34] F. Patolsky, B. P. Timko, G. Zheng, and C. M. Lieber, MRS BULLETIN, 32, 142 (2007).

[35] G. Koley, Ph. D. dissertation, Connell University, p.10, (2003).

[36] O. Ambacher, J. Smart, J. R. Shealy, N. G. Weimann, K. Chu, M. Murphy, W. J. Schaff, L. F. Eastman, R. Dimitrov, L. Wittmer, M. Stutzmann, W. Rieger, and J. Hilsenbeck, *J. Appl. Phys*., 85, 3222 (1999).

[37] V. Cimalla, M. Niebelschütz, G. Ecke, V. Lebedev, O. Ambacher, M. Himmerlich, S. Krischok, J. A. Schaefer, H. Lu, and W. J. Schaff, *Phys. Stat. Sol.* (a) 203(1), 59–65 (2006).

[38] Hamaguchi C, 2001 Basic Semiconductor Physics (Berlin:Springer) pp 375–77.

[39] I. Mahboob, T. D. Veal, C. F. McConville, H. Lu and W. J. Schaff, *Phys. Rev. Lett.*92.036804, 2004.

[40] Ananta R. Acharya, Sampath Gamage, M.K. Indika Senevirathna, Mustafa Alevli, Kucukgok Bahadir, Andrew G. Melton, Ian Ferguson, Nikolaus Dietz, Brian D. Thoms, *Applied Surface Science* 268 (2013) 1– 5.

[41] R. Calarco, and M. Marso, *Appl. Phys. A*, 87, 499 (2007).

[42] P. D. C. King, T. D. Veal, C. F. McConville, F. Fuchs, J. Furthmüller, F. Bechstedt, P. Schley, R. Goldhahn, J. Schörmann, D. J. As, K. Lischka, D. Muto, H. Naoi, Y. Nanishi, Hai Lu, and W. J. Schaff, *Appl. Phys. Lett*., 91, 092101 (2007).

[43] S. Zhao, S. Fathololoumi, K. H. Bevan, D. P. Liu, M. G. Kibria, Q. Li, G. T. Wang, Hong Guo, and Z. Mi, *Nano Lett.* 2012, 12, 2877−2882.

[44] Petersen G, Hernandez S E, Calarco R, Demarina N andSchaepers T, 2009 Phys. Rev. B 80,125321.

[45] Ming-Shien Hu, Wei-Ming Wang, Tzung T. Chen, Lu-Sheng Hong, Chun-Wei Chen, Chia-Chun Chen, Yang-Fang Chen, Kuei-Hsien Chen, and Li-Chyong Chen. *Adv. Funct. Mater*. 2006, 16, 537-541.

[46] C. H. Liang, L.C. Chen, J. S. Hwang. K. H. Chen, Y. T. Hung, Y. F. Chen. *Appl. Phys. Lett*, 81 (2002).

[47] J. I. Pankove and T. D. Moustakas, Gallium Nitride I, *Semiconductors and Semimetals*, Vol. 50, Academic Press, 1998.

[48] Jeganathan, V. Purushothaman, R. K. Debnath, R. Calarco, and H. Luth, *Appl. Phys. Lett*., 97, 093104 (2010).

[49] F. Agulló-Rueda, E.E. Mendez, B. Bojarczuk, S. Guha, *Solid State Comm*., 115, 19-21, 2000.

[50] Satyaprakash Sahoo, M. S. Hu, C. W. Hsu, C. T. Wu, K. H. Chen, L. C. Chen, A. K. Arora, and S. Dhara. *Appl. Phys. Lett*. 93, (2008) 233116.

[51] J. S. Thakur, D. Haddad, V. M. Naik, R. Naik, G. W. Auner, H. Lu, and W. J. Schaff, *Phys. Rev. B*, 71, 115203 (2005).

[52] Staffan Westerberg, Chen Wang, Keng Chou, and Gabor A. Somorjai, *J. Phys. Chem.* B 2004, 108, 6374-6380.

[53] J. Fogelberg, I. Lundström and L-G Petersson, *Phys. Scr.,* 1987, 35, 702.

[54] D. P. Sobczyk, A.M. de Jong, E. J. M. Hensen, and R.A. van Santen, *Journal of Catalysis* 219 (2003) 156–166.

[55] Nuria Lopez, Monica Garcia-Mota, and Jaime Gomez-Diaz, *J. Phys. Chem. C* 2008, 112, 247-252.

[56] A. Franceschetti, S. J. Pennycook, S.T. Pantelides, *Chemical Physics Letters* 374 (2003) 471–475.

[57] Huaqiang Wu, Ho-Young Cha, M. Chandrashekhar, Michael G. Spencer, and Goutam Koley, *J. Electron. Mater*, Vol. 35, No. 4, (2006).

[58] A. Zubrilov, "Properties of Advanced SemiconductorMaterials GaN, AlN, InN, BN, SiC, SiGe.," (eds. M. E. Levinshtein, S. L. Rumyantsev, M. S. Shur), John Wiley & Sons, Inc., New York, pp. 49-66 (2001).

[59] C. H. Swartza, R. P. Tompkinsa, N. C. Gilesa, T. H. Myersa, H. Lub, W. J. Schaffb and L. F. Eastman, *Journal of Crystal Growth*, 269**,** 29 (2004).

[60] W. Qian, M. Skowronski, and G. R. Rohrer, Structural defects and their relationship to nucleation of GaN thin films. in III-Nitride, SiC, and Diamond Materials for Electronic Devices. Eds. D. K. Gaskill, C. D. Brandt and R. J. Nemanich, *Material Research Society Symposium Proceedings*, Pittsburgh, PA. 423, 475-486 (1996).

[61] A. F. M. Anwar, S. Wu, and R. T. Webster, *IEEE Trans. Electron Devices*, 48(3), 567 (2001).

[62] E B. Quddus, J. Liu, Z. Cai, D.Veereddy, X. Tao, X. Li, R. A. Webb, G. Koley, "Structural and mechanical properties of InN nanowires," *Physica Status Solidi*, Vol. 209, pp. 718-723, April 2012.

[63] R. B. Sadeghian and M. Kahrizi. "A novel gas sensor based on tunneling-field_ionization on whisker-covered gold nanowires," *IEEE Sensors Journal*, Vol. 8, No.2, pp. 161-169, 2008.

[64] A. Modi, N. Koratkar, E. Lass, B. Wei, P. M. Ajayan, "Miniaturized gas ionization sensors using carbon nanotubes," *Nature*, vol. 424, pp.171–174, 2003.

[65] S. Strite and H. Morkoc, *J. Vac. Sci. Technol*. B10, 1237 (1992).

[66] Wilke, I.; Ascazubi, R.; Lu, H.; and Schaff W. J.; *Appl. Phys. Lett.*2009, 93, 221113.

[67] Jones, R. E.; Li, S. X.; Haller, E. E.; van Genuchten, H. C. M.;Yu, K. M.; Ager III, J. W.; Liliental-Weber, Z.; and Walukiewicz, W.; Lu, H.; and Schaff W. J.; *Appl. Phys. Lett.*2007, 90, 162103.

[68] A. Hussain, J. Hone, Henk W. Ch. Postma, X. M. H. Huang, T. Drake, M. Barbic, A. Scherer and M. L. Roukes; "Nanowire-based very-high-frequency electromechanical resonator," *Appl. Phys. Lett*. 2003, 83, 1240.

[69] Ford A C, Ho J C, Chueh Y, Tseng Y, Fan Z, Guo J, Bokor Jand Javey A, 2009 *Nano Lett.* 9 360–5.

[70] K. L. Ekinci, and M. L. Roukes, *Rev. Sci. Instr.*, 76, 061101 (2005).

[71] Y. T. Yang, C. Callegari, X. L. Feng, K. L. Ekinci, and M. L. Roukes, *Nano Lett.*, 6, 583 (2006).

[72] D. Rugar, R. Budakian, H. J. Mamin, and B. W. Chui, Nature, 430, 329 (2004).

[73] K. C. Schwab, and M. L. Roukes, *Phys. Today*, 36, July 2005.

[74] X. L. Feng, C. J. White, A. Hajimiri, and M. L. Roukes, *Nature Nanotech.*3, 342 (2008).

[75] M. L. Roukes, In Technical Digest 2004 *IEEE International Electron Devices Meeting*, San Francisco, CA, December 13-15, p 539 (2004).

[76] M. A. Khaderbad. Y. Choi, P. Hiralal, A. Aziz, N. Wang, C. Durkan, P. Thiruvenkatanathan, G. A. J. Amaratunga, V. Ramgopal Rao, A. A. Seshia, *Nanotechnology*, 23, 2012.

[77] Li M, Bhiladvala R B, Morrow T J, Sioss J A, Lew K-K, Redwing J M, C. D. Keating, T. S. Mayer, *Nat. Nanotechnology*, 2008, 88-92.

[78] S. Wolf, R. N. Tauber,"Silicon processing for the VLSI Era," *Process Technology*, Vol. 1, pp. 532-533, 1986.

[79] C. Iliescu, J. Jing, F. Tay, J. Miao, T. Sun, *Surf. Coat. Tech*., 2005, 198.

[80] http://www.cleanroom.byu.edu/rie_etching.phtml.

[81] G. S. Oehrlein, "Reactive-ion etching," *Physics Today*, 39(10), 26 (1986).

[82] C. Wu, C. Shen, H. Lin, H. Lee, S. Gwo, "Direct evidence of 8: 9 commensurate heterojunction formed between InN and AlN on c plane", *Appl. Phys. Lett*. 2005, 87, 241916:1–241916:3.

[83] Y.-S. Lu, C.-C. Huang, J. A. Yeh, C.-F.; Chen, S. Gwo, "InN-based anion selective sensors in aqueous solutions", *Appl. Phys. Lett*. 2007, 91, 202109:1–202109:3.

[84] Y.-H. Chang, Y.-S. Lu, Y.-L. Hong, C.-T. Kuo, S. Gwo, J. A. Yeh, "Effects of $(NH_4)_2S_x$ treatment on indium nitride surfaces", *J. Appl. Phys.* 2010, 107, 043710.

[85] Y.-S. Lu, C.-L. Ho, J. A. Yeh, H.-W. Lin, S. Gwo, "Anion detection using ultrathin InN ion selective field effect transistors", *Appl. Phys. Lett.* 2008, 92, 212102:1–212102:3.

[86] L. Voss, B. P. Gila, S. J.; Pearton, H. T.; Wang, F. Ren, "Characterization of bulk GaN rectifiers for hydrogen gas sensing", *J. Vac. Sci. Technol. B* 2005, 23, 2373–2377.

[87] F. L. Hsiao, C. Lee, "Computational study of photonic crystals nano-ring resonator for biochemical sensing", *IEEE Sens. J.* 2010, 10, 1185–1191.

[88] Y.-H. Chang, K.-K. Chang, S. Gwo, J. A. Yeh, "Highly sensitive hydrogen detection using a Pt-catalyzed InN epilayer", *Appl. Phys. Express* 2010, 3, 114101–114103.

[89] O. Kryliouk, H. J. Park, H. T. Wang, B. S. Kang, T. J. Anderson, F. Ren, S. J. Pearton, "Pt-coated InN nanorods for selective detection of hydrogen at room temperature", *J. Vac. Sci. Technol. B* 2005, 23, 1891–1894.

[90] H. Lu, W. J. Schaff amd L. F. Eastman, "Surface chemical modification of InN for sensor applications," *J. Appl. Phy.,* 2004, 96 (6), 3577-3579.

[91] Y.-H. Chang, K.-K. Chang, S. Gwo, J. A. Yeh, "Highly sensitive pH sensing using an indium nitride ion-sensitive field-effect transistor", *IEEE Sens. J.* 2011, 11, 1157–1161.

[92] Y.-S. Lin, J. A. Yeh, "GaN-based light-emitting diodes grown on nanoscale patterned sapphire substrates with void-embedded cortex-like nanostructures", *Appl. Phys. Express*, 2011, 4, 092103.

[93] H. Lu, W. J. Schaff amd L. F. Eastman, "Surface chemical modification of InN for sensor applications," *J. Appl. Phy.,* 2004, 96 (6), 3577-3579.

[94] K.-W. Kao, M.-C. Hsu, Y.-H Chang, S. Gwo, J. A. Yeh, "A Sub-ppm Acetone Gas Sensor for Diabetes Detection Using 10 nm Thick Ultrathin InN FETs", *Sensors* 2012, *12*(6), 7157-7168.

[95] A. M. Basilio, Y.-K. Hsu, C. C. Chang, P. C. Wei, A. Ganguly, H. C. Shih, Y.-T. Chen, L.-C. Chen, K.-H. Chen, "Electrochemical Characterization of

InN Thin Films for Biosensing Applications”, *J. New Mater. Electrochem. Syst*. 2010, 13(4), 337-343.

[96] F. Schedin, A. K. Geim, S. V. Morozov, E. W. Hill, P. Blake, M. I. Katsnelson, and K. S. Novoselov, “Detection of individual gas molecules adsorbed on graphene”, *Nature Mater*. 2007, 6, 652 – 655.

[97] M. W. K. Nomani, R. Shishir, M. Qazi, D. Diwan, V. B. Shields, M. G. Spencer, G. S. Tompa, N. M. Sbrockey, and G. Koley, “Highly sensitive and selective detection of NO_2 using epitaxial graphene on 6H-SiC”, *Sens. Actuators B* 2010, 150, 301.

[98] R. A. Potyrailo, C. Surman, N. Nagraj, and A. Burns, “Materials and Transducers Toward Selective Wireless Gas Sensing”, *Chem. Rev.* 2011, 111, 7315.

[99] S. Rumyantsev, G. Liu, M. S. Shur, R A. Potyrailo, and A. A. Balandin, “Selective Gas Sensing with a Single Pristine Graphene Transistor”, *Nano Lett.* 2012, 12, 2294.

[100] A. K. Singh, M. A. Uddin, J. T. Tolson, H. Maire-Afeli, N. Sbrockey, G. S. Tompa, M. G. Spencer, T. Vogt, T. S. Sudarshan, G. Koley, “Electrically tunable molecular doping of graphene”, *Appl. Phys. Lett.* 2003, 102, 043101.

[101] A. H. Goldstein, I. E. Galbally, “Known and unexplored organic constituents in the earth’s atmosphere,” *Environmental Science and Tech.*, (2007), 41, 1514-21.

[102] U. Niinemets, F. Loreto, M. Reichstein, "Physiological and physicochemical controls on foliar organic compound emissions," *Trends in Plant Science*, (2004), 180-6.

[103] S. Wang, H. M. Ang, M. O. Tad, "Volatile organic compounds in indoor environment and photocatalytic oxidation: state of the art," *Environment International*, (2007), 694-705.

[104] W. H. Brattain and J. Bardeen, "Surface properties of germanium," *Bell Syst. Tech. J.,* 32 (1953) 1.

[105] G. Sberveglieri, "Recent developments in semiconducting thin-film gas sensors," *Sensors and Actuators B* 23, (1995) 103-109.

[106] Ehtesham B. Quddus, Alina Wilson, Richard A. Webb, and Goutam Koley, "Oxygen mediated synthesis of high quality InN nanowires above their decomposition temperature," *Nanoscale*, 2014, 6, 1166.

[107] K. Bolotin, K. Sikes, J. Hone, H. Stormer, and P. Kim, "temperature-dependent transport in suspended graphene," *Physical Rev. Lett.*, vol. 101, p. 096802, 2008.

[108] A. A. Balandin, S. Ghosh, W. Bao, I. Calizo, D. Teweldebrhan, F. Miao, *et al.*, "Superior thermal conductivity of single-layer graphene," *Nano letters*, vol. 8, pp. 902-907, 2008.

[109] C. Lee, X. Wei, J. W. Kyser, and J. Hone, "Measurement of the elastic properties and intrinsic strength of monolayer graphene," *Science*, Vol. 321, pp. 385-388, 2008.

[110] K. S. Novoselov, A. K. Geim, S. Morozov, D. Jiang, Y. Zhang, S. Dubonos, *et. al*., "Electric field effect in atomically thin carbon films," *Science*, vol. 306, pp. 666-669, 2004.

[111] Zhang, Q., Wang, P., Li, J., Gao, X. "Diagnosis of diabetes by image detection of breath using gas-sensitive laps," *Biosens. Bioelectron.* 2000, 15, 249–256.

[112] Moorhead, K., Lee, D., Chase, J., Moot, A., Ledingham, K., Scotter, J., Allardyce, R., Senthilmohan, S., Endre, Z., "Classifying algorithms for SIFT-MS technology and medical diagnosis." *Comput. Methods Progr. Biomed.* 2008, 89, 226–238.

[113] Kun-Wei Kao, Ming-Che Hsu, Yuh-Hwa Chang, Shanjr Gwo, and J. Andrew Yeh, "A sub-ppm acetone gas sensor for diabetes detection using 10 nm thick ultrathin InN FETs," *Sensors*, 7157-7168, 2012.

[114] O. Kryliouk, H. J. Park, H. T. Wang, B. S. Kang, T. J. Anderson, and F. Ren, "Pt-coated InN nanorods for selective detection of hydrogen at room temperature," *J. Vac. Sci. Technol*., B 23(5), 2005.

[115] F. Schedin, A. K. Geim, S. V. Morozov, E. W. Hill, P. Blake, M. I. Katsnelson, *et al*., "Detection of individual gas molecules adsorbed on graphene," *Nat Mater*, vol. 6, pp. 652-655, 2009.

[116] H. Yang, J. Heo, S. Park, H. J. Song, D. H. Seo, K.E. Byun, P. Kim, I. Yoo, H. J. Chung, K. Kim, "Graphene barristor, a triode device with a gate-controlled Schottky barrier," *Science*, vol. 336, 2012.

[117] C. Ojeda-Aristizabal, W. Bao, and M. S. Fuhrer, “Thin-film barristor: a gate-tunable vertical graphene-pentacene device,” *Phys. Rev. Lett.*, 88, 035435, 2013.

APPENDIX A

DEVICE FABRICATION

1. FET FABRICATION

Step	***Description***	***Process Details***
1.1	Sample Clean	Sonicate sample in acetone and IPA for 5 minutes each Dry sample using nitrogen
1.2	Optical Lithography	Photoresist: S1811 Spin: 4000 rpm for 30 sec Bake: 100 °C for 1 min Developer: DI water : MF-351 (5:1)
1.3	Metal Deposition	Equipment: E-beam (or thermal) evaporator Pressure: below $2x10^{-6}$ Torr Gold (Au): 2 nm
1.4	Electron Beam Lithography	Photoresist layer 1: PMMA 495K Spin: 6000 rpm at for 40 sec Soft Bake: 180˚C for 2 min on hotplate Photoresist layer 2: PMMA 950K Spin: 6000 rpm at for 40 sec) Soft Bake: 180˚C for 2 min on hotplate Total PR thickness: 0.270 μm Exposure: Specimen/Collector Current = 20 pA to 1500 pA, Dose: 3.7 to 3.81 pC/ μm^2 Developer: MIBK: IPA 1:3 Ratio Temperature: 23˚C Time: 40 Sec Rinse: IPA 30 sec, N_2 blow dry
1.5	Metal Deposition	Equipment: E-beam metal evaporator Deposition of following metal stack at pressure below 2×10^{-6} Torr Titanium (Ti): 20 nm Aluminum (Al): 50 nm Titanium (Ti): 20 nm Gold (Au): 50 nm

2. SUSPENDED NWS FABRICATION

Step	*Description*	*Process Details*
1.1	SiO_2 Dry Etch using RIE	Equipment: MARCH CS-1791 SiO_2 etch for 3 min Gases: CHF_3 = 4 sccm, O_2 = 20 sccm Power: 200 W; Pressure: 200 mTorr Etch rate is ~ 40 nm/min
1.2	SiO_2 Wet Etch 6:1 BOE	Removal of SiO_2 with Buffered Oxide Etch (BOE 6:1) The etch rate is ~2 nm/sec

3. GRAPHENE/INN NW HETEROSTRUCTURE FABRICATION

Step	*Description*	*Process Details*
1.1	Optical Lithography	Mask Aligner: Karl Suss MJB3 Promoter: HMDS Spin: 5000 rpm for 10 sec Photoresist: AZ1518 Spin: 5000 rpm for 30 sec Bake: 110 °C for 90 sec Developer: DI water : AZ400K (4:1)
1.2	Metal Deposition	Equipment: E-beam metal evaporator Deposition of following metal stack at pressure below 2×10^{-6} Torr Chromium (Cr): 20 nm Gold (Au): 50 nm
1.3	Graphene etch using RIE (O_2 plasma)	Equipment: MARCH CS-1791 Graphene etch for 150 sec Pressure: 300 mT Power: 150 W Total gas flow: 50 sccm